Observation of Initial and Final-State Effects in the Systems (^{6}He+n), (^{8}He+n), and (^{9}Li+n)

By

Luke Chen

A DISSERTATION

Submitted to
Michigan State University
in partial fulfillment of the requirements
for the Degree of

DOCTOR OF PHILOSOPHY

Department of Physics and Astronomy

2000

ABSTRACT

Observation of Initial and Final-State Effects in the Systems (^{6}He+n), (^{8}He+n), and (^{9}Li+n)

By

Luke Chen

An experiment was performed at the NSCL to study the unbound nuclei ^{10}Li and ^{7,9}He produced in breakup of 30 MeV/u ^{12,11,10}Be nuclei on a ^{9}Be target. The observed relative velocity distribution of the neutron relative to the fragment shows that the initial states have significant influence on the observed final-state interactions. A value of 440±16 keV has been obtained for the $p_{3/2}$ resonance energy in ^{7}He. The experiment confirms the existence of a low-lying l=0 state for the ^{10}Li isotope, corresponding to a scattering length a_s <-10 fm. The (^{8}He+n) data are limited by counting statistics but seem to offer the first evidence for an l=0, l=1 inversion, in this case characterized by a numerically large scattering length $a_s \leq -10$ fm.

For my family and friends

ACKNOWLEDGMENTS

First and foremost, I would like to thank Gregers Hansen for being a terrific role-model as well as my thesis advisor. It was a joy working for someone who is knowlegeable, patient, insightful, and humorous. I sincerely appreciated all the support and encouragement I've received during these years working on this research project. I will miss working with him. I want to thank Michael Thoennessen for providing me with a chance to work with him and all the help with data analysis. In addition, I would like to thank Walt Benenson, Aaron Galonsky, Scott Pratt, Jon Pumplin and Jack Baldwin for serving on my guidance committee.

Much gratitude goes to the collaborators on the thesis experiment: Aaron Galosky, the group from Rikkyo University (K. Ieki, Y. Iwata, Y. Higurashi, S. Takeuchi) , and the group from Hungary (F. Deák, Á. Horváth, Á. Kiss, and Z. Seres).

I would like to thank all of the NSCL faculty, graduate students, and staff for making this such a friendly place to work. I will not forget the time I have spent here in Michigan.

CONTENTS

LIST OF TABLES

LIST OF FIGURES

Chapter 1

Introduction

1.1 Overview

There has been much interest in the study of the exotic nuclei far from stability in recent years, and much of that focus has been on the light neutron-rich isotopes. Figure 1.1 is a chart illustrating the known bound nuclear systems, and Figure 1.2 is a similar chart for the light nuclear systems. In nature, there are under 300 stable nuclei, and the region they occupy in the chart is known as the "valley of stability". Generally, as nuclei approach the driplines, they become increasingly unstable. Nuclei beyond the dripline region are unstable with respect to nucleon emission, and experimentally difficult to study. The objective of this work is to explore a technique for the study of such unbound systems through the use of final-state interactions. In some cases, the products emerging from the reaction interact strongly with each other, and this phenomenon is known as final-state interaction. By modeling the interactions in the final-states, it permits the deduction of the nature of the interactions in the unbound systems. This technique, as we will show, permits the probing of various neutron-rich unbound nuclei, and offers new insight into their structure. In this work, details of this technique will be discussed, and the results of the unbound ^{7,9}He and ^{10}Li be

presented.

1.2 Spectroscopic Techniques for Bound and Unbound Nuclei

In a conventional nuclear physics experiment, the nucleus of interest is produced in a stable target, which is probed by a nuclear beam delivered by an accelerator. Thus, the accelerator is a physicist's microscope to examine the details of nuclear interaction. However, targets cannot be made to produce neutron-rich nuclei near the dripline because these nuclei are very short-lived. This problem is solved by the use of radioactive beams. Using a radioactive beam to interact with a stable target has exactly the same physics as using a stable beam probing a radioactive target (if such target were available). Because the measurement is made with respect to the projectile's frame instead of the target's, this technique is commonly referred to as "inverse kinematics". The radioactive beam is a very powerful tool for studying bound and unbound systems near and beyond the dripline. The primary methods of spectroscopy with radioactive beams include: (1) Coulomb excitation, (2) Breakup reactions, and (3) Transfer reactions.

Using radioactive beams in conjunction with Coulomb excitation techniques provides a method to study reduced transition probabilities for the lowest excited states in a model independent-way [1, 2, 3]. With this technique, the incident nucleus is excited by the Coulomb field of the target, and the γ-ray from the de-excitation of the incident nucleus is then detected.

Breakup reactions have also provided many important results in this field. They can be used to measure interaction cross sections, and it was with this technique that the large interaction radius of ^{11}Li was first discovered [4]. In addition, momen-

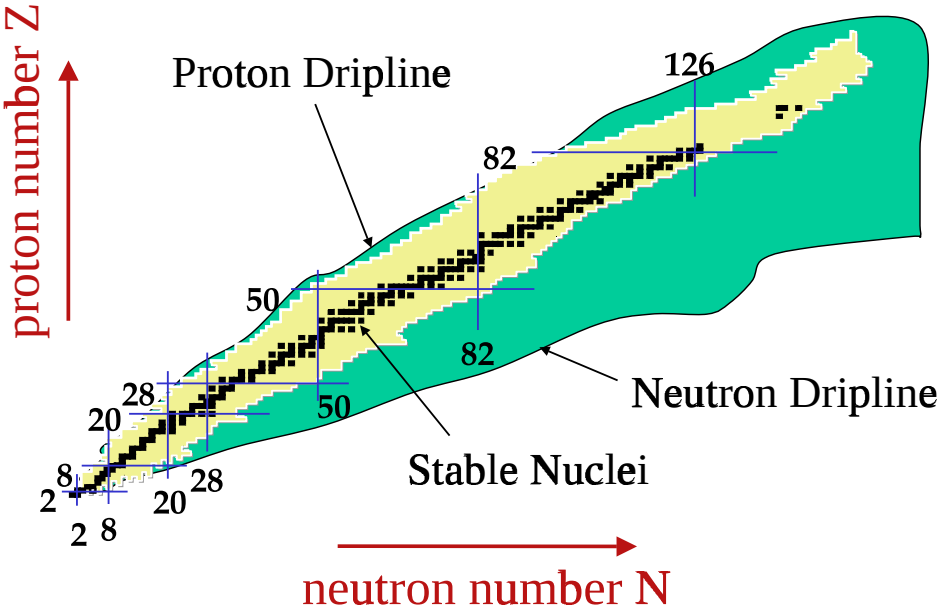

Figure 1.1: Chart of nuclides for bound nuclear systems. Bound nuclear systems are shown here as a function of their proton number Z and neutron number N. The black squares represents the stable nuclei in nature, and these collectively are usually referred to as the "valley of stability". Nuclear binding weakens for nuclei away from stability, and eventually becomes too weak to permit a bound system. The regions where this occurs are referred to as the neutron and proton driplines. Also shown are the known magic numbers for the stable nuclei.

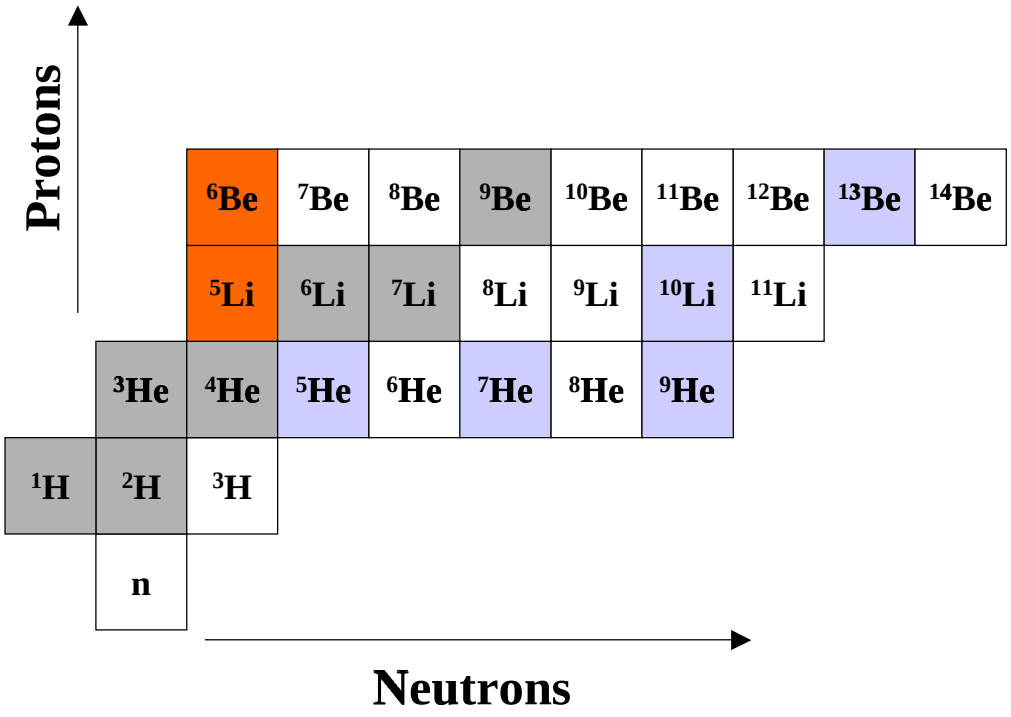

Figure 1.2: Chart of light nuclides. Shown here are the light nuclear systems. The stable systems are shown in gray and particle-stable systems are shown in white. Nuclei unstable to a proton-decay are shown in red, and nuclei unstable to neutron decay are shown in violet. This work is focused on the unbound systems of ^{7,9}He, and ^{10}Li.

tum measurements from breakups have provided important information on nuclear structure. A primary example is in the study of the halo nuclei, where the narrow momentum distribution of the fragment after neutron removal suggests the existence of a diffuse neutron "halo" [5, 6, 7]. More recent experimental work in breakup reactions has been done by [8, 9], where both the γ-ray and momentum distributions of the fragment after a single-nucleon knockout is measured. In this technique, it is possible to identify both the spin and parity of the nucleus.

Transfer reactions can be used to measure masses of both bound and unbound systems. Usually in such experiments, some reaction A(B,C)D is selected, where the masses of A, B, and C are known. Since

$$Q = T_f - T_i = m_a + m_b - m_c - m_d, \tag{1.1}$$

an accurate measurement of the Q-value in conjunction with using reaction participants of well-known masses permits determination of the mass and excited states of the unknown nucleus, assuming that a precise measurement of the momentum is made. The energy at the reaction needs to be very accurately determined, which means that the target needs to be very thin, on order of 1 mg/cm^2 (a 0.4 mg/cm^2 target was used in the ^{7}He experiment [10]). This reaction can involve the exchange of a pion, as in the single charge-exchange reaction ^{7}Li(t,^{3}He)^{7}He used by Stokes and Young [10], or the double charge-exchange reaction of ^{9}Be(π^-,π^+)^{9}He used by Seth *et al.* [13] to study ^{9}He. In addition, these reactions can involve actual transfer of nucleons from one nucleus to another, as in the case of the ^{10}Li studies by [11, 12]. Figure 1.3 shows data from a study of the unbound ^{9}He nucleus from the works of [13, 14].

Of spectroscopy techniques mentioned, only the transfer reaction can be applied to study unbound systems. This is because the techniques of Coulomb excitation and breakup reaction both require a beam of the nucleus of interest be produced in a

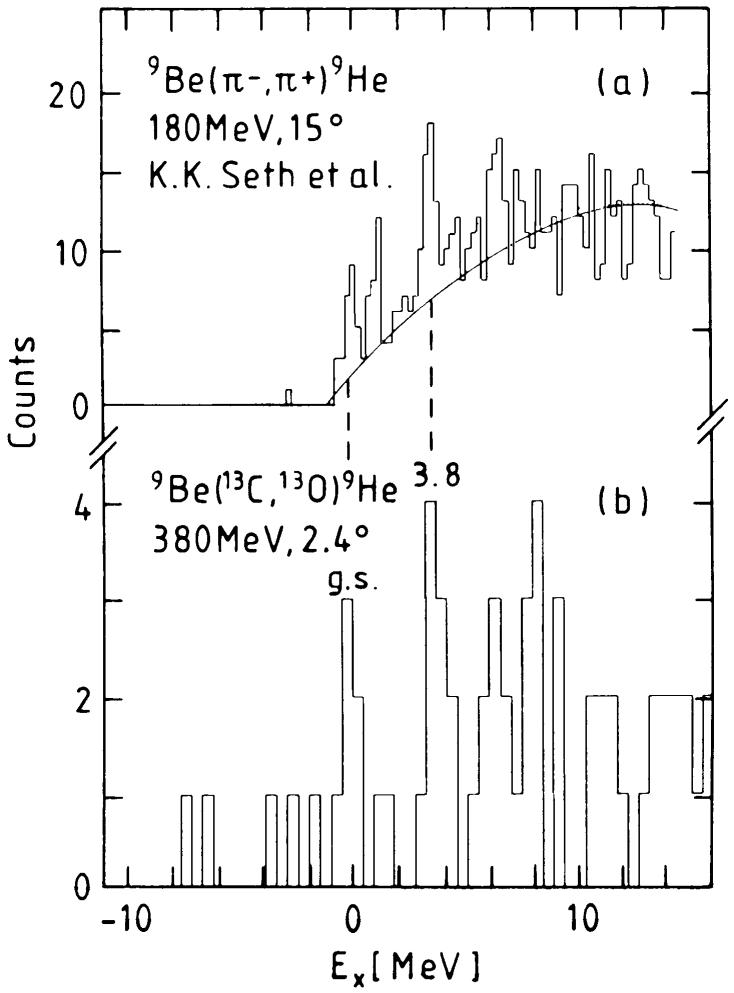

Figure 1.3: Data from Seth *et al.* and Bohlen *et al.*. The upper panel shows the missing-mass spectrum result of a ^{9}Be(π^-,π+)^{9}He reaction at 194 MeV from [13]. The authors reported states at 0, 1.2, 3.8, and 7.0 MeV, using a scale where the energies are measured in reference to the lowest observed state, which has a neutron separation energy of -1.13 $\pm$ 0.10 MeV. The figure in the lower panel shows the results of a ^{9}Be(^{13}C,^{13}O)^{9}He reaction at 380 MeV, where the authors reported a sharp peak for the ground state 1.83 MeV unbound against neutron decay [14]. Our work suggests that the ^{9}He ground state actually is at -1 to 1.2 MeV on the scale shown here.

laboratory. In the case of unbound systems such as ^{7}He, the lifetime is on the order of 10^{-21} second or less, which implies that an unbound nucleus would travel roughly 30 times the nuclear radius after being formed from a reaction. Instead of using transfer reactions, this work approaches the problem of unbound systems through the use of final-state interactions. A beam of a well-understood nucleus fragments at the target and then populates states of various unbound systems. The interactions of the post-reaction fragments are simulated by a potential scattering model, and the nature of the interaction of the unbound nucleus is deduced.

1.3 Previous Use of Final-State Interactions

Final-state interactions have played an important role in the study of the neutron-neutron interaction [15, 16, 17, 18]. A convenient way to describe the neutron-neutron interaction in a low energy scattering process involves the quantity scattering length, which describes the range of an interaction. More on scattering length will be given in Chapter 4. At the beginning, it was understood that accurate determination of the neutron-neutron scattering length along with the proton-proton scattering length will help to determine the charge dependence of the strong nuclear force. Today, the charge symmetry of the strong forces is well-documented [19], and the quantity $\triangle a = a_{nn} - a_{pp}$ is a direct measure of charge-symmetry-breaking [20]. This is the reason why experiments are still being performed today trying to further ascertain the value of a_{nn} even though the first measurement was made over forty years ago.

While the nature of the proton-proton interaction can be deduced by a direct nucleon-nucleon scattering process, a neutron-neutron scattering experiment is technically impossible. As a result, the only viable means was to use the final-state interaction to probe the n-n interaction. It was suggested over forty years ago that breakup reactions would be very important for the study of the neutron-neutron interaction

[21, 22]. The early attempts to study the neutron-neutron scattering length a_{nn} used the ^{2}H(n,p)2n reaction [23, 24, 25]. In these experiments, the proton spectra exhibit two peaks at angles near zero degrees. These experiments are complicated to analyze because proton-neutron and neutron-neutron interactions (as measured by scattering length) are on the same order of magnitude, and the three-body nature of the exit channel provides additional complications. Consequently, there have been fairly large discrepancies among results from 3-nucleon reactions [20]. To address these problems, there are experiments which use the reaction $^2H(\pi^-,\gamma)2n$ [15, 20, 26]. This reaction is superior because only two of the three particles in the exit channel are strongly interacting. Regardless of which reaction one uses to study a_{nn}, a theory that accounts for the final-state interaction between the neutrons is used to interpret the data.

The use of final-state interactions (FSI) in the studies of a_{nn} has provided many useful results since the first experiment. Currently, the world average value for a_{nn} is -18.59 ± 0.27(experimental)± 0.30(theoretical) fm [20]. It is the purpose of this work to show that FSI is also a viable way to study the neutron-rich unbound nuclei.

1.4 Studies of Unbound Nuclei with FSI

There have been two previous experiments that used the FSI to study unbound nuclei in the literature [27, 28], and both of them were performed at the NSCL. The aim of both of these experiments was to search for the low-lying states of ^{10}Li, which is critical for the understanding of the ^{11}Li two-neutron halo.

The isotope ^{10}Li is an N=7 isotone, which is a member of a family of nuclei with seven neutrons. The systematics of the level crossing of the N=7 isotones is shown in Figure 1.4. It is a very well documented fact that ^{11}Be, the lightest bound N=7 isotone, is the crossing point where parity inversion occurs, and that the ground-state of ^{11}Be is actually an intruder s-state, and not the p-state that would be predicted

by a simple shell model. It has been suggested by Sagawa *et al.* that this inversion phenomenon would continue for the lighter and unbound N=7 isotones [29], suggesting that the low-lying states of ^{10}Li may be a *s*-state. An experimental observation of the ^{9}He would also help to establish this trend.

The first experiment, by Kryger *et al.* [27] (Figure 1.5), probed the ^{10}Li through the use of sequential decay neutron spectroscopy. In that experiment, an incident 80 MeV/u ^{18}O beam irradiated a carbon target, and coincident events between neutron and ^{9}Li were detected in a collinear arrangement. It is assumed that by fragmenting an initial nucleus, it is possible to populate many unbound states, including ^{10}Li. This first experiment observed a ^{10}Li state that corresponded to either a ground state or, if this feeds an excited state of ^{9}Li, then to an excited state with $E_x \approx 2.7$ MeV. The second experiment, by Thoennessen *et al.* [28], was a repeat of the Kryger experiment, but with improved resolution (Figure 1.6). The scattering length of the observed low-lying *s*-state was established to be $a_s < -20$ fm for ^{10}Li.

1.5 The Objectives of This Work

The present work has three objectives. The first is to investigate the influence of the initial state and to demonstrate the selectivity of the method. This was done with ^{10,11,12}Be as projectiles. The results show that, as expected, the observed momentum distributions depend on how the product was formed. (This shows that it is necessary to go beyond a picture where ^{10}Li is formed as a separate identity, which much later decays in flight. This picture would obviously be correct for a very narrow resonance.)

The second objective is to repeat the experiments by Kryger *et al.* and Thoennessen *et al.* [27, 28] with a set of different initial nuclei. This will help to establish that the previously observed interaction in the $l = 0$ channel is not an artifact of the initial nucleus; since the ^{18}O and the ^{12,11}Be have very different structures. The

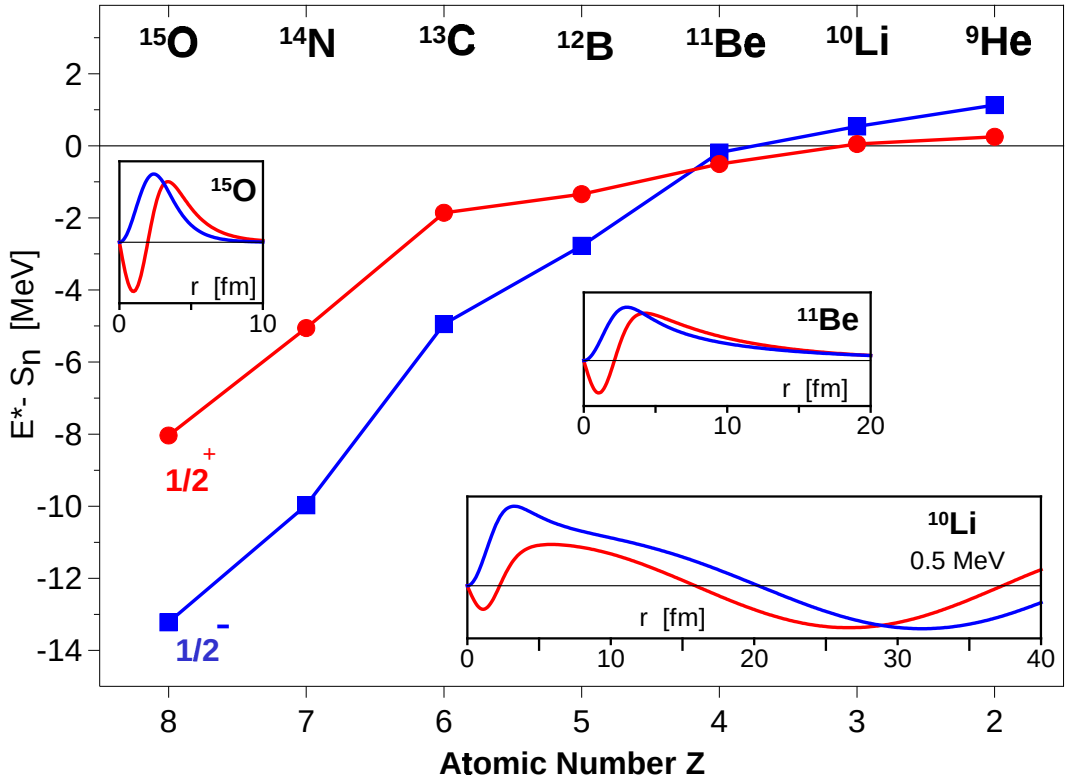

Figure 1.4: Shown here is the systematics of the level crossing in the N=7 isotones. In the y-axis is the eigenvalue energy of the $\frac{1}{2}^-$ and $\frac{1}{2}^+$ states, which is the difference between the energy of the state(E^*) and the neutron separation energy (S_n). Shown in the insets are the wave functions $\chi(r) = rR(r)$ of corresponding single particle states calculated with a Woods-Saxon potential. The ^{15}O is very tightly bound, while the ^{11}Be is very loosely bound (as evident by the long tail in the wave function), and the unbound ^{10}Li is characterized by a scattering wave. The nuclei ^{10}Li and ^{9}He are studied in the present work, which suggests s states at $\leq$ 50 and $\leq$ 200 keV, respectively. The p state shown for ^{10}Li is that discussed in the works of Caggiano *et al.* [12]. The state near 1.1 MeV in ^{9}He has been observed in the double charge exchange reaction and in multinucleon transfer.

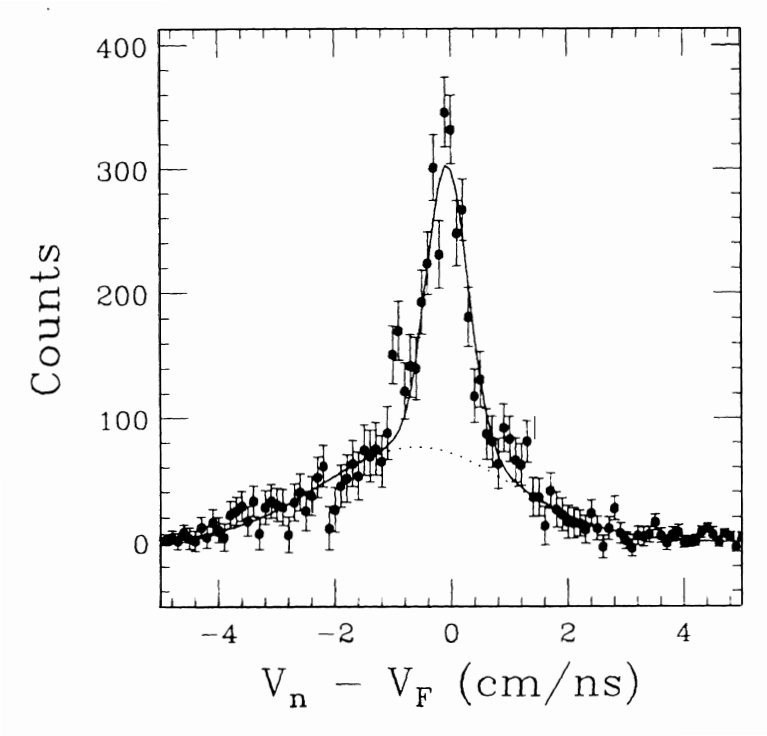

Figure 1.5: Data from Kryger *et al.* [27]. The relative velocity of the ^{9}Li+n system is fitted with an estimated background and a simulated velocity difference distribution from a computer simulation which included the experimental resolution, acceptance, and efficiencies. The fit shown is for a resonance with $E_r = 50$ keV and $\Gamma = 100$ keV. The authors concluded that the state was either a ^{10}Li ground state or an excited state with $E_x \approx 2.7$ MeV.

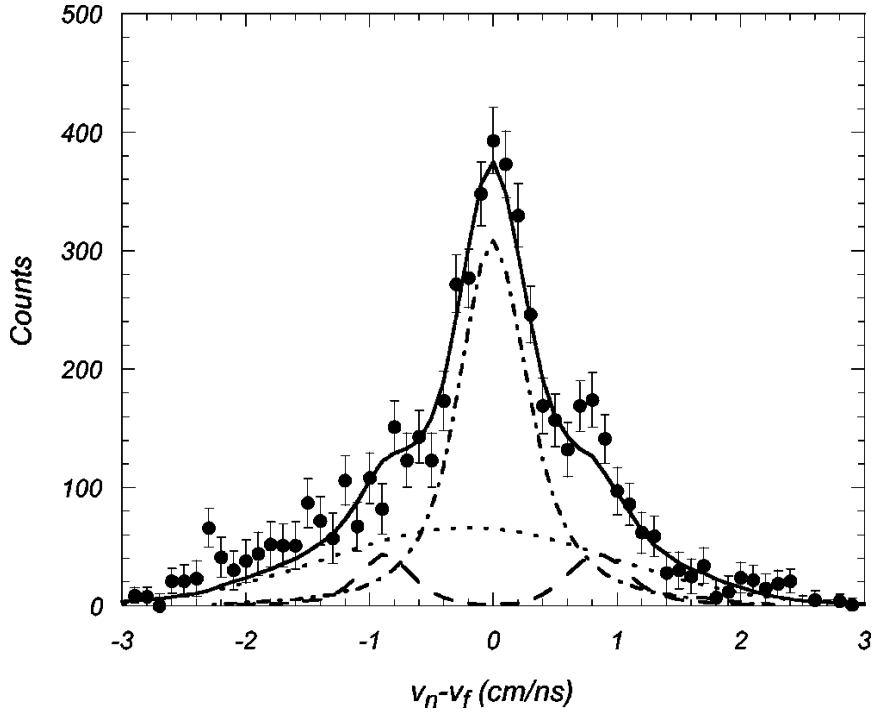

Figure 1.6: Data from Thoennessen *et al.* [28]. Shown here are the computer simulation results (solid), which include contributions from an s-wave with $a_s = -30$ fm (dot-dashed), p-wave with $E_r = 538$ keV (dashed), and estimated background (dotted). The essential feature of this data is the pronounced peak at zero relative velocity, which is interpreted as a low-lying s-state with an $a_s < -20$ fm.

results confirm the finding by Kryger *et al.* and Thoennessen *et al.* [27, 28] that in ^{10}Li the lowest neutron state must have the spin and parity $1/2^+$, an intruder from the s, d shell. It has been pointed out by Thompson and Zhukov [30] that the presence of a $1s_{1/2}$ state just above the threshold of the ^{9}Li+n system is essential for the understanding of the binding of the ^{11}Li two-neutron halo. They suggest that an interaction characterized by an s-wave scattering length of the order of -20 fm or numerically larger is required. This is in agreement with the previous experiment [28] and the present work.

The third objective is to look for a low-lying s-state in the ^{9}He. For ^{9}He, there have been resonances observed near 1.2 MeV (and also at higher energies) by Seth *et al.* [13] and by von Oertzen *et al.* [32]. The mass assignment given for ^{9}He by Audi and Wapstra [31] is based on the weighted average of these two observations. The data presented in this work suggests that the lowest state, missed in the previous work, has l=0 and lies approximately 1 MeV lower.

1.6 Outline

The remainder of this work is based on the results from experiment 97017, which is the third experiment to study the unbound nuclei ^{7}He and ^{10}Li using FSI. The details of the experimental setup will be covered in Chapter 2. A detailed discussion regarding the theoretical model, and the calculation of the final-state interaction is presented in Chapter 4. Chapter 3 discusses the data reduction procedures, including aspects of detector calibration and proper event selection. Chapters 5, 6, and 7 contain the results for ^{7}He, ^{10}Li, and ^{9}He respectively.

Chapter 2

Experiment 97017

The experiment was performed in the NSCL N4 vault between 8/14/97 and 8/22/97. Subsequent sections provide details regarding various technical aspects of the experiment.

The primary beam of came from the cyclotron, and the radioactive beam was produced in the A1200 fragment separator. The radioactive beam was then directed to the N4 vault through a sequence of magnets in the transfer hall. Figure 2.1 shows the layout of the apparatus.

This experiment requires kinematic measurement of both the charged fragments as well as the neutrons produced from the fragmentation. The neutrons were detected using the two NSCL Neutron Walls [33]; two large arrays of position-sensitive neutron detectors. The first neutron wall was placed 5 meters from the target position in the forward direction, and the second wall was 0.5 meters immediately behind the first. The fragments produced in reactions in a ^{9}Be target were deflected away from the Neutron Walls with a 1.5 Tesla sweeping magnet. Particle identification of the fragments was achieved with a two dimensional gate on the energy-loss, which was measured by an array of 58.2 mg/cm^2 silicon-strip detectors, and the total energy, which was measured by an array of sixteen plastic scintillator detectors downstream

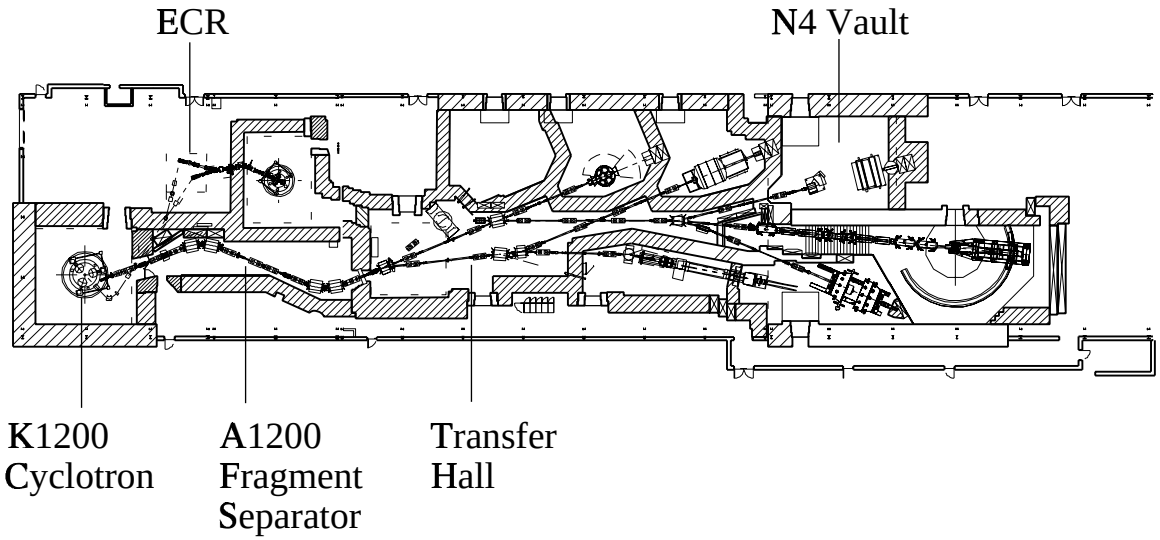

Figure 2.1: Schematic of the NSCL. The primary beam from the K1200 cyclotron reacts with a production target in the A1200 fragment separator, which then produces the radioactive beam used in this experiment. The secondary beam is directed to the N4 vault by the magnets in the N4 vault.

from the target. The neutron energy was determined by a time-of-flight measurement. A thin, fast plastic detector was placed in the flight path after the production target and before the beam enters our experimental vault to provide an event-by-event identification of our secondary beam.

The details of the apparatus will be discussed in subsequent sections in this chapter. Figure 2.2 shows the layout of the experimental vault.

2.1 Radioactive Beam

This experiment was performed at the NSCL using a secondary beam of 30 MeV/u ^{12,11,10}Be on a 200 mg/cm^2 ^{9}Be target. The mid-target energy of the secondary beams is estimated to be 27.9, 27.7, and 27.5 MeV/u for ^{12,11,10}Be respectively. These radioactive beams were produced with the projectile fragmentation technique. Generally, the production of a radioactive beam with this technique uses a primary beam which is broken up at a production target, and the reaction fragments are subse-

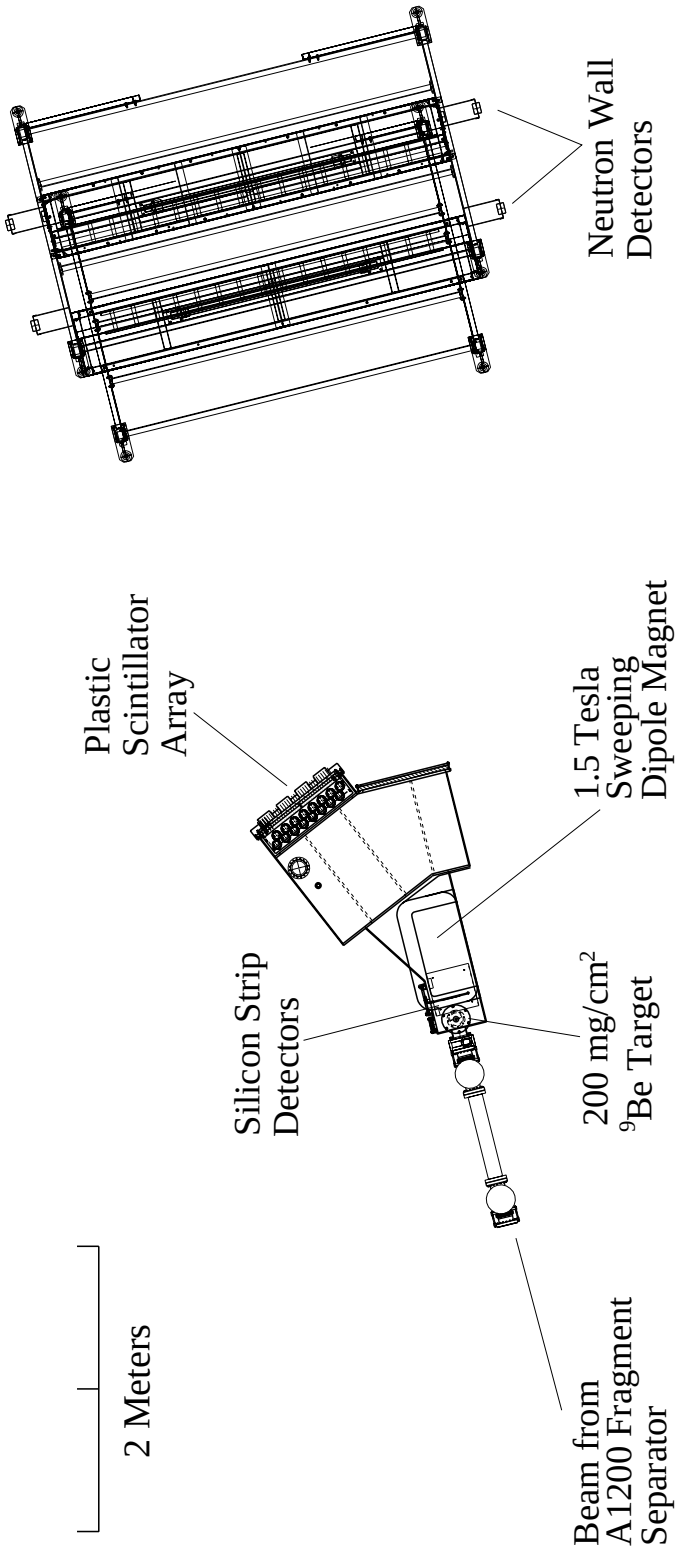

Figure 2.2: Experimental setup at the N4 vault of the NSCL.

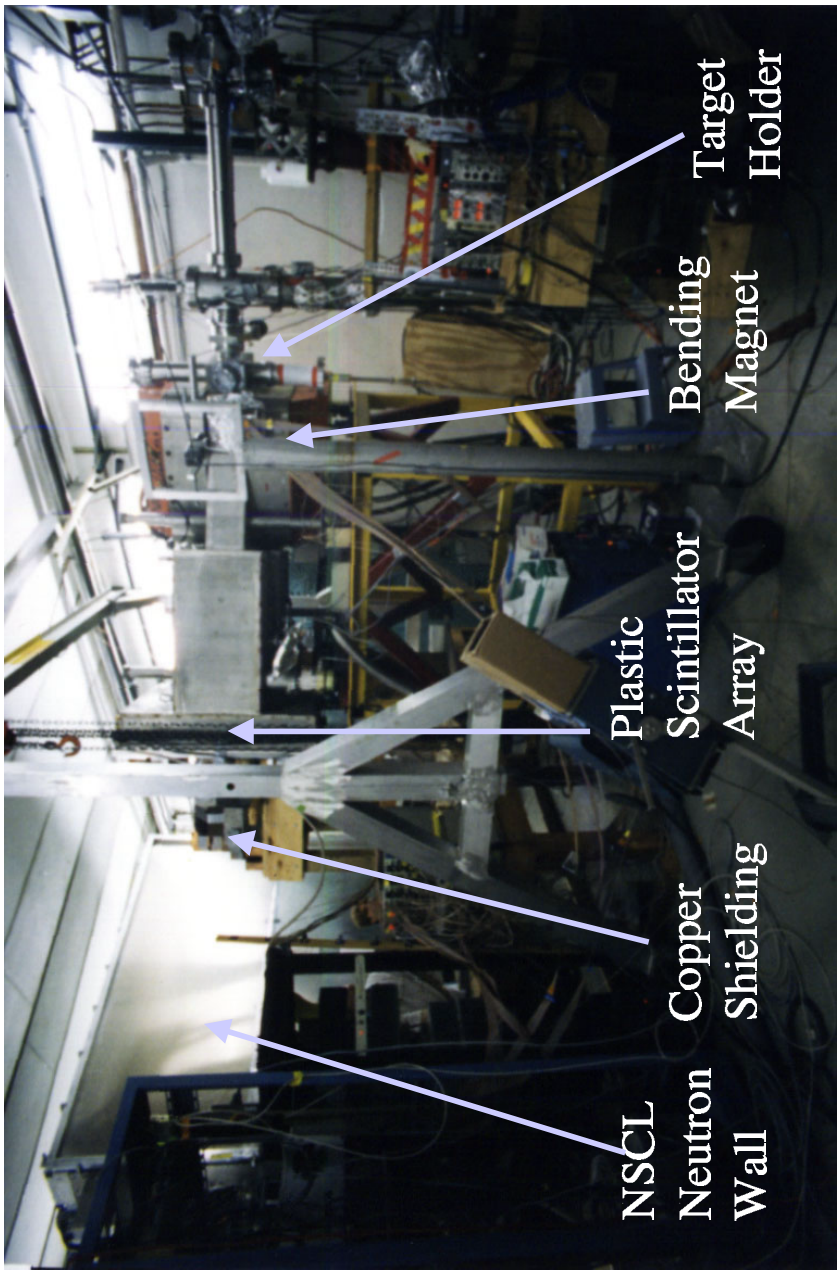

Figure 2.3: Photograph of N4 Vault

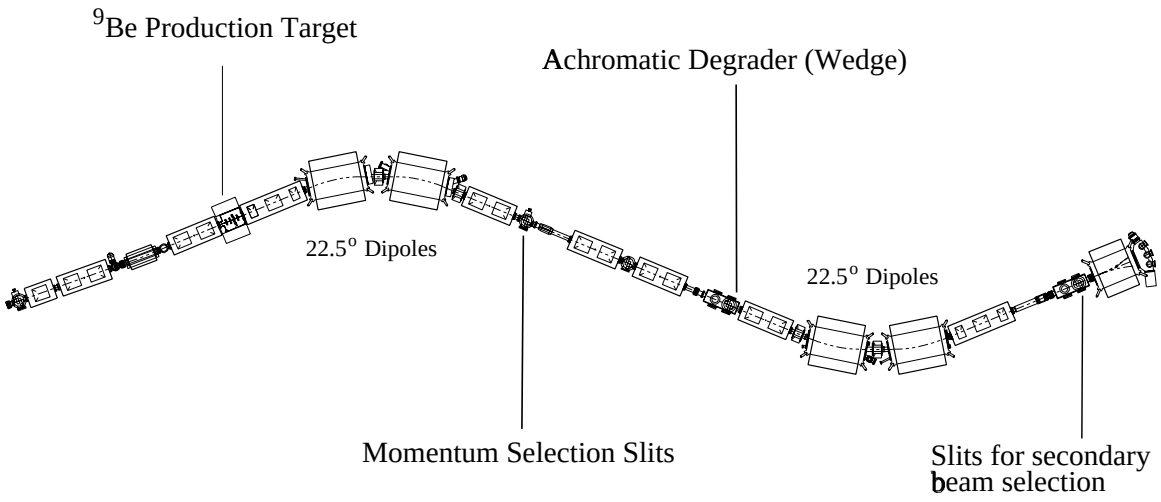

Figure 2.4: The A1200 Fragment Separator. (Figure courtesy of NSCL design group)

quently purified by a series of dipole magnets and an energy-loss degrader. In this experiment, the primary beam was produced by the K1200 cyclotron. The ^{12}Be secondary beam was produced using a primary beam of 80 MeV/u ^{18}O at 150 pnA on a 1455 mg/cm^2 ^{9}Be production target, and is purified with the A1200 fragment separator with a 725 mg/cm^2 ^{27}Al degrader. The production of the ^{11}Be and ^{10}Be secondary beams was accomplished with an 80 MeV/u ^{13}C primary beam with a beam current of 75 pnA on a 1900 mg/cm^2 ^{9}Be production target, degraded with a 233 mg/cm^2 (^{11}Be) and a 525 mg/cm^2 (^{10}Be) Al degrader. Momentum slits were set to 3% for ^{12}Be, and to 1% for ^{11,10}Be. Figure 2.4 shows a schematic of the A1200.

2.2 NSCL Neutron Walls

The neutrons were measured by the NSCL Neutron Walls, which are two large-area position-sensitive neutron detectors designed and built at the NSCL. Details of the construction and various technical aspects can be found in [33]. Each of the Neutron Walls consists of twenty-five Pyrex glass cells which are filled with NE-213 liquid scintillator, which has the dimensions of 200 cm wide, 7.62 cm high, and 6.35 cm thick.

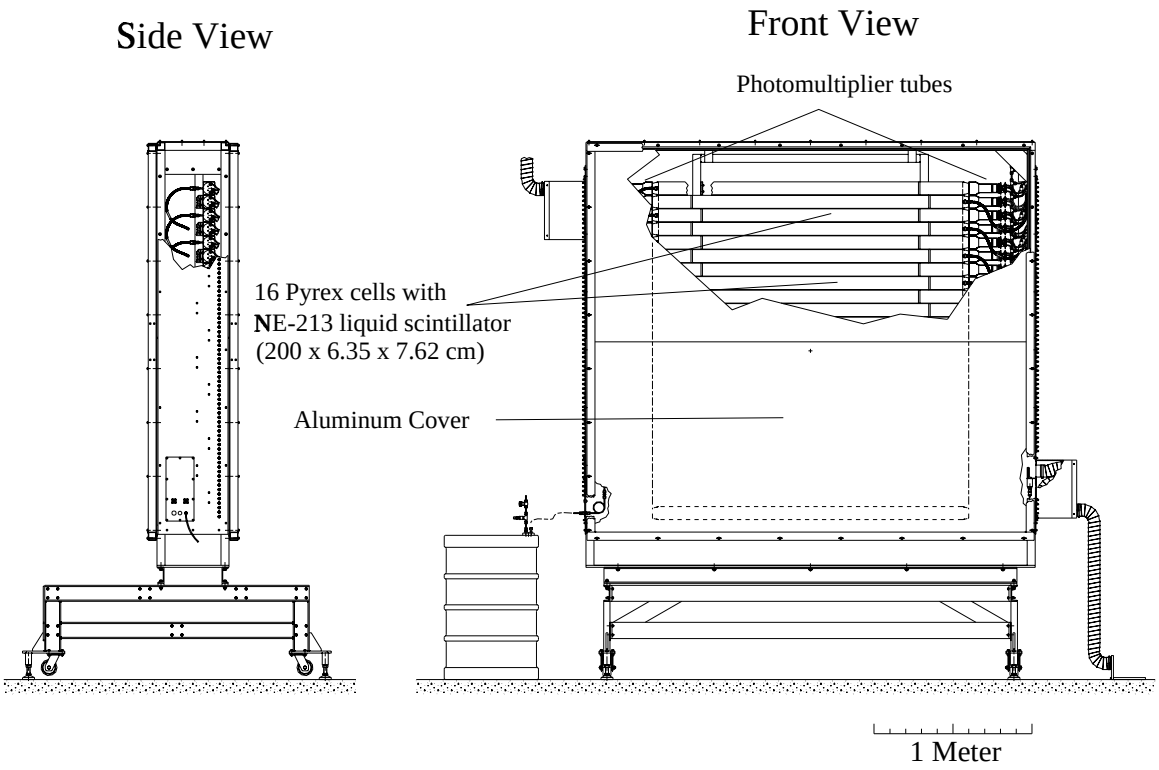

Figure 2.5: NSCL Neutron Wall Detectors. (Figure courtesy of NSCL design group)

The center-to-center distance between the detectors is 8.55 cm. These rectangular cells are tapered to a circle of 7.5 cm diameter, and a photomultiplier tube (PMT) of the same diameter is attached to the cell with optical epoxy. A large aluminum frame secures these cells to each other, and an aluminum covering shields these detectors against ambient light.

During the experiment, the two neutron walls were arranged at zero degrees with respect to the incident beam. In positioning the Neutron Wall detectors in a back-to-back manner, we approximately double the detection efficiency without sacrificing the position resolution from having a singular neutron detector with twice the thickness.

2.3 Plastic Scintillator Array

The total energy measurement is made by the plastic scintillator array. The array consists of sixteen BC408 plastic scintillators, each with the dimensions of 40.64 x 4 x 2 cm. It is positioned with its normal at approximately 23 degrees to the beam direction, with the scintillators approximately 170 cm from the target position. Each of these scintillator bars has one PMT attached to each end of the plastic scintillator. Although the PMTs are larger than the plastic scintillators, it is possible to arrange the plastic scintillator so that there is no dead space in the array by using a staggered arrangement. The scintillators are arranged in two parallel planes 4.75 cm apart. The plastic scintillator bars are not optically shielded from each other, so it is possible for the light output from one detector to scatter to a neighboring detector. Even though the array is placed outside the magnet, it is necessary to shield the PMTs from the external magnetic field with μ-metal shields.

Previous experiments have shown that beam interaction with the fragment scintillators can produce a considerable amount of neutrons. Only neutrons produced from the reactions with targets are of interest, so copper bricks were placed immediately behind the plastic scintillators to shield the neutron wall from these neutrons.

2.4 Silicon Strip Detector

In addition to the total energy, an energy-loss signal ($\triangle$E) is needed for particle identification. This signal is provided by the silicon strip detectors. There are two silicon strip arrays, each is a 250 μm thick square with 5 cm sides. There are thirty-two 3.125 mm strips in each detector, with sixteen strips in each of the horizontal and vertical directions. The silicon strip detector is placed 15.24 cm behind the the target position, so each silicon strip corresponds to a solid angle coverage of approximately

1.2 degrees. The two silicon strip arrays are placed side by side to increase coverage after the target, with a 2 mm gap between the detectors.

2.5 Sweeping Magnet

The secondary beam and the reaction fragments are deflected away from the neutron wall by the 1.5 Tesla sweeping magnet. The magnet has a 7.5 inch gap with pole faces that are 13 inches wide and 26 inches long. Originally, this was a 1.7 Tesla magnet at the Bevalac with a 6.5 inch magnet gap. The gap was extended to increase the acceptance of the Neutron Walls [34].

Both the plastic scintillator detector and the silicon strip detectors are housed in a vacuum chamber that fits inside the gap of the sweeping magnet. The silicon strip detector sits inside the magnet gap and has to be water-cooled because the magnet generates a considerable amount of heat. The target pod is attached to the front of the chamber.

2.6 Electronics Setup

The mastergate is generated when there is a coincidence between the event in the Neutron Walls and the fragment detectors. If a coincidence event is detected, a veto signal is sent to the electronics to give the computer time to read out the TDCs and the ADCs. However, if there is no coincidence, then only 1 out of N times (where N is the downscale factor set) will the event be recorded. In other times, a FAST CLEAR signal is sent to reset the electronics to allow new data to be recorded. The downscaled data is used to determine the absolute normalization of the data.

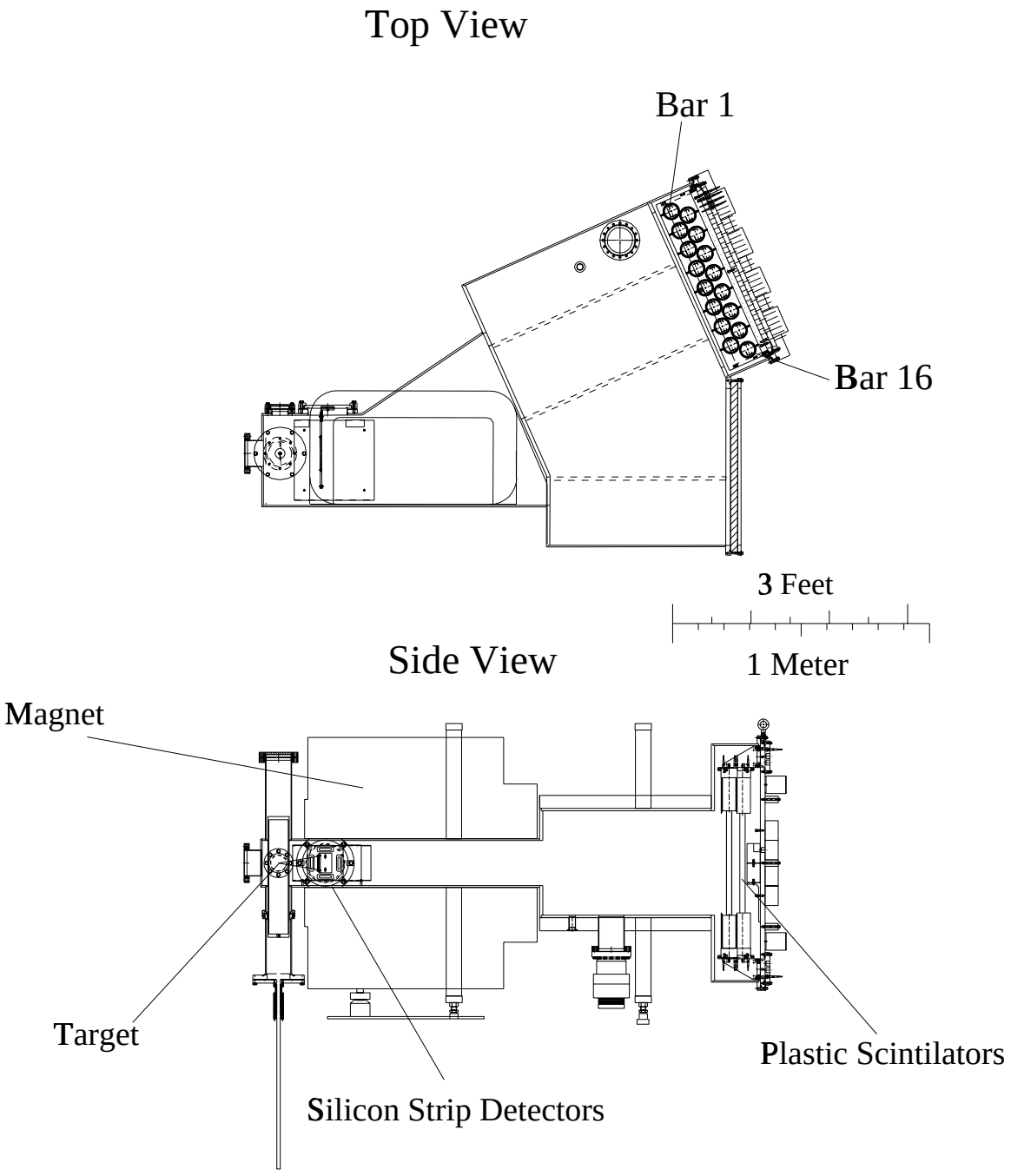

Figure 2.6: Bending Magnet and Fragment Detector Array.

Chapter 3

Data Analysis

3.1 Velocity Difference Analysis

The main objective of this experiment is to measure the energy of unbound states in a two-body system. In the center of mass system, the total kinetic energy of a two-body system is given by the relation

$$E_r = \frac{1}{2}\mu V_{rel}^2 \tag{3.1}$$

where the μ is the reduced mass, and V_{rel} is the relative velocity between the fragment and neutron. Thus, a measurement of the relative velocity is also a measurement of the energy of the system. The relative velocity in the center-of-mass system can be related to quantities measured in the laboratory frame. Looking at Figure 3.1, it is apparent that $\mathbf{V_{rel}} = \mathbf{V_f} - \mathbf{V_n}$. For a small θ, $|V_{rel}| = V_f - V_n$, where the difference between V_f and V_n is simply a scalar difference of the fragment and neutron velocities. Both the neutron and fragment velocities are measured quantities in this experiment. Previous FSI experiments [27, 28] have used a collinear geometry to detect a neutron in coincidence with a fragment. The neutron detectors were 12.7 cm in diameter, which represents a solid angle coverage of 1.15 msr [36]. The neutron walls

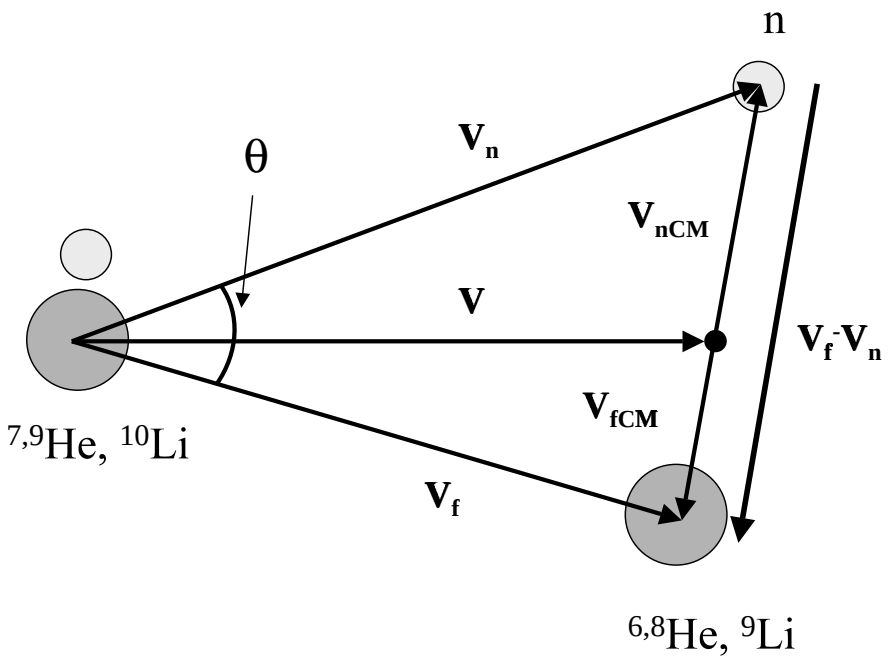

Figure 3.1: Kinematic diagram of the core+n two-body system. $\mathbf{V}$, $\mathbf{V_n}$, $\mathbf{V_f}$ denotes respectively (in the lab frame), the velocity of the fragment+n system, neutron, and fragment velocities. $\mathbf{V_{nCM}}$ and $\mathbf{V_{fCM}}$ denotes (in the center-of-mass frame) the neutron and fragment velocities. For small θ, $V_{rel} = V_f - V_n$

offer greater detection efficiency because of greater angular coverage. The increased angular coverage also affects the way data is analyzed, and the details of the analysis will be presented in this section.

In this experiment, only neutrons which are detected within five degrees of a detected fragment are analyzed. Assuming that the coordinates of the fragment and the neutron are given as $\mathbf{X_f}(x_f, y_f, z_f)$ and $\mathbf{X_n} = (x_n, y_n, z_n)$ respectively, then the relative angle between the two is simply:

$$\theta = \cos^{-1}\left(\frac{\mathbf{X_f} \cdot \mathbf{X_n}}{|\mathbf{X_f}|\,|\mathbf{X_n}|}\right) \tag{3.2}$$

The choice of angular cut θ is a compromise between energy resolution and number of events. A smaller angular separation between the fragment and the neutron would improve the resolution of the velocity difference distribution, but a larger angular cut would increase counting statistics at the cost of sacrificing resolution. Figure

3.2 shows the detection probability as a function of velocity difference of the two-body system with masses corresponding to a ^{6}He+n system decaying at 440 keV, which is the current tabulated value for the decay. The simulation accounts for the detector size, acceptances (including the shadowing from the magnet), and resolutions of the experimental setup, so the use of a mono-energetic energy distribution gives an idea of the resolution of the experimental apparatus. The asymmetry of the two peaks is caused by acceptance effects, because neutrons moving faster than beam velocity are more likely to be found within angle θ of a fragment than those neutrons moving more slowly. Ideally, the velocity difference distributions would have two sharp peaks at the velocity corresponding to the decay energy and minimal intensity at zero relative velocity. This figure shows that a five degree cut offers a good combination of resolution and counting statistics for the ^{6}He+n system.

The analysis using the relative velocity distribution of an unbound two-body system has some inherent advantage over using an invariant mass spectra. The energies of interest are on the order of a few hundred keV or less, and an analysis using relative velocity accentuates the sensitivity in this low energy region. As shown in the energy scale on Figure 3.2, the window between -1 and 1 cm/ns represents 0 to 500 keV for a system with mass parameter corresponding to a ^{7}He. For very small energies, even though the peaks may not be fully resolved (as shown in Figure 3.3), there is a very significant change in the line shape of the distribution. This is important for the low-lying s-states in both the ^{10}Li and ^{9}He.

The relative velocity distributions corresponding to the s-state for the ^{9}Li+n and ^{8}He+n systems are shown in Figures 3.4, 3.5, 3.6, and 3.7. These calculations used energy distributions computed from the technique that will be described in Chapter 4. Without going into much detail at this point, it is sufficient to mention that a numerically larger scattering length a_s corresponds to a stronger final-state interaction,

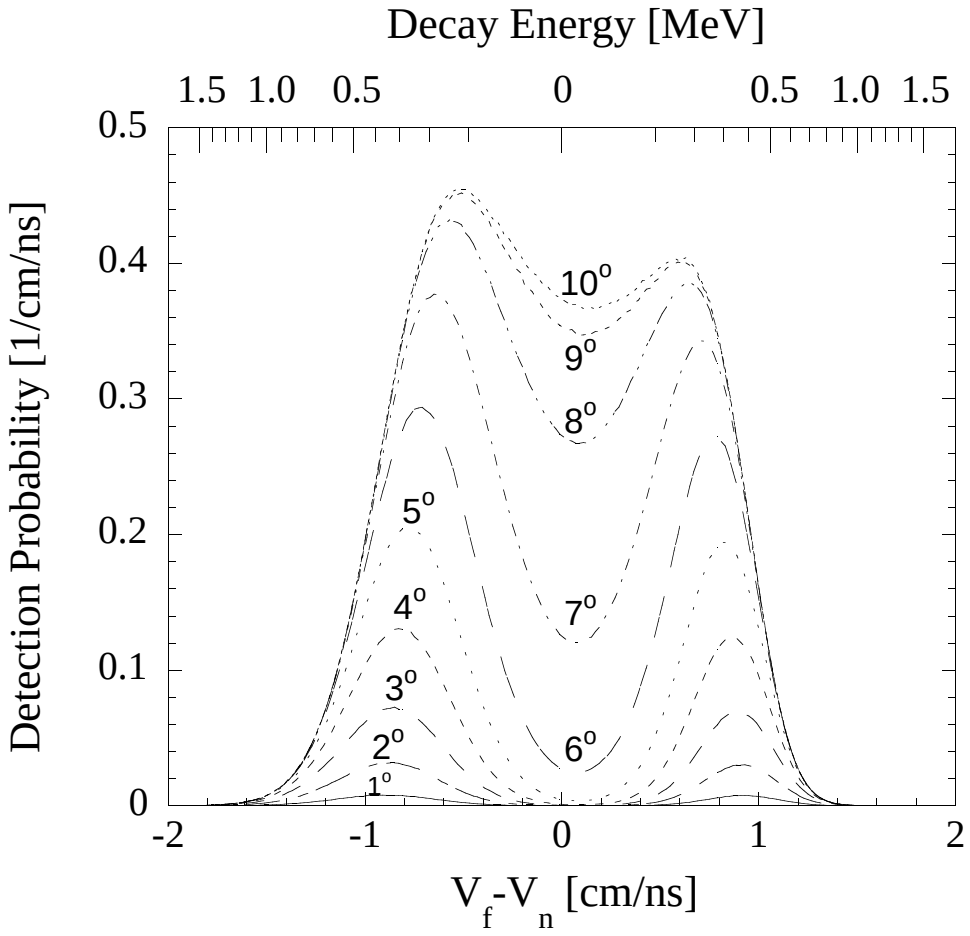

Figure 3.2: Detection probability of decay of a two-body system with the mass parameters of ^{7}He with a sharp energy distribution $E_r = 440$ keV. Shown is the detection probability as a function of angular cut for the fragment-neutron coincidence event. For comparison, an x-axis containing the energy scale is also shown this relative velocity distribution. The calculations here include acceptance effects (including the shadowing of the magnet) as well as resolution effects. As the angular acceptance increases, the resolution deteriorates as the two peaks eventually merge together. Ideally, there should be no intensity in the region of $V_f - V_n = 0$, but as the angular cut expands to much beyond 5^0, the contribution in that region becomes significant due to poorer resolution.

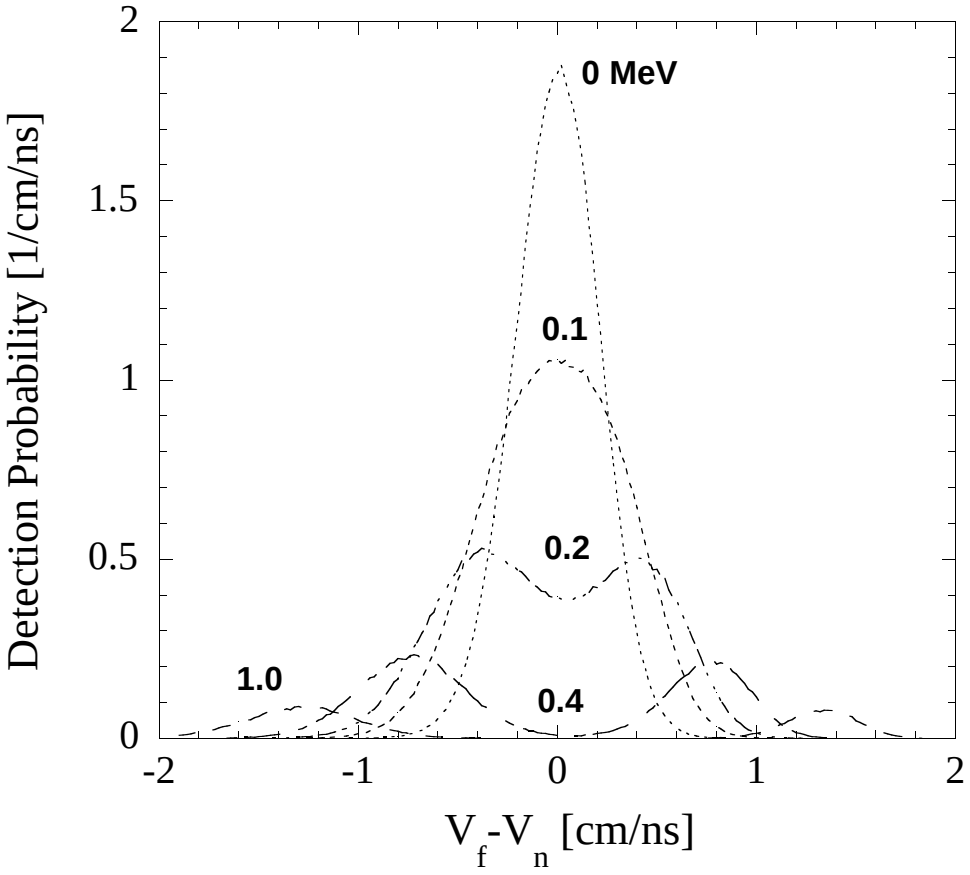

Figure 3.3: Detection probability of decay of a two-body system with the mass parameters of ^{7}He with sharp energy distributions. Shown is the detection probability as function of decay energy, and in all cases, the angular cut is fixed at 5^0. This calculation includes all acceptance and resolution effects of the experimental apparatus. The method of using velocity difference is very efficient for low energy events and the efficiency decreases for higher energy. At around $E_r = 0.2$ MeV, it becomes possible to resolve two separate peaks from the velocity difference spectra.

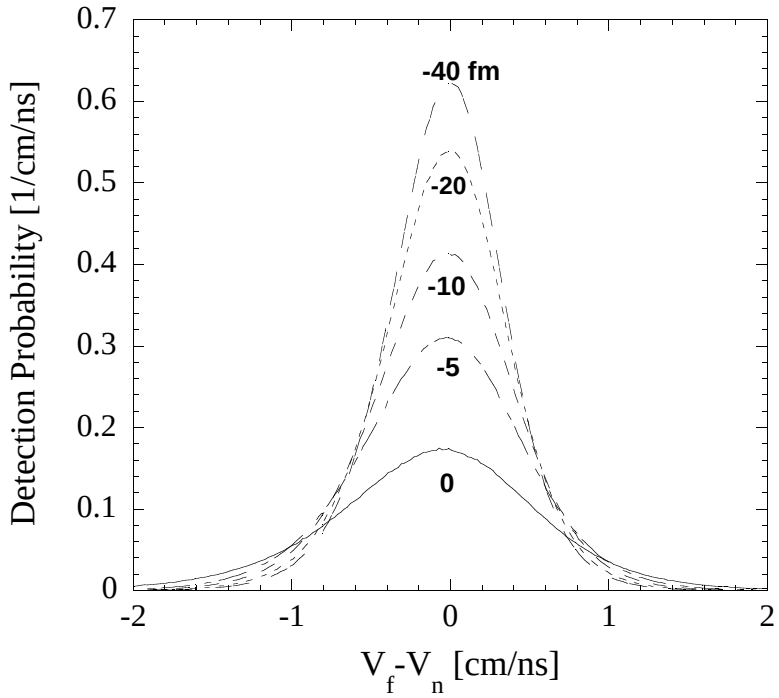

Figure 3.4: Detection probability of a ^{9}Li+n system breaking up isotropically after being formed from ^{11}Be. Shown here are calculated velocity distributions for $a_s = 0, -5, -10, -20, -40$ fm for a 5^0 angular cut.

which corresponds to a more narrow relative velocity distribution. Figures 3.4 and 3.5, show the detection probability as a function of velocity difference of some select a_s for the ^{9}Li+n system. Figures 3.6, and 3.7 show the total detection probability for events to falls into different angular cuts for various scattering lengths. Larger angular cuts will reduce the sensitivity for larger numerical scattering lengths since the contribution from zero decay energy increases with numerically larger scattering length.

Figures 3.8 and 3.9 show the same calculations for the ^{8}He+n system breaking up from an initial ^{12}Be. It demonstrates that even at a 10-degree angular cut, there was sufficient sensitivity to detect the difference among different scattering lengths. This is important because in the case of ^{8}He+n system there is limited counting statistics, and it will be necessary to increase the size of the angular cut.

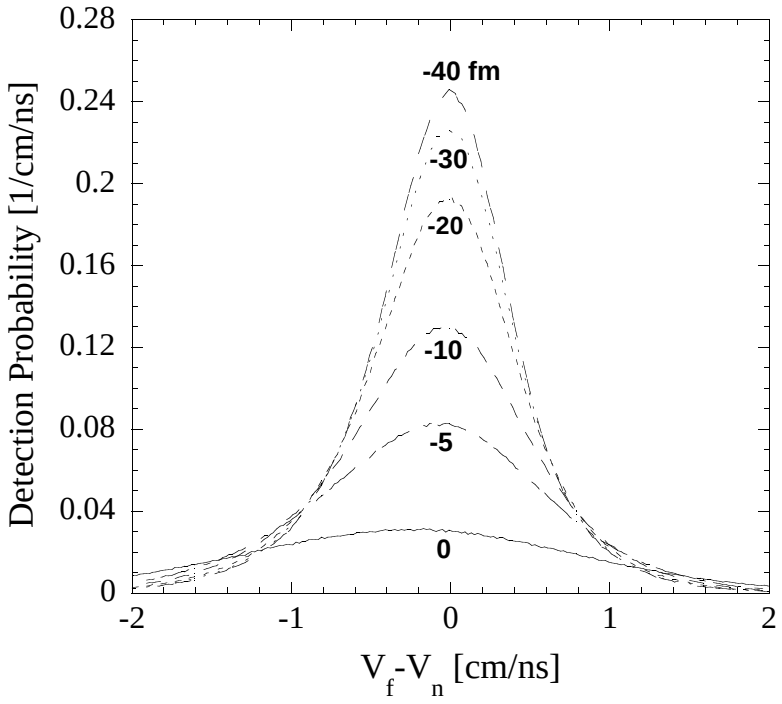

Figure 3.5: Detection probability of a ^{9}Li+n system breaking up isotropically after being formed from ^{12}Be. Shown here are calculated velocity distributions for $a_s = 0, -5, -10, -20, -30, -40$ fm for a 5^0 angular cut.

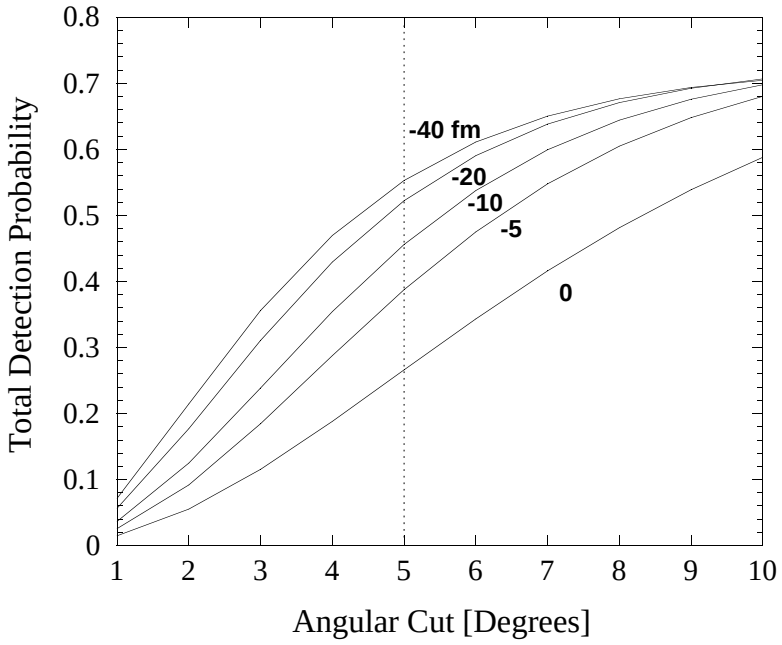

Figure 3.6: Total detection probability of a ^{9}Li+n system breaking up isotropically after being formed from ^{11}Be. Shown here are curves for $a_s = 0, -5, -10, -20, -40$ fm as a function of angular cut for neutron-fragment coincidence events.

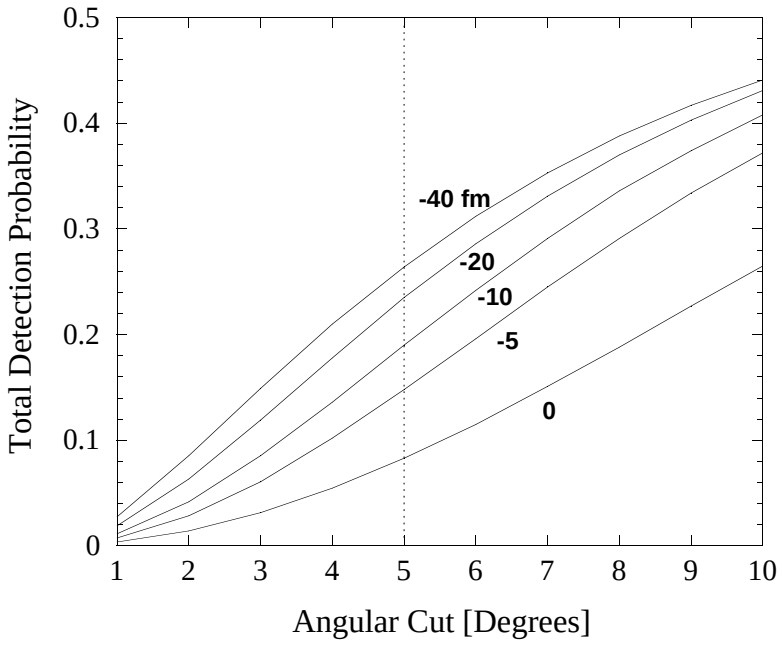

Figure 3.7: Total detection probability of a ^{9}Li+n system breaking up isotropically after being formed from ^{12}Be. Shown here are curves for $a_s = 0, -5, -10, -20, -40$ fm as a function of angular cut for neutron-fragment coincidence events.

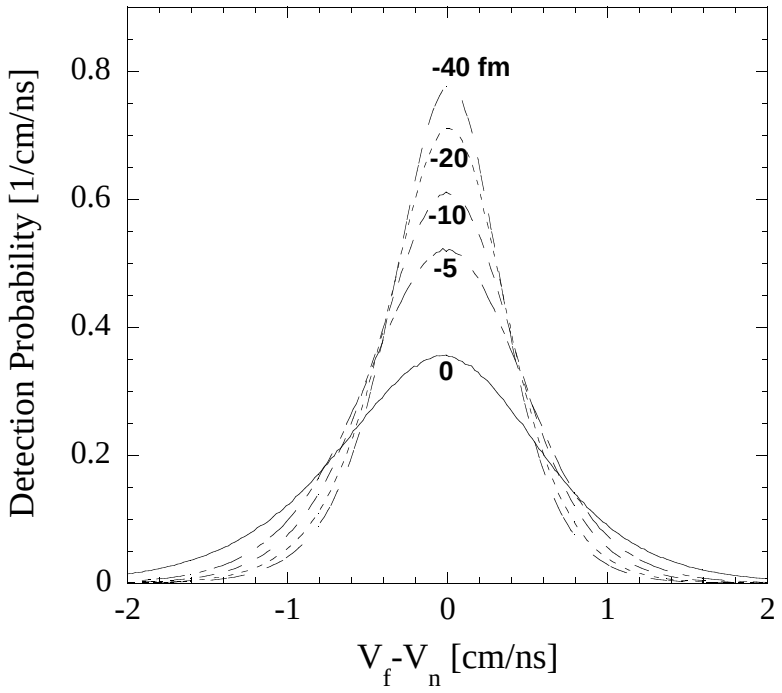

Figure 3.8: Detection probability of a ^{8}He+n system breaking up isotropically after being formed from ^{11}Be. Shown here are calculated velocity distributions for $a_s = 0, -5, -10, -20, -40$ fm for a 10^0 angular cut.

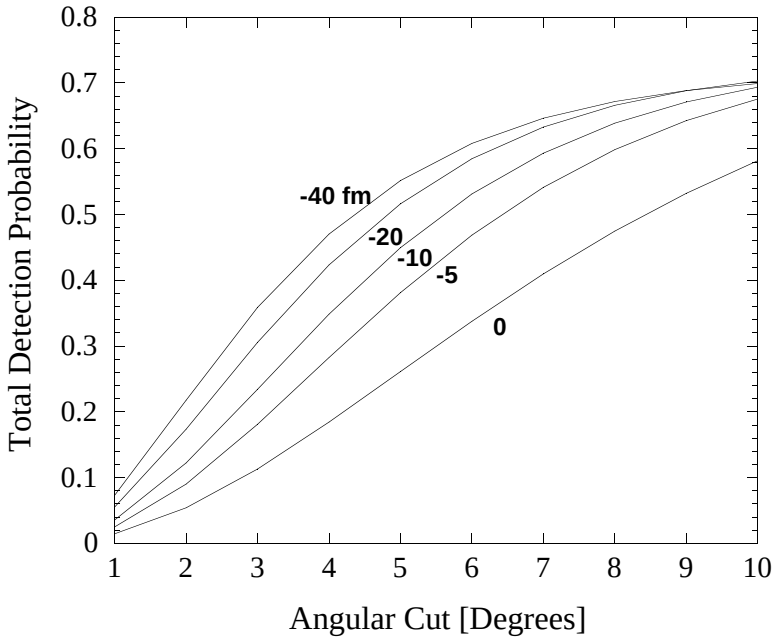

Figure 3.9: Total detection probability of a ^{8}He+n system breaking up isotropically after being formed from ^{11}Be. Shown here are curves for $a_s = 0, -5, -10, -20, -40$ fm as a function of angular cut for neutron-fragment coincidence events.

3.2 Silicon Strip Detectors

The role of the silicon strip detectors in this experiment is to provide an energy-loss ($\triangle E$) signal for particle identification. As a charged fragment passes through the detector, it loses energy proportional to the square of its charge, making it possible to perform particle separation based on the charge of the fragments. The energy calibration was done using a ^{228}Th source. ^{228}Th and its daughter nuclei decay, yielding mono-energetic α-particles with energies listed in Table 3.1. A typical calibration spectrum from the energy calibration is shown in Figure 3.10.

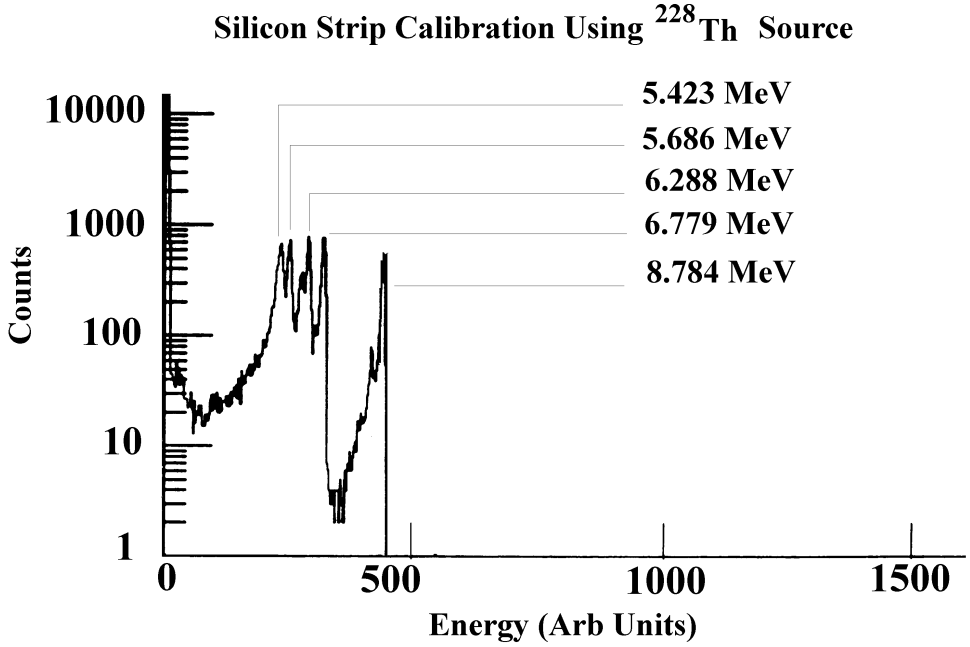

Figure 3.10: Silicon strip Energy calibration spectra with ^{228}Th source.

Table 3.1: Kinetic energy of the α particles for the decay of ^{228}Th.

Isotope	Energy of α (MeV)
^{228}Th	5.423
^{224}Ra	5.656
^{220}Rn	6.288
^{216}Po	6.779
^{212}Po	8.784

3.3 Plastic Scintillators

3.3.1 Energy Calibration

The fragmentation of the primary beam on the production target produces secondary beams of various nuclear isotopes. The so-called 'cocktail beam' is obtained from the widening of the A1200 selection slits, and allows various nuclei with the same momentum to enter the N4 vault and be used to calibrate the plastic scintillators. This is a standard energy calibration procedure. The cocktail beams were set with the following rigidity ($B\rho$) settings: 2.692 Tm, 2.358 Tm, 2.0275 Tm, and 1.4016 Tm. In addition, four targets (200 mg/cm^2 ^{9}Be, 300 mg/cm^2 ^{9}Be, 123 mg/cm^2 ^{27}Al, and 540 mg/cm^2 Al) were used to degrade the cocktail beams to provide more data points for the calibration.

Particle identification of the cocktail beam is performed with beamline time vs. energy loss ($\triangle E$) spectra, and a typical spectrum is shown in Figure 3.11. A two-dimensional gate on the beamline time versus the energy loss is used to select the desired secondary beam. Given the identity of the fragment and the $B\rho$ of the particle, the energy is given by Equation 3.3.

$$E = \sqrt{931.5^2 + \left(299.7925\frac{Z}{A}B\rho\right)^2} - 931.5, \tag{3.3}$$

where E is the energy per nucleon in MeV, and $B\rho$ is magnetic rigidity in Tesla-meter. We have assumed that energy loss through the two PPAC detectors is negligible. The energy-loss through the silicon strip detectors, as well as through the target, needs to be determined for accurate energy calibration for the scintillators. The target energy-loss was calculated with the INTENSITY code, and the energy-loss through the silicon strips is known because it is directly measured. Figure 3.12 shows typical energy calibration spectra.

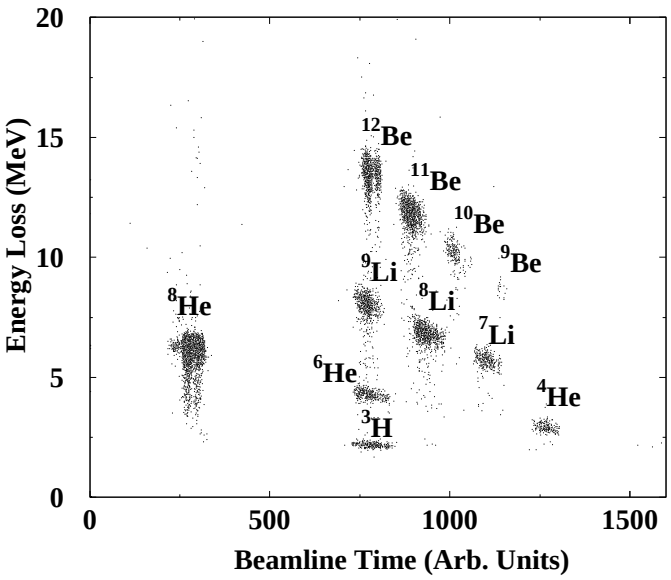

Figure 3.11: Typical $\triangle$E vs. beamline time spectrum from a typical 'cocktail' beam calibration run. The start signal comes from the plastic scintillators and the stop signal comes from the beamline timer, so that a short time-of-flight (TOF) represents slower particles. For a fixed $B\rho$, beams with the same A/Z ratio have the same TOF.

The energy resolution of the plastic scintillator has an energy-dependent response. In addition, the light output from the scintillators is dependent on the charge of the fragment. The energy resolution for helium isotopes for the energy range in this experiment is $3.7 \pm 0.8\%$ as determined by the FWHM of the peak divided by the energy at the peak. For the lithium isotopes, the resolution is $4.7 \pm 0.7\%$, and for beryllium, the resolution is $4.0 \pm 1.0\%$. For the fragments of interest in this experiment, it is reasonable to assume an energy resolution on the order of $4 \pm 1\%$.

As we change the $B\rho$ settings, we also get different kinds of particles into our cocktail beams. The end result is that not all of the fragment detectors would have the same species of isotopes used for calibration. Table 3.2 summarizes the various beryllium, lithium and helium isotopes used in this energy calibration.

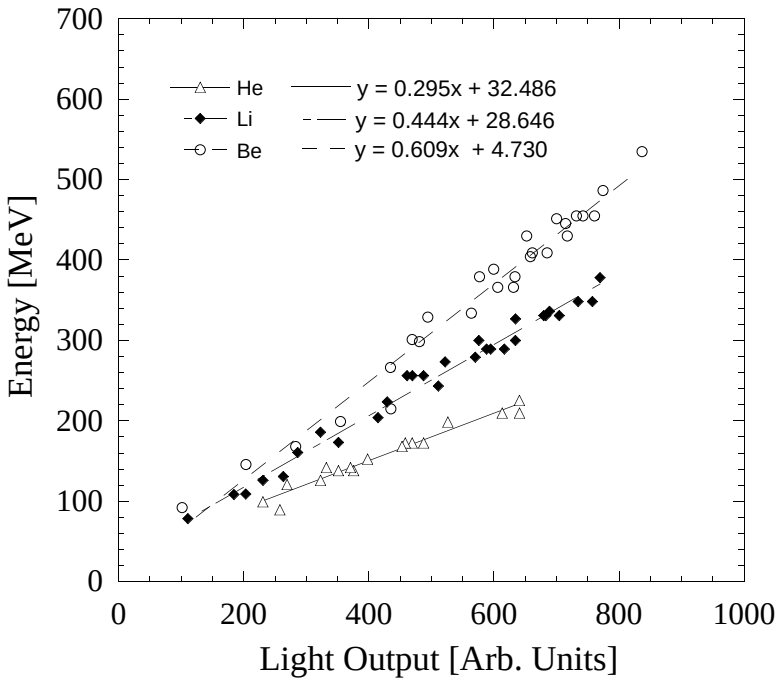

Figure 3.12: A typical energy calibration spectrum for the plastic scintillator. The energy from cocktail beam runs is plotted against the light output from the plastic scintillator. Shown here is the energy calibration for detector 13.

Table 3.2: 'Cocktail' beam calibration summary. Summarized here are the contents in the 'cocktail' beams with different $B\rho$ settings and the detectors which were able to be calibrated. Detector 1 represents the detector with most deflection, and detector 16 is nearest to the beam axis.

$B\rho$ (Tm)	Runs	Contents of 'Cocktail' Beam			Detectors Calibrated
2.692	75-81	^{10,11,12}Be	^{7,8,9}Li,	^{4,6,8}He	12-16
2.358	42-52	^{9,10}Be	^{7,8,9}Li	^{4,6}He	9-16
2.028	55-61	^{9,10}Be	^{7,8,9}Li	^{4,6}He	5-16
1.402	63-74	^{7,9}Be	^{6,7}Li	^{3,4}He	1-16

3.3.2 Fragment Identification

The fragment identification is achieved with a two-dimensional gate on the $\triangle E$ vs. total energy. As mentioned earlier, the $\triangle E$ from the silicon strip is proportional to the Z^2 of the particles, thus providing the charge separation of the particles. The total energy measured by the plastic scintillators provides isotopic separation. Figure 3.13 shows the particle identification of the ^{6,8}He and ^{9}Li.

The plastic scintillator array is placed downstream from the sweeping magnet, and as a result, fragments of the same velocity will strike different scintillators. So, in addition to having the $\triangle E$ vs. E gate, the combination of the plastic scintillator array and the sweeping magnet allows for some spatial separation between the different isotopes. Table 3.3 summarizes the predicted scintillator bar that will be illuminated by a particular nucleus with the specific kinetic energy per nucleon (MeV/u).

3.3.3 Multiple Fragment Hits

There are events in which more than one fragment scintillator detector was illuminated. The cause of such an event is either two fragments striking the plastic scintillators (such as a ^{6}He and ^{4}He) or cross-talk from an adjacent detector (the scintillators are placed adjacent to each other without light shielding). The events which correspond to a single plastic scintillator hit comprise of 90.5% of the events. Table 3.4 summarizes the distribution of plastic scintillators illuminated by the fragments. Only single-hit events from the plastic scintillators are used for the analysis.

3.3.4 Fragment Velocity Measurement

The fragment velocity was calculated by using the measured kinetic energy of the fragment at the time of the reaction. Since the plastic scintillators measure the post-target, post-silicon trip energy, it is necessary to account for the energy-loss in the

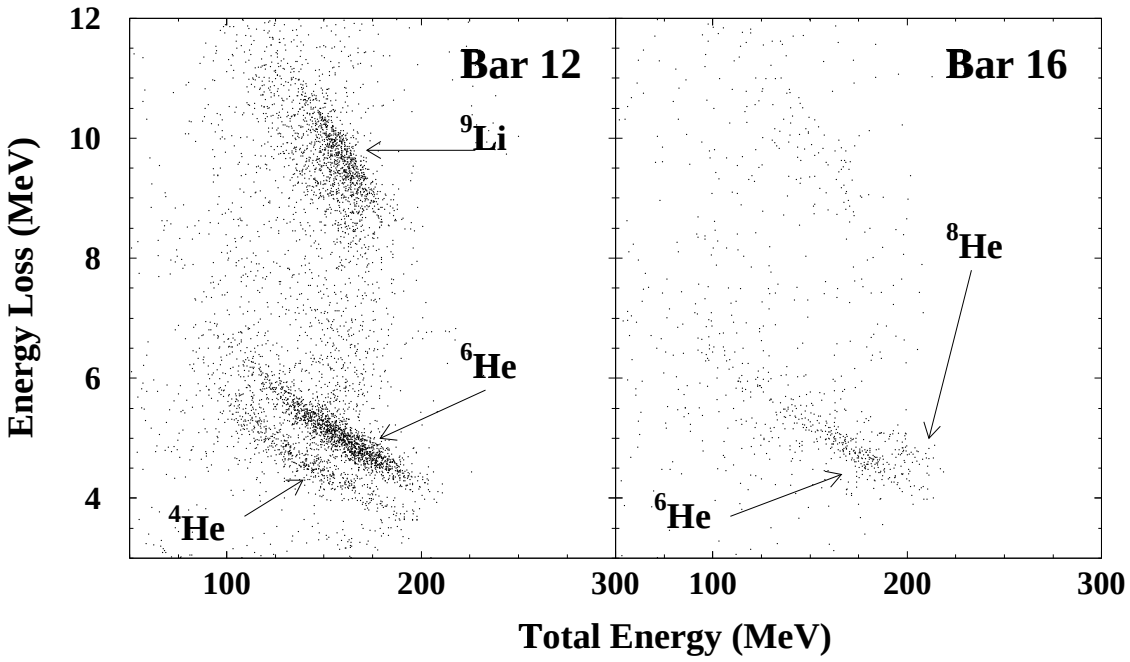

Figure 3.13: Particle identification for two different fragment detectors. The array of sixteen plastic scintillators measures the total energy, and the different positions of the plastic scintillators help with isotope separation. The energy loss was measured by an array of silicon strip detectors positioned downstream from the target. The figure on the left shows an energy-loss vs total energy spectrum of the 12^{th} scintillator bar, which was farther away from the beam axis than the 16^{th} bar. The energy scale used in the two figures is correct for the helium isotopes. Since the light output of the plastic scintillators decreases when the charge of the particle increases, a scale factor of approximately 1.4 is needed to obtain the correct energy for ^{9}Li. While bar 12 detects mostly ^{6}He and ^{9}Li, bar 16 detects only ^{6,8}He, and very little ^{9}Li. Even though ^{9}Li and ^{6}He have the same A/Z ratio, the ^{6}He fragment will have a wider momentum spread than ^{9}Li from the fragmentation reaction, where the spread is characterized by $\sigma = \sigma_0\sqrt{\frac{A_F(A-A_F)}{A-1}}$, where A is the mass for the incident nucleus and A_F is the mass of the reaction fragment. Consequently, there was an appreciable amount of ^{6}He measured, but not ^{9}Li.

Table 3.3: The trajectories of various charged fragments as they pass through the sweeping magnet. The fragments are assumed to be at zero degrees relative to the beam direction, passing through the center of the magnet gap. The calculations are done based on the work by [34], which uses a measured field map of the magnet to integrate the trajectories of the fragment. Detector 1 is the detector farthest from the beam axis, and the detector 16 is the nearest. Values between X and $X+1$ correspond to a fragment predicted to hit bar $X+1$ (such that 13.9 means the portion of bar 14 closer to the beam axis). At energies close to 30 MeV/u, the ^{8}He fragments take a trajectory that strikes the plastic scintillators nearest the beam direction. A higher beam energy would have improved the resolution of the experiment, but the reaction fragments would have been insufficiently deflected by the sweeping magnet.

Energy (MeV/u)	Predicted Plastic Scintillator Position					
	^{11}Be	^{10}Be	^{8}He	^{12}Be ^{6}He	^{4}He	^{6}Be ^{3}He
30.0	11.2	10.1	15.1	12.2	7.2	3.0
29.5	11.1	10.0	15.0	12.1	7.0	2.8
29.0	11.0	9.9	14.9	12.0	6.9	2.7
28.5	10.9	9.8	14.8	11.9	6.8	2.6
28.0	10.8	9.7	14.7	11.8	6.7	2.5
27.5	10.7	9.6	14.7	11.7	6.6	2.3
27.0	10.8	9.4	14.6	11.6	6.5	2.2
26.5	10.5	9.3	14.5	11.5	6.4	2.1
26.0	10.4	9.2	14.4	11.4	6.3	1.9
25.5	10.3	9.1	14.3	11.3	6.1	1.8
25.0	10.2	9.0	14.2	11.2	6.0	1.6
24.5	10.0	8.9	14.1	11.1	5.9	1.5
24.0	9.9	8.7	14.0	11.0	5.7	1.3
23.5	9.8	8.6	13.9	10.8	5.6	1.1
23.0	9.7	8.5	13.8	10.7	5.4	1.0

Table 3.4: Fraction of neutron-fragment coincidence events as a function of number of bars which detected a fragment. For the neutron-fragment coincidence events, 90.5% are detected by one plastic scintillator. Events with multiple scintillator hits are not used for analysis.

Total Bars Fired	Fraction of Events
1	0.905
2	0.093
3+	0.002

target and the silicon-strip detectors. The energy-loss through the silicon is known from the silicon-strip energy calibration. It is assumed that the nuclear reaction occurred at the mid-target position, so the total kinetic energy of each fragment is:

$$E_f = E_{plastic} + E_{silicon} + E_{targeteloss}, \tag{3.4}$$

where E_f is the mid-target energy, and $E_{targeteloss}$ is the energy loss of the fragment as it passes through the target. The velocity is related to the kinetic energy by the relation:

$$v_f = c\sqrt{1 - \left(\frac{1}{1 + \frac{E_f}{mc^2}}\right)^2}, \tag{3.5}$$

where m is the mass of the fragment.

3.3.5 Fragment Velocity Resolution

There are three major factors that contribute to the velocity resolution of the fragment. The discussion of velocity resolution is most conveniently expressed with respect to momentum resolution, and the relationship between momentum resolution σ_p and velocity resolution σ_v can be approximated as:

$$\sigma_v = \frac{\sigma_p}{m\gamma^3}, \tag{3.6}$$

where $\gamma = 1/\sqrt{1-\beta^2}$, and p and m are momentum and the mass of the fragment. This relationship can be obtained by taking the derivative of the equation $p = \gamma m v$, and replacing the differentials dp and dv with σ_p and σ_v. For the energy range of interest here (mid-target energy of around 27.7 MeV/u), $\gamma = 1.030$, so that essentially, $\sigma_v = \sigma_p/m$.

The spread in momentum contributed from the target energy-loss can be obtained from the spread in energy. The relationship between the energy spread and the momentum spread can be approximated as:

$$\sigma_{p_{Eloss}} = \frac{1}{\beta c}\sigma_{Eloss}, \tag{3.7}$$

Table 3.5: Stopping power parameters for beryllium, lithium, and helium nuclei passing through ^{9}Be target. Tabulated here are the parameters C_0 and C_1 for a fit to a form of $S(T) = C_0 T^{C_1}$, where T is the kinetic energy per nucleon of the nucleus. The unit of the stopping power is MeV/(mg/cm^2). Total energy loss can be estimated by multiplying the target thickness (in units of mg/cm^2), with the mid-target energy.

Isotope	C_0	C_1
Beryllium	3.9039	-0.8128
Lithium	2.1997	-0.8131
Helium	0.9804	-0.8139

where $\sigma_{p_{Eloss}}$ is the contribution in momentum (measured in standard deviation σ) from the target energy-loss (σ_{Eloss}). This relation can be derived by simply taking the expression energy E: $E^2 = p^2c^2 + m^2c^4$, which means $EdE = c^2pdp$. Since $p/E = v/c^2 = \beta/c$, one readily obtains the result in Equation 3.7. For a small spread $\sigma_{p_{Eloss}}$ and σ_{Eloss}, one can replace those differentials with these widths.

The stopping power is an energy-dependent quantity, and we obtained our estimates in units of energy per unit target thickness (MeV/(mg/cm^2)) by using a power-law fit in the form of $S(T) = C_0 T^{C_1}$ to the tabulated values from the works of [40]. $S(T)$ is the total energy loss and T is the kinetic energy per nucleon. For the energy range of 20 to 40 MeV/u, the appropriate constants (where the stopping power is expressed in units of MeV/(mg/cm^2)) are summarized in Table 3.5. The energy-loss of the entire fragment can be estimated by multiplying the target thickness (in units of mg/cm^2), with the mid-target energy. As mentioned previously, the mid-target energy is on the order of 27.7 MeV/u for the cases here. There is a 5% error assigned for these predicted energy-loss estimates, as suggested by the authors in [40].

To first order, the energy distribution of the reaction fragments after they pass through the target can be modeled by a rectangular distribution since the reactions can occur near the front or the back of the target with equal probability. A rectan-

gular distribution of width w has a standard deviation of $w/\sqrt{12}$. Thus, as a rough approximation, the width of this energy distribution σ_{Eloss} can be taken as:

$$\sigma_{Eloss} = A_f \frac{E_f - E_b}{\sqrt{12}}, \tag{3.8}$$

where E_f is the energy per nucleon of the reaction fragment after it traveled through the entire target with its initial energy taken to be the beam energy, E_b is the energy per nucleon of the beam after it has traveled through the target, and A_f is the mass of the reaction fragment.

As mentioned in Section 3.3.1, the energy resolution of the plastic scintillators is taken as 4% from the result of the cocktail beam calibration. Given the energy resolution of the plastic scintillators expressed as σ_{Eres}, the contributed momentum width $\sigma_{p_{Eres}}$ can be approximated as:

$$\sigma_{p_{Eres}} = \frac{E\sigma_{Eres}}{c\sqrt{E^2 - m^2c^4}}, \tag{3.9}$$

where E is the total energy, and m is the mass of the fragment.

The momentum slits of the A1200 are set at 3% for ^{12}Be and 1% for ^{11}Be. Assuming a rectangular distribution, the momentum spread from the beam σ_{beam} can be approximated as

$$\sigma_{p_{beam}} = \frac{\triangle P}{\sqrt{12}}, \tag{3.10}$$

where $\triangle P$ is the momentum acceptance of the beam.

These resolution effects can be added in quadrature so that $\sigma_p^2 = \sigma_{p_{Eloss}}^2 + \sigma_{p_{Eres}}^2 + \sigma_{p_{beam}}^2$. Tables 3.6 and 3.7 summarize the resolution effects from each of these three contributions. The velocity resolutions expressed in both units of momentum as well as velocity. In the case of an incident ^{12}Be projectile, the effects of each of these contributions on the overall velocity resolution are very comparable. Although the ^{11}Be beam has a smaller momentum spread than ^{12}Be (1% momentum acceptance versus 3%), there is an increased spread in the target energy-loss, since ^{11}Be loses

Table 3.6: Resolution of momentum and velocity measurement of the plastic scintillators with incident ^{12}Be beam. Listed here are the contributions from target energy-loss, momentum spread in the ^{12}Be beam, and energy resolution from the plastic scintillators.

	Total		Target		Beam (^{12}Be)		Energy Res.	
Fragment	MeV/c	cm/ns	MeV/c	cm/ns	MeV/c	cm/ns	MeV/c	cm/ns
^{8}He	34.5	0.13	26.2	0.10	15.9	0.06	15.9	0.06
^{6}He	23.0	0.11	15.7	0.08	11.9	0.06	11.9	0.06
^{9}Li	27.9	0.09	11.8	0.04	17.9	0.06	17.9	0.06

Table 3.7: Resolution of momentum and velocity measurement of the plastic scintillators with incident ^{11}Be beam. Listed here are the contributions from target energy-loss, momentum spread in the ^{11}Be beam, and energy resolution from the plastic scintillators.

	Total		Target		Beam (^{11}Be)		Energy Res.	
Fragment	MeV/c	cm/ns	MeV/c	cm/ns	MeV/c	cm/ns	MeV/c	cm/ns
^{8}He	34.6	0.13	30.3	0.11	5.3	0.02	15.8	0.06
^{6}He	22.5	0.11	18.8	0.09	4.0	0.02	11.9	0.06
^{9}Li	24.8	0.08	16.2	0.05	5.9	0.02	17.8	0.06

more energy going through the target. Thus, the overall resolution of the ^{12,11}Be beams is about the same.

All of these resolution effects are included in the computer simulation used for data analysis. The contribution from the resolution from the silicon strip detectors (nominally 1-2 % is typical for such detectors) is very minimal and will essentially have no effect on the resolution, since the typical energy loss through the silicon strip detectors is on the order of 10 MeV or less for ^{9}Li and ^{6,8}He.

3.4 NSCL Neutron Walls

The NSCL neutron wall array is a large-area position-sensitive detector. Each of the two walls has dimensions of 2 meters by 2 meters, and has a neutron detection

efficiency on the order of 12 % for 30 MeV neutrons [35]. More detailed discussions on this detector can be found elsewhere [35].

3.4.1 Neutron Identification

Crucial in this experiment is the ability of this detector to distinguish the difference between a neutron signal versus a γ- ray signal. This is achieved with the method of pulse-shape discrimination. The light-output as a function of time is not the same for for a neutron and a γ-ray. More specifically, a greater portion of a γ- ray pulse comes from the beginning part (fast) of a pulse as compared with a neutron signal. If both the fast portion of the signal and the total size of the signal are measured, then it is possible to separate the neutron and γ-ray events. A pulse-shape discrimination circuit discussed by [35] is used in this experiment. This circuit takes the anode signal from the neutron wall PMT as an input, and outputs four signals for the QDCs: (1) signal proportional to the size of the head of the signal (QFAST), (2) signal proportional to the total charge of the anode pulse (QTOTAL), (3) attenuated QFAST signal, (4) attenuated QTOTAL signal. Attenuated signals are necessary because the neutron wall signals have a large dynamic range. The threshold on the neutron wall detector was set to 1 MeVee (MeV electron-equivalent); the same amount of light output that comes from a one MeV electron. A typical spectrum of the neutron wall identification is shown in Figure 3.14

3.4.2 Multiple Neutron Hits

As in the case of the plastic scintillators, multiple-hit events can also occur for the neutron detectors. A sophisticated approached used in reference [50] to process multiple-hit events is not needed for the present work since the events studied here are the single neutron-coincidence events. While a single neutron can produce neutron pulses

Table 3.8: Fraction of neutron coincidence events as a function of number of bars which detected a fragment. For the neutron-fragment coincidence events, over 90% are detected by only one neutron wall cell.

Total Neutron Cells Fired	Fraction of Events
1	0.923
2	0.067
3+	0.003

in multiple neutron wall cells, approximately 92.3% of the fragment-neutron coincide events includes only 1 neutron wall cell. Table 3.8 summarizes the distribution of the multiple neutron events.

3.4.3 Position Calibration and Resolution

Positions on the neutron walls are determined by taking the time difference between the left and the right detector, and bear the following relationship:

$$X = C_1(T_L - T_R) + C_2, \tag{3.11}$$

where X is the x-position on a neutron wall detector, and the T_L and T_R are the values of the fragment-detector started, neutron-wall stopped times. C_1 and C_2 are calibration constants that need to be determined on a detector-by-detector basis. Since background γ-rays evenly bombard the entire width of a neutron detector, the position calibration is simply a matter of analyzing the γ-ray-gated time difference spectra. Each of the neutron wall cells is 2 meters wide, so the proportionality constant $C_1 = 2.0$ meters$/\triangle T$, where $\triangle T$ is the width of the γ-gated time difference spectra. C_2 is an offset constant chosen such that the center of the neutron wall has the position of zero meters. The y-position is obtained by the knowledge of which neutron wall cell observed the neutron event.

One important question regarding the neutron wall is the position resolution of

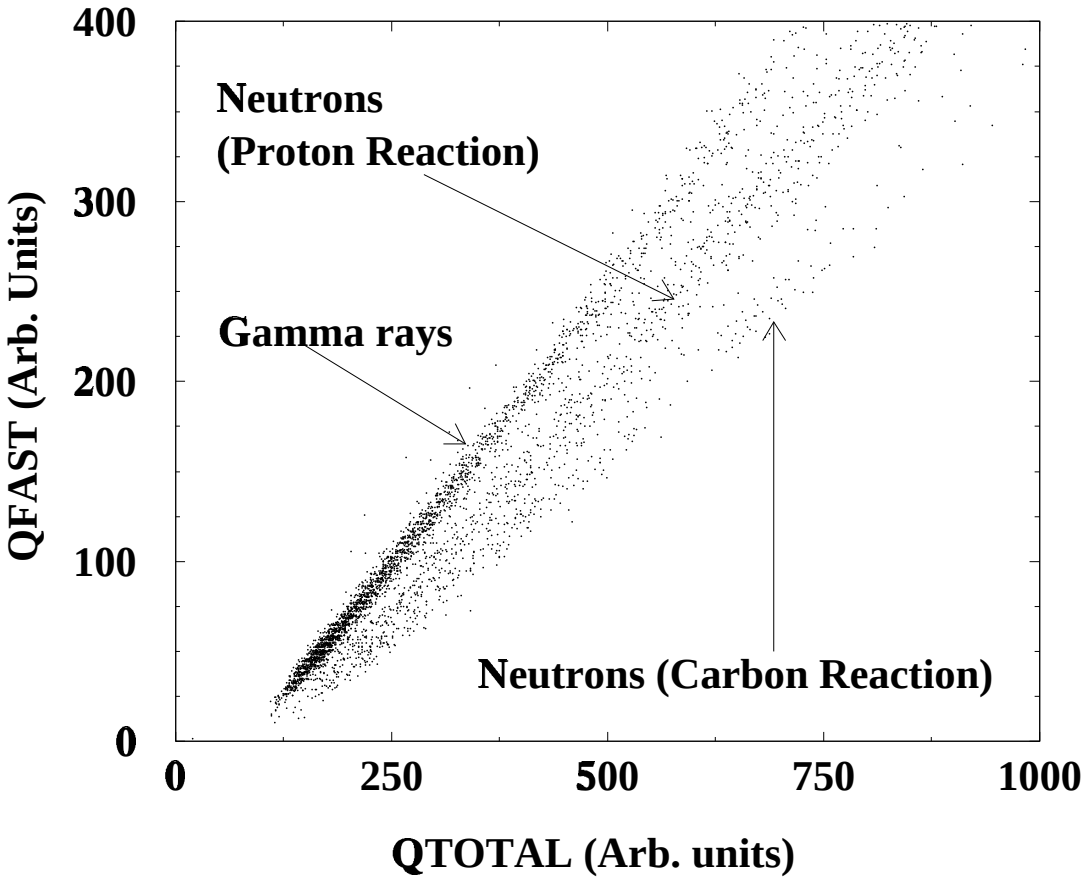

Figure 3.14: Neutron identification in this experiment was achieved through pulse-shape discrimination. Shown here is the fast (QFAST) portion of the neutron wall signal plotted versus the total pulse size (QTOTAL). There are three distinct bands in the spectra. The top band represents γ-rays, while there are two bands corresponding to neutron events. One of these bands comes from the reaction with the proton in the liquid scintillator, and the other comes from interactions with the carbon.

the detector. This is determined by using the so-called 'shadowbars' during the experiment.

During the run, brass bars (the aforementioned shadowbars) with the dimension of 3"x $2\frac{1}{2}$" x 12" (7.6cm x 7.0 cm x 30.5 cm) are placed 173 cm away from the target position. The front neutron wall is 500 cm away from the target, while the back neutron wall is 550 cm away. From simple geometric considerations, we see that the 'shadow' casted by these shadowbars will have the size about 22 cm x 20 cm. With each neutron wall being 7.62 cm tall, each shadowbar should have effects that can be observed across at least two adjacent neutron detectors, with one cell completely shadowed. These effects were observed.

In order to extract the background neutrons as well as the position resolution, the following approach was taken. The neutron distribution across a neutron wall cell in the absence of a shadowbar is known. Typically, the distribution resembles Figure 3.15. If the resolution of the neutron wall is perfect, we know that in the presence of a shadowbar, the distribution of the neutrons would resemble Figure 3.16.

In this ideal case, a sharp dip would be present in the distribution, where the height of this sharp dip would represent the background neutrons detected. In this case, there would be a sharp drop-off in the neutron distribution in the region where the shadowbar shields the neutron wall. Ideally, there would be no neutrons in the region of the cell shielded by the shadowbar. However, there can be some counts in this region that came from some other sources, such as neutron scattering from an adjacent cell. To account for this, an additional fitting parameter H is introduced. H corresponds to the neutrons not coming directly from the beam reaction with the target, and thus is a measure of the background.

If the resolution of the detector is characterized as:

$$f(x) = \frac{1}{\sqrt{2\pi}\sigma} \exp[(x - x_0)/2\sigma^2], \tag{3.12}$$

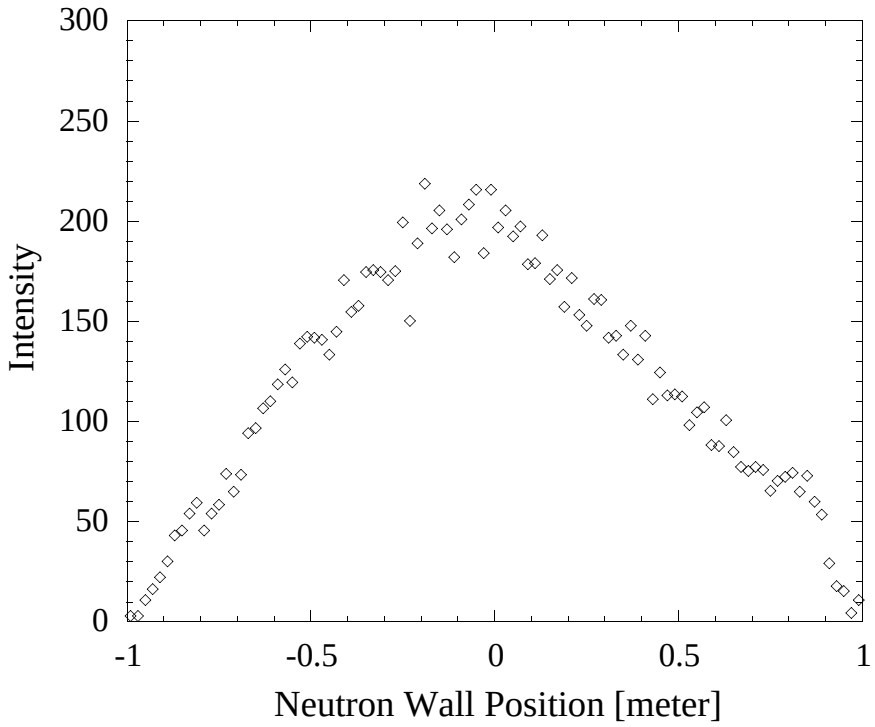

Figure 3.15: Neutron distribution on cell 9 without shadowbar

and the ideal response of a given neutron wall cell can be taken as the neutron distribution in the absence of the shadowbar, and the shadowed region has a response of H (as in Figure 3.16) , one can perform a two-parameter fit with the shadowbar data by varying both H and σ. This analysis is performed for cells 9 and 13.

Figures 3.17 and 3.18 show the shadowbar data of cell 9 (middle of the front neutron wall) and cell 13 (near the top of the front neutron wall).

According to both of these fits, a FWHM of 12 cm for the Gaussian response function for the neutron wall seems to fit the shapes of the shadow bar curves quite well. Cell 9 is the neutron wall cell that is closest to the beam direction. A detector resolution of 12 cm and a background parameter H=6 seem to fit quite well. We expect around 113 events in the region covered by the shadowbar, so the fit suggests that around 5% of the events in cell 9 are background events. A similar analysis performed on Cell 13 (H=10, expected count=109) suggests that we have about a 9% background for that particular cell.

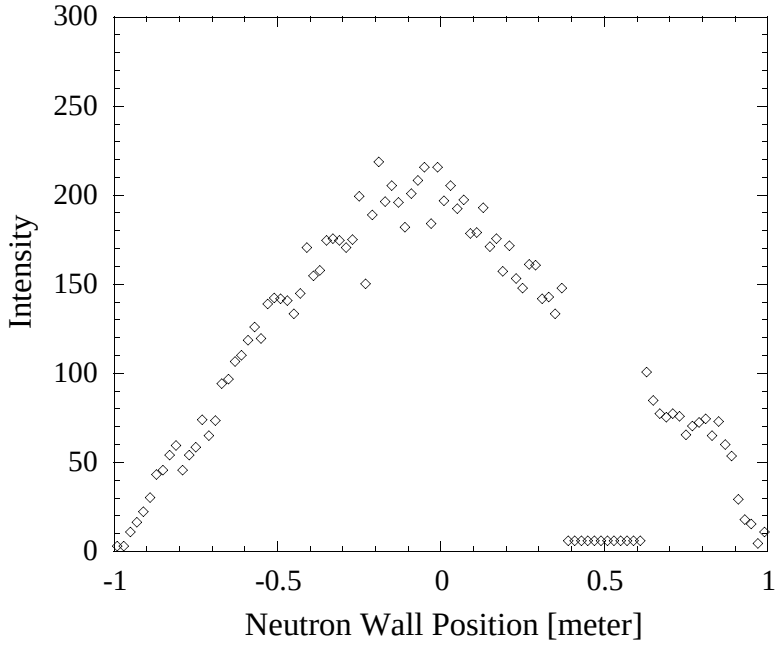

Figure 3.16: Hypothetical neutron distribution on cell 9 in presence of shadowbar, where perfect resolution is assumed.

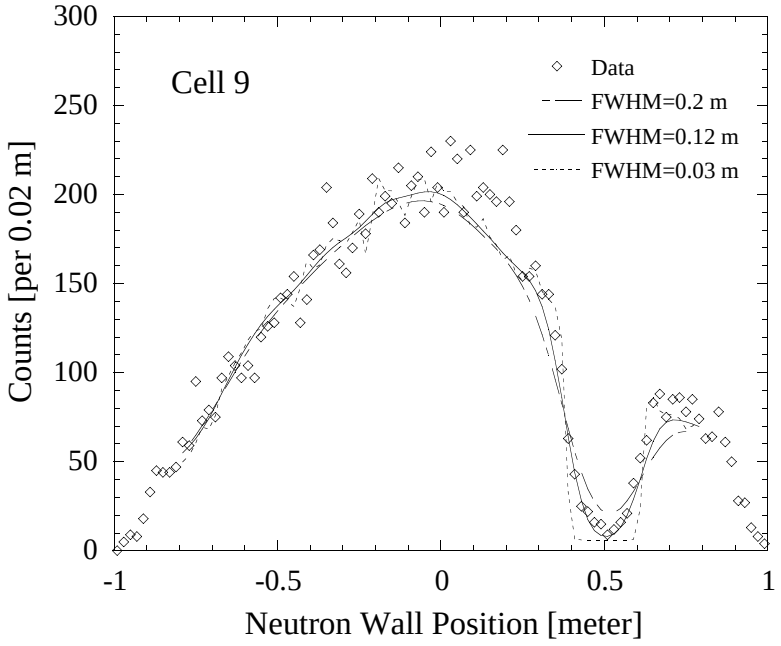

Figure 3.17: Neutron Wall cell 9 shadowbar spectra. Shown are the fits using FWHM=0.2, 0.12, and 0.03 meters, with background parameter $H = 6$. The best-fit uses FWHM=0.12 m (σ = 5.1 m) for neutron response function, and the $H = 6$ corresponds to a 5 % contribution to background.

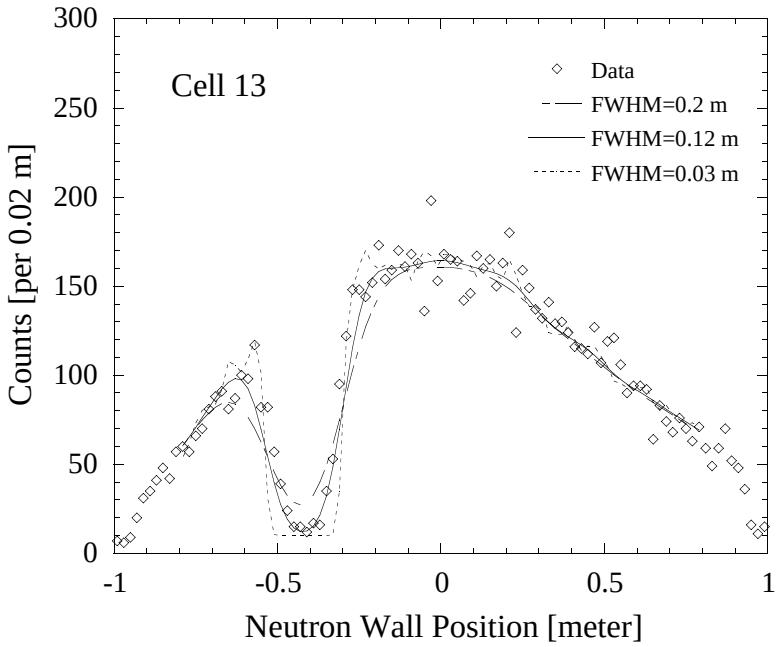

Figure 3.18: Neutron Wall cell 13 shadowbar spectra. Shown are the fits using FWHM=0.2, 0.12, and 0.03 meters, with background parameter $H = 6$. The best-fit of uses FWHM=0.12 m (σ = 5.1 m) for neutron response function, and H = 10 corresponds to a 9 % contribution to background.

In the works by [35] it was concluded that the position sensitivity of the neutron wall approaches 7.65 cm (FWHM) for high-energy neutron events. This value was extracted through the use of a collimated source at different positions of the neutron wall. The analysis performed on these shadowbars suggests a substantially worse resolution (FWHM of 12 cm versus 7.65 cm).

Because the size of the neutron wall cell is only 7.62 cm, it suggests a better position resolution is obtained vertically as compared to horizontally. A rectangular distribution with a width of 7.62 cm is equivalent to a Gaussian distribution with σ = 2.2 cm (Gaussian equivalent to FWHM=5.2 cm). This is less than 50% of the FWHM=12 cm in the horizontal direction. In terms of standard deviation σ, the position resolution is on the order of $\sigma_x = 5.1 \pm 1.0$ cm.

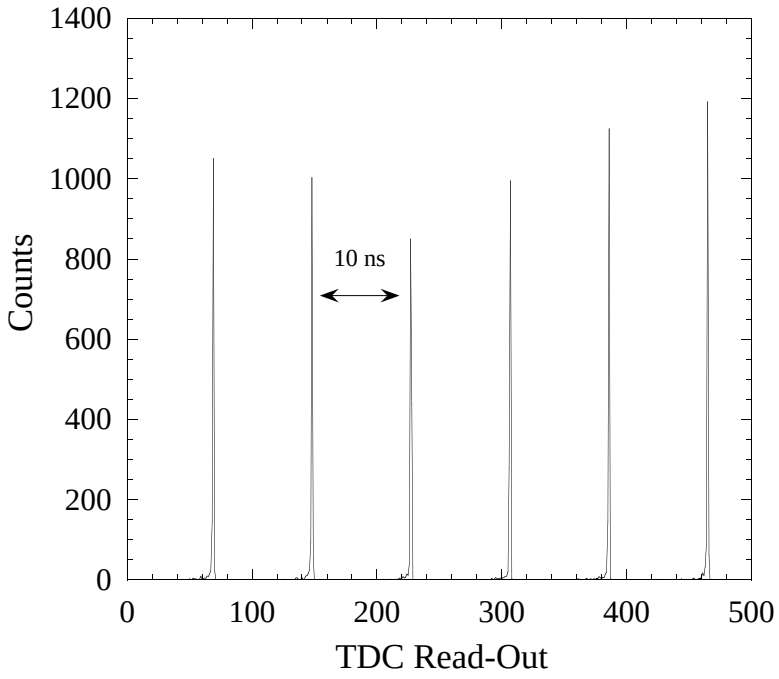

Figure 3.19: TDC calibration spectrum

3.4.4 Time Calibration and Resolution

The time-to-digital converters (TDC) in the experiment are all calibrated with a pulser that generates random pulses at adjustable intervals. A typical interval is 10 ns. By pulsing the TDCs with this pulser, we easily calibrate our TDCs. A typical spectrum from this calibration is shown in Figure 3.19.

The time-of-flight of the neutron is measured with a start trigger that comes from any one of the plastic scintillators and the stop trigger that comes from the neutron wall. Thus, it is possible to have sixteen possible start triggers and thirty-two possible stop triggers. With issues such as different cable lengths and delays, it is necessary to have a common reference for the time-of-flight (TOF) measurements. A ^{60}Co source was placed between the neutron walls and the plastic scintillators, thus providing an absolute timing reference for TOF measurement. Figure 3.20 shows a typical spectrum from this calibration. The time resolution as measured with standard deviation σ is 2.1 ns.

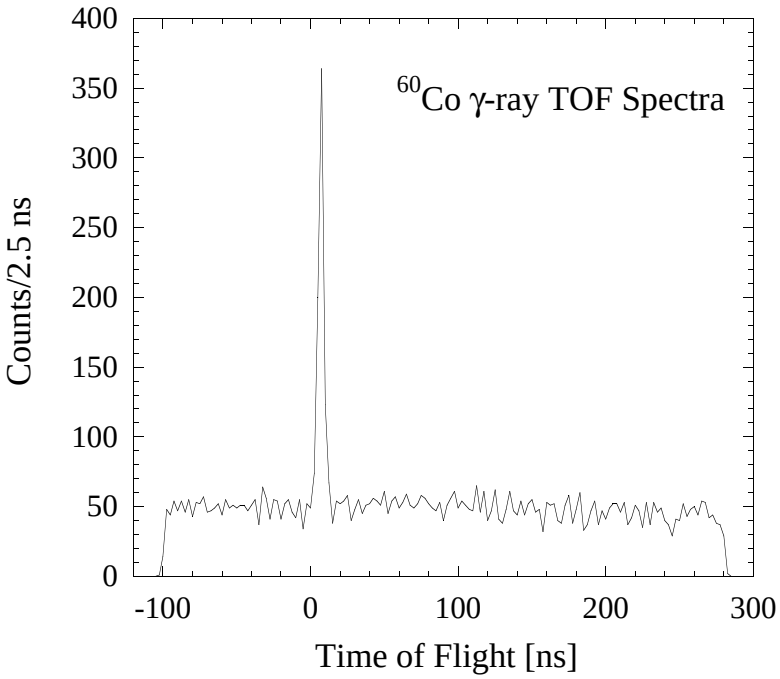

Figure 3.20: ^{60}Co γ-ray TOF spectrum. The peak shown has a FWHM of 5 ns.

3.4.5 Neutron Velocity Measurement

The neutron time-of-flight is measured with respect to the fragment detectors. Thus, in order to obtain the total neutron time-of-flight from the target, it is necessary to obtain the velocity of the fragment measured in coincidence. This can be done by the procedure outlined in Section 3.3.4.

The velocity of the neutron is then given as

$$v_n = \frac{D_n}{\frac{D_f}{v_f} + T_{fn}}, \tag{3.13}$$

where D_n is the distance traveled by the neutron, D_f is the distance traveled by the fragment from the target to the scintillator, which is approximately 170 cm for all detectors, v_f is the velocity of the fragment (Section 3.3.4), T_{fn} is the neutron time-of-flight measured with respect to the fragment detector. The T_{fn} is measured by taking the average time between the left and the right neutron wall TDC signals.

Table 3.9: Resolution of momentum and velocity measurement of neutron wall detectors with an incident ^{12}Be beam. Shown are the contributions from resolution from the fragment velocity resolution, time resolution, and position resolution effects.

	Total		Frag. Velocity		Time Res.		Position Res.	
Fragment	MeV/c	cm/ns	MeV/c	cm/ns	MeV/c	cm/ns	MeV/c	cm/ns
^{8}He	8.2	0.24	1.5	0.04	7.4	0.22	3.0	0.09
^{6}He	8.1	0.24	1.3	0.04	7.4	0.22	3.0	0.09
^{9}Li	8.1	0.24	1.1	0.03	7.4	0.22	3.0	0.09

3.4.6 Neutron Velocity Resolution

Because the fragment velocity is used to extract the neutron velocity, all of the resolution issues discussed in Section 3.3.5 apply to the neutron velocity resolution. Since the fragment velocity resolution is fragment dependent, the neutron velocity resolution is also fragment dependent. In addition, there is the contribution from the resolution of the neutron time-of-flight measurement. Shown in Tables 3.9 and 3.10 are the neutron velocity resolutions expressed in both units of momentum and velocity for initial ^{12}Be and ^{11}Be projectiles. The tables show the contribution to the resolution from the fragment velocity resolution, time resolution, and position resolution effects. The dominant effect in the neutron velocity resolution is the time resolution of the time-of-flight measurement, and the fragment velocity resolution is the smallest contribution. The neutron velocity resolution is quite a bit worse than the fragment velocity resolution; the resolution as measured in standard deviation σ is approximately a factor of two larger than the fragment velocity resolution. Thus, the neutron velocity resolution dominates the resolution of the relative velocity distribution.

Table 3.10: Resolution of momentum and velocity measurement of neutron wall detectors with an incident ^{11}Be beam. Shown are the contributions from resolution from the fragment velocity resolution, time resolution, and position resolution effects.

	Total		Frag. Velocity		Time Res.		Position Res.	
Fragment	MeV/c	cm/ns	MeV/c	cm/ns	MeV/c	cm/ns	MeV/c	cm/ns
^{8}He	8.1	0.24	1.5	0.04	7.4	0.22	3.0	0.09
^{6}He	8.1	0.24	1.3	0.04	7.4	0.22	3.0	0.09
^{9}Li	8.0	0.24	0.9	0.03	7.4	0.22	3.0	0.09

3.5 Particle Tracking Issues

The ability to track the reaction products as well as the neutrons is essential for the selection of collinear events. The experiment was set up with two parallel plate avalanche counter (PPAC) detectors in front of the target and as aforementioned, silicon strip detectors after the target. For inexplicable reasons, the position information from the PPAC detectors did not agree with tracking from the silicon strip detectors. The same problem was found in the two other experiments that ran with the identical setup. The silicon strip detector signals are considered most reliable because they provided correct particle identification signals (as we will see later in our data analysis). As such, PPAC signals were discarded from the analysis.

Without the use of pre-target tracking, it was necessary to make certain assumptions about the characteristics about the incident secondary beam. In this work, the beam is assumed to have taken a straight path to the target.

Originally, as in other experiments done with this setup such as those in Jon Kruse and Jing Wang's thesis [34, 50], the silicon strip detectors were to provide the post-target tracking. Because the silicon detectors contain some dead strips, there are events where either the x or the y coordinate of the event are missing. Although silicon strip detectors could not be used for tracking, it was possible to obtain the information from the plastic scintillator bars.

The plastic scintillators are placed approximately 170 centimeters away from the target and downstream from the bending magnet. At a width of 4 cm, the scintillator bar has an angular coverage of 1.35 degrees, which makes it just slightly larger than the angle subtended by the silicon strips. The x-position information is contained within which detector was struck by the charged fragment. For each of the ^{6,8}He and ^{9}Li, we assume the scintillator bar that has the largest number of counts of the given isotope represents the $x = 0$ position. For ^{6}He and ^{9}Li, bar 13 represents $x = 0$, and for ^{8}He, it is bar 15.

Because the time signals of the PMTs on the plastic scintillators relative to the silicon-strip detector were also recorded, the time difference between the top and the bottom PMT on each scintillator can provide y-position information. This is completely analogous to the procedure for determining the x-position on each of neutron wall cells.

In addition to the benefit of an increased number of available events for analysis, the use of the plastic scintillator for tracking is very important from another standpoint. The width of the beam spot for the experiment (as measured by FWHM), is on order of 2.5 cm, which covers eight silicon-strip detectors. Since the beam-spot is large compared to the distance of the silicon strip detector behind the target, it means that there will not be much correlation between which strip is hit versus the angle it is deflected from the beam axis. By tracking with the plastic scintillators, the additional flight path improved the ability to track.

In conclusion, the final manner by which the particles were tracked turned out to be superior than the method originally planned, since this allows the analysis of events that would have been difficult to analyze without complete kinematic information.

3.6 The Fitting of the Velocity Difference Data

Each set of velocity difference data is fitted to a combination of a computer simulated velocity difference distribution and a background. It was found that a background component is necessary to describe the data. In the previous experiments by Kryger *et al.* and Thoennessen *et al.* [27, 28], a background of a thermal neutron source of the form $\sqrt{E}\exp(-E/T)$ was used. After accounting for the detector efficiencies and acceptances, the relative velocity distribution of the background takes a near-Gaussian shape. In the present work, an event-mixed background is used instead of the thermal neutron background assumed by [27, 28].

The essential idea behind event-mixing is to combine data from two different physical events and treat them as a single event. The combination of two different events simulates a data set of which one does not expect to have any physical correlation, and it can be used to model the background in the experiment. For the neutron-fragment coincidence data collected in this experiment, the event-mixed analysis would use the fragment data from one event and the neutron data from another event. The analysis uses the same event selection procedures, and the distribution is one where there were no correlations between the fragment and the neutron. As will be shown here, the event-mixed velocity difference distribution can be obtained by folding the velocity difference distributions of the neutron and the fragment.

Let's assume that there are two distributions, $w_n(v_n)$ and $w_f(v_f)$, which are velocity distribution functions of the neutrons and the fragments normalized to unity. The velocity difference is then defined as:

$$\triangle v = v_f - v_n \tag{3.14}$$

If the two distributions are independent, then the probability of obtaining some v_f and v_n is simply:

$$d^2w(v_f, v_n) = w_n(v_n)w_f(v_f)dv_n dv_f \tag{3.15}$$

This means that the probability distribution of a velocity difference can simply be written as:

$$dw^2(\triangle v, v_n) = w_n(v_n) w_f(\triangle v + v_n) J(\frac{v_n v_f}{v_n \triangle v}) dv_n d\triangle v \tag{3.16}$$

Since the Jacobian $J(\frac{v_n v_f}{v_n \triangle v}) = 1$, the differential probability can simply be expressed as:

$$\frac{dw(\triangle v)}{d\triangle v} = \int w_n(v_n) w_f(v_n + \triangle v) dv_n \tag{3.17}$$

Once both the neutron and the fragment velocity distributions are known, a simple folding of the two distributions will give a distribution that corresponds to uncorrelated fragments and neutrons. Typically, the FWHM of the neutron and the fragment velocity distributions are on the order of 1 cm/ns. The velocity distributions for the neutrons and the fragments are tabulated in Appendix A.

In our velocity difference analysis, there will be a significant fraction of the events where the measured neutrons and the fragments are not correlated. This may be caused by neutron interaction with the target or other final-state interaction with the reaction fragments. For example, the case of a ^{9}Be(^{12}Be,^{6}He+n)X reaction, where, in addition to a ^{6}He fragment being produced, there are four other neutrons available in the system. Consequently, the detected neutron might have never interacted with the ^{6}He. In addition, it is also possible that ^{12}Be can break up into ^{6}He + ^{4}He + 2n. Furthermore, it is possible that an observed neutron may have interacted with the target instead of the fragment of interest. With the estimate of a background distribution, we then can proceed to simulate the events associated with various p-wave and s-wave scattering which allows for comparison with experimental data. The velocity difference distribution from the final-state interaction is simulated with a computer simulation which accounts for the detector resolution and acceptance effects in addition to energy-loss straggling through the target and silicon-strip detectors. In the computer simulation, it is assumed that the unbound system is populated by

the fragmentation in the target and then experiences an isotropic decay. The energy distribution of this decay is calculated with the potential scattering model, which will be discussed in detail in Chapter 4. Because the energy calibrations are not perfect, it is possible to have a systematic shift in the spectra, and the absolute position of the theoretical curve is allowed to be shifted arbitrarily to fit the data. In general, such a shift is small, on the order of 0.1 cm/ns or less. The best fit was obtained by changing the relative contributions amongst the background and the predicted distributions from final state interactions using the minimum χ^2 method.

Chapter 4

Model of the Reaction of the Final-State Interaction

This section discusses the simple model for the formation of the unbound nuclei in the final states as well as the manner which the final-state interaction is calculated.

4.1 Fragmentation Mechanism for Breakup

For a system where the reaction fragments are produced as a result of a fragmentation reaction of a stable projectile, the momentum distribution can be described as a Gaussian with width σ

$$\sigma = \sigma_0 \sqrt{\frac{K(A-K)}{A-1}}, \tag{4.1}$$

where A = mass of the original (unreacted) nucleus, K = mass of the emerging fragment, and a typical value for σ_0 is 90 MeV/c [37] for high-energy reactions.

Equation 4.1 can be derived with a model using two assumptions: (1) The projectile breakup is a fast process (thus the sudden approximation is valid), and (2) The emerging fragments from the breakup have the nucleon momenta from the initial projectile. These assumptions were first put forth by Feshbach and Huang [38] but it

was shown by Goldhaber [37] that these results can be derived by using a statistical model where the nucleons in the initial projectile have minimal correlation with each other. In addition, it was also shown that the σ_0 parameter can be related to the Fermi momentum via the relation $\sigma_0 = p_f/\sqrt{5}$.

The measurement of the σ_0 parameter from this experiment will show that the present data is consistent with this Goldhaber picture. The σ_0 parameter, which characterizes the momentum transfer from a fragmentation reaction, is extracted here by measuring the width σ of the fragment momentum distribution and then using Equation 4.1. However, the distribution would be broadened by the target energy-loss, momentum spread from the incident beam, as well as energy-resolution of the detectors. Since the momentum resolution of the fragment momentum measurement has already been discussed (Section 3.3.5), it is a straight-forward task to extract the value for σ_0.

The extracted value of σ_0 for various fragments for ^{11,12}Be as well the momentum resolution are listed in Tables 4.1 and 4.2. The momentum distributions of the fragments are shown in Figures 4.1, 4.2, and 4.3. The σ of the fragment momentum distribution and its error were assigned by taking the average and the standard deviation of four different methods of measurement. The four methods are: (1) Gaussian fit of distribution and extract σ, (2) Assuming the distribution to be a triangular distribution and extract σ, (3) Actual computation of the standard deviation of the data over the entire distribution, and (4) measuring the FWHM of the distribution and assume a Gaussian distribution when extracting a σ (dividing by 2.35).

The values of extracted σ_0 are smaller than the canonical value of 90 MeV/c. However, it has been experimentally observed that σ_0 diminishes with decreasing beam energy [39]. Figure 4.4 shows the data with various reactions at different beam energies. Murphy and Stokstad [39] observed momentum widths σ_0 of 65 and 60

MeV/c for ^{6,7}Li respectively from a ^{9}Be + Au reaction at 27.4 MeV/u. The results from [39] are obtained from using a beam energy very comparable to those used in this experiment. The measured σ_0 in this experiment are consistent with these results, with the exception that the ^{8}He momentum distribution with incident ^{12}Be seems somewhat narrower.

In the case of the momentum distribution of the ^{9}Li fragments from the breakup of ^{11}Be, there exist theoretical techniques to predict the distribution. In particular, one can use the model of a knock-out reaction, where one proton in the ^{11}Be is knocked out and the momentum distribution of the ^{10}Li is deduced. In the rest frame of the projectile and if sudden approximation is valid, the momentum of the remaining fragment equals that of the knocked-out nucleon. Consequently, the momentum of the fragment can be determined by simply integrating the neutron momentum probability over the impact parameter. The integration was done using a black disk approximation. A detailed discussion on this technique can be found in [41]. The calculation performed in this analysis is similar to those used in [8, 9]. Although the deduced momentum distribution in this case is the for the ^{10}Li, the momentum distribution of the ^{9}Li can be taken as 9/10 of the ^{10}Li distribution. Figure 4.3 shows the calculated distribution for a single neutron-knockout reaction transformed to the laboratory system. The resolution correction has not been included; it would broaden the peak by approximately 4 MeV/c.

The excellent agreement between the experiment and theory on the ^{9}Li momentum distribution data suggests that the sudden approximation is valid, and that reaction products are projectile-like fragments. In addition, the extracted σ_0 value indicates that the momentum transfer from the reaction will be small and it would allow us to assume that the reaction fragments have the same momentum distribution as they had within the beam projectile. The fact that the recoil effects can be neglected here

Table 4.1: Goldhaber σ_0 parameters extracted from incident ^{11}Be projectile. All values tabulated are in units of MeV/c and are expressed in terms of standard deviation σ. Shown tabulated here are the extracted σ_0, the estimated contribution from the momentum resolution, and the measured momentum spread of the fragment. Since the halo neutron in ^{11}Be is so loosely bound, it means that it would not contribute much Fermi momentum to the system. Consequently it might be more correct to use $A = 10$ for the incident ^{11}Be. The extracted σ_0 parameter from the use of both of these assumptions are shown.

Fragment	$\sigma_0(A = 11)$	$\sigma_0(A = 10)$	Resolution	σ_{exp}
^{8}He	43.1±1.4	50.0±1.6	34.6	75.1±1.7
^{6}He	64.5±2.8	68.4±3.0	22.5	114.0±4.8
^{9}Li	57.0±5.3	76.5±7.1	24.8	80.4±6.7

Table 4.2: Goldhaber σ_0 parameters extracted from incident ^{12}Be projectile. All values tabulated are in units of MeV/c and are expressed in terms of standard deviation σ. Shown tabulated here are the extracted σ_0, the momentum resolution, and the measured momentum spread of the fragment.

Fragment	σ_0	Resolution	σ_{exp}
^{8}He	52.0±13.4	34.5	94.8±21.3
^{6}He	63.1±7.5	33.0	116.3±13.2
^{9}Li	66.5±9.2	27.9	107.4±13.9

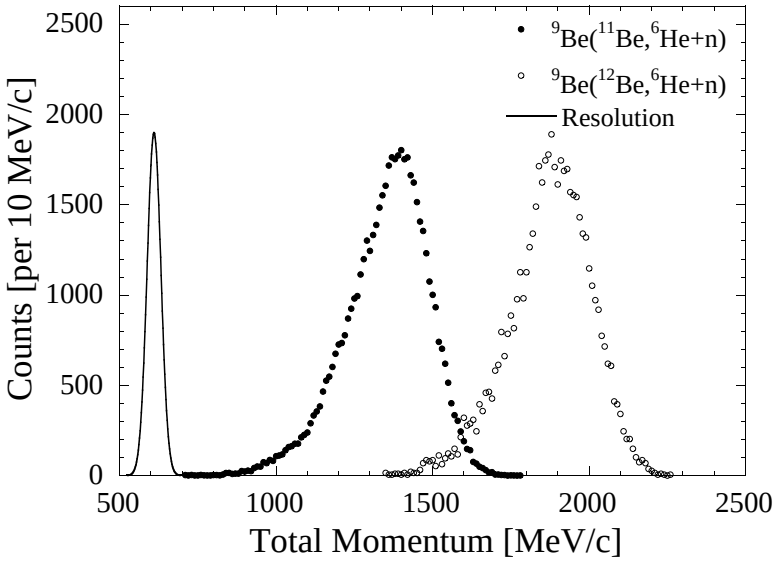

Figure 4.1: ^{6}He Momentum distribution measured in neutron coincidence. The distribution from incident ^{12}Be is shifted by +500 MeV/c and is normalized to the same area as (^{11}Be,^{6}He+n) spectrum for the purpose of comparison. Also shown is a distribution of the total momentum resolution calculated at mid-target energy of approximately 28 MeV/u, corresponding to a total momentum of 1370 MeV/c. The curve has been shifted down for display purposes.

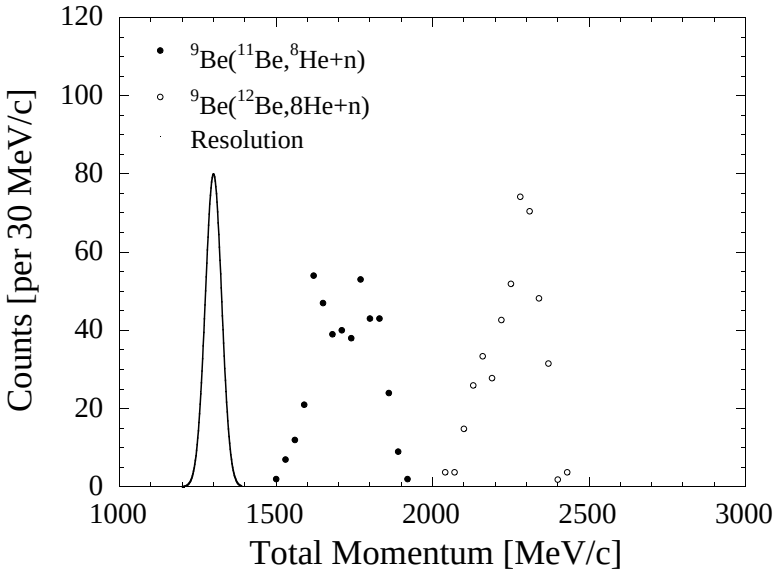

Figure 4.2: ^{8}He Momentum distribution measured in neutron coincidence. The distribution from incident ^{12}Be is shifted by +500 MeV/c and is normalized to the same area as (^{11}Be,^{8}He+n) spectrum for the purpose of comparison. Also shown is a distribution of the total momentum resolution calculated at mid-target energy of 27.7 MeV/u, corresponding to a total momentum of 1840 MeV/c. This curve has been shifted down for display purposes.

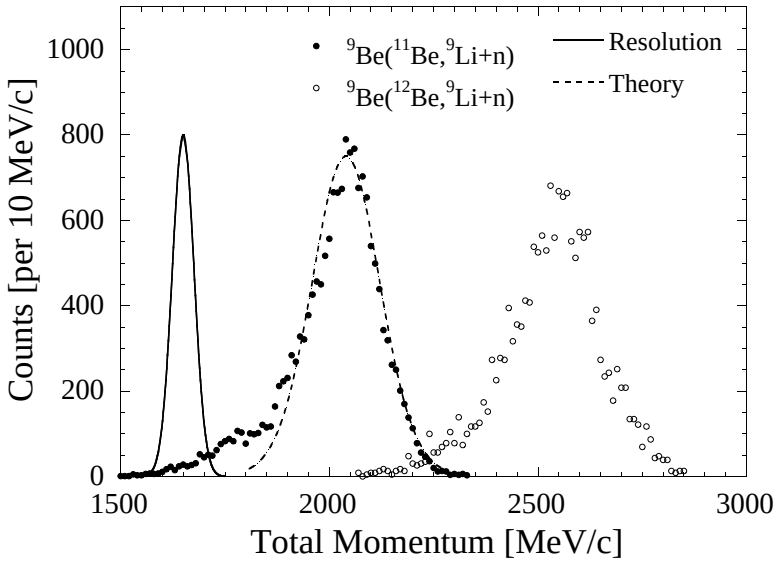

Figure 4.3: ^{9}Li Momentum distribution measured in neutron coincidence. The distribution from incident ^{12}Be is shifted by +500 MeV/c and is normalized to the same area as (^{11}Be,^{9}Li+n) spectrum for the purpose of comparison. A calculated momentum distribution of ^{9}Li using single neutron knock-out from a ^{11}Be and then rescaled by 9/10 is shown (dashed line). Also shown is a distribution of the total momentum resolution calculated at mid-target energy of 27.7 MeV/u, corresponding to a total momentum of 2060 MeV/c. This curve has been shifted down for display purposes.

will simplify the calculation of the final-state interactions.

In addition to the fragment momentum distribution measurement, an attempt was made to measure the fragmentation cross sections. The results are summarized in Table 4.3. This measurement should be only taken as an order-of-magnitude estimate. While we do not attempt to make a theoretical prediction for the production cross section for ^{7,9}He, it is possible to make an estimate for the ^{10}Li cross section from ^{11}Be breakup using the technique proposed by [42]. Using this theory, which uses an eikonal model to calculate the cross section of the breakup, a total single-particle cross section of 15.6 mb was obtained (stripping: 12.0 mb, diffraction dissociation: 3.6 mb). Using spectroscopic factors obtained from [43] (Table, 4.4) $\sigma(^{11}\mathrm{Be},^{9}\mathrm{Li}+\mathrm{n}(1s_{1/2}))$=25 mb was obtained. The estimated observed cross section is on the order of 6 mb.

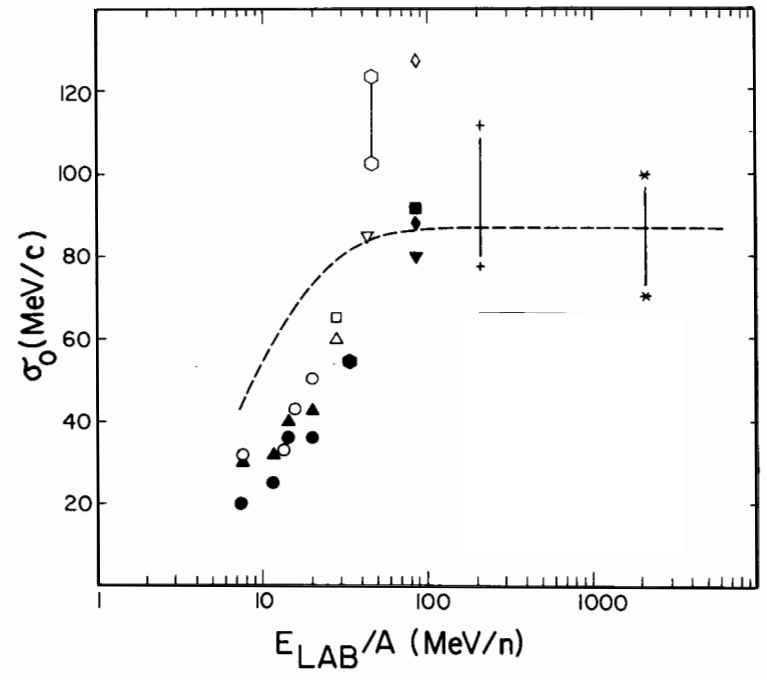

Figure 4.4: The systematics of σ_0 as a function of projectile bombarding energy [45]. It is clear that there is a trend of increasing σ_0 with increasing beam energy in the region between 10 to 100 MeV per nucleon. The reactions corresponding to these data points can be found in [45].

Table 4.3: Production cross sections of ^{7,9}He, and ^{10}Li

Fragment	^{12}Be (mb)	^{11}Be (mb)	^{10}Be (mb)
^{7}He	28.2	32.2	10.5
^{9}He	1.1	0.35	- -
^{10}Li	5.0	6.2	- -

Table 4.4: Spectroscopic Factor for (^{11}Be,^{10}Be) and (^{10}Be,^{9}Li) obtained from [43]

Reaction	State	Spectroscopic Factor
(^{11}Be,^{10}Be)	$s_{1/2}$	0.74
	$p_{3/2}$	1.27
	$d_{5/2}$	0.18
(^{10}Be,^{9}Li)	$p_{3/2}$	2.29
	$p_{1/2}$	0.35

4.2 Model for Calculation of Final-State Interaction

The potential scattering model calculates the interactions between the neutron and the core fragment in the unbound systems. This model is similar to those used in [28, 44]. In essence, the calculation assumes that a reaction mechanism described in the Goldhaber model applies in the case at hand, thus allowing the sudden approximation to be made. As such, the neutron wave function after the breakup reaction is taken to be the same as that of the initial nucleus. The neutron wave functions are calculated using a single-particle Woods-Saxon potential:

$$V(r) = \frac{V_0}{1 + \exp[\frac{r - r_0}{a}]}, \tag{4.2}$$

with r_0=1.25 fm and a = 0.7 fm. For each final-state interaction calculation, the potential well depth is adjusted to reproduce the known binding energy of the initial state, and the momentum and energy distributions of the final state are calculated based on some presumed scattering length a_s ($l = 0$) or decay energy ($l > 0$). The spin-orbit interaction is included in the effective potential V_0. It is reasonable to use a purely real potential in this model because the states probed here are predominantly single-particle states. In probing the the core + n unbound systems, the first excited states of the core are much higher compared to the unbound states. As such, there will not be much coupling between the low-lying states of the unbound systems studied here with the excited states of the core, which allows it to be treated as elastic scattering between the two bodies. The lowest excited states of the core in the systems analyzed in this work are shown in Table 4.5.

The neutron wave function of the initial state is then expanded with the final-state continuum eigenstates, which for an unbound system asymptotically must become the free-particle solution for angular momentum. The bound initial state is characterized

Table 4.5: The lowest known excited energy for ^{6,8}He and ^{9}Li taken from [51].

Isotope	First Excited State (MeV)
^{6}He	1.797 ± 0.025
^{8}He	2.8 ± 0.4
^{9}Li	2.691 ± 0.005

as:

$$\psi_0(\vec{r}) = \frac{\chi_{l_0}(r)}{r}\, Y_{l_0,m_0}(\theta,\phi), \tag{4.3}$$

and the continuum eigenstates in the core + n unbound nucleus have the eigenfunctions:

$$\phi_k(\vec{r}) = \frac{u^k_{l_1}(r)}{r}\, Y_{l_1,m_1}(\theta,\phi), \tag{4.4}$$

where k denotes the wave vector in the lab frame, l_0,m_0 and l_1,m_1 denote the initial and final angular momentum states. The amount of overlap between these two wave functions becomes:

$$a_0(k) = \delta_{l_0,l_1}\delta_{m_0,m_1}\int_0^\infty \chi_{l_0}(r)\; u^k_{l_1}(r)dr. \tag{4.5}$$

In the present model, the recoil effects from the breakup have been neglected. However, the presence of recoil terms could induce transitions to states with angular momenta other than l_1, m_1. This effect may be important for the ^{11}Be breakup.

The continuum wave function as obtained from solving the Schrödinger equation is asymptotically the spherical free-particle solution for angular momentum:

$$A_0(\vec{k}) = \frac{1}{k'}\delta(k'-k)\; Y_{l_0,m_0}(\hat{k}), \tag{4.6}$$

and the momentum distribution is given simply as:

$$W(\vec{k}) = \left|\frac{1}{k}\, a_0(k)\; Y_{l_0,m_0}(\hat{k})\right|^2. \tag{4.7}$$

After integrating over the delta function and summing over final states and averaging, the expression simplifies to:

$$W(k) = \frac{1}{4\pi} \left| \frac{1}{k} a_0(k) \right|^2 . \tag{4.8}$$

4.3 Parameterization of the Continuum States

An important quantity in the parameterization of the continuum states is the phase shift δ_l. In terms of phase shift δ_l, the solution of the Schrödinger equation far away from the potential with an azimuthally symmetric $V(r)$ which vanishes as $r \to \infty$ is

$$R_l(r) = a_l k \left[\cos(\delta_l) j_l(kr) - \sin(\delta_l) \eta_l(kr) \right], \tag{4.9}$$

where $R_l(r)$ is the radial wave function, $k = \frac{\sqrt{2\mu E}}{\hbar}$, μ is the reduced mass of the two body system, and $j_l(kr)$ and $n_l(kr)$ are the regular and irregular spherical Bessel functions.

In practice, $R_l(r)$ is a numerical solution to the Schrödinger equation. By comparing $R_l(r)$ far away from the potential with the asymptotic form of the continuum wave function, one can directly obtain the phase shift (Equation 4.9). For $l > 0$ resonances, the energy of resonance is specified, and V_0 of the Woods-Saxon potential is adjusted while keeping a and r_0 fixed so that the phase shift changes from $\pi/2$ to $-\pi/2$. This is a reasonable to vary simply one parameter because the detailed shape of the potential is not important for low-energy neutron scattering.

At zero energy and for $l = 0$ (s-wave), it is convenient to introduce a quantity scattering length a_s. Using effective range theory, a_s can be expressed as

$$k \cot \delta_0 = -\frac{1}{a_s} + \frac{1}{2} r_0 k^2 \left(+ \mathcal{O}\left(k^4\right) \right), \tag{4.10}$$

and for $k \to 0$, the scattering length a_s can be expressed as

$$a_s \to -\frac{\delta_0}{k}, \tag{4.11}$$

Since the scattering length can be related to the ratio between the phase shift and the wave vector, the potential can simply be adjusted to reproduce the desired s-wave scattering length. In the presence of attractive potentials, the scattering length is positive, and a numerically negative scattering length a_s represents unbound states. The equivalent energy of the virtual state can be expressed as $E = \hbar^2/2ma_s^2$. This is a very useful result because it implies that the energy of bound and unbound states can be determined by performing low-energy scattering experiments to determine the scattering length. The ability to deduce the energies of the bound and unbound states without needing to know the details of the potential is an important feature of this technique.

4.4 Computing Energy Distributions

The computer code which generated the energy distributions used in this analysis was based on programs FSI1 and BDELTA written by P.G. Hansen. In order to compute an energy distribution as a result of the final-state interactions, a few input parameters are needed. First, one needs to specify the size of fragment that the neutron is being scattered from, and one also must choose the resonance energy ($l > 0$) or scattering length a_s ($l = 0$). In addition, the effective binding energy of the neutrons in the initial states is needed. The values used in this analysis are summarized in Table 4.6, and the wave functions of the corresponding effective binding energies are shown in Figures 4.5 and 4.6. These initial states are then expanded into the eigenstates of the final unbound states to obtain the energy distributions.

Some examples of the expansion of the bound initial states with the continuum eigenstates are shown in Figures 4.7, 4.8, 4.9, and 4.10. The model used to compute the final-state interaction is dependent on both the initial and the final states, and thus, different initial states can influence the calculated final-state interactions.

Table 4.6: Effective binding energies of neutrons in ^{12,11,10}Be nucleus.

Nucleus	State	Effective Binding Energy (MeV)	Wood Saxon Depth (MeV)
^{12}Be	$1s_{1/2}$	3.169	64.369
(S_n=3.169 MeV)	$0p_{1/2}$	3.489	38.514
	$0d_{5/2}$	4.95	74.737
^{11}Be	$1s_{1/2}$	0.503	55.962
(S_n=0.503 MeV)	$0p_{3/2}$	6.6	47.646
^{10}Be	$1s_{1/2}$	8.49	87.605
(S_n=6.812 MeV)	$0p_{3/2}$	6.81	50.916

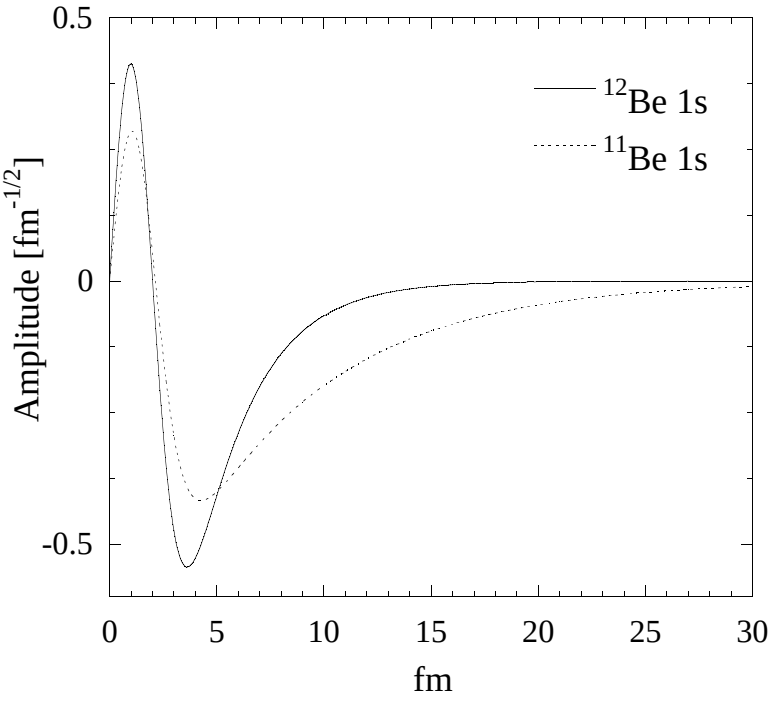

Figure 4.5: Radial wave function $\chi_0(r)$ of the s-state in ^{11,12}Be. The long tail in the neutron wave function of ^{11}Be is a result of the low binding energy.

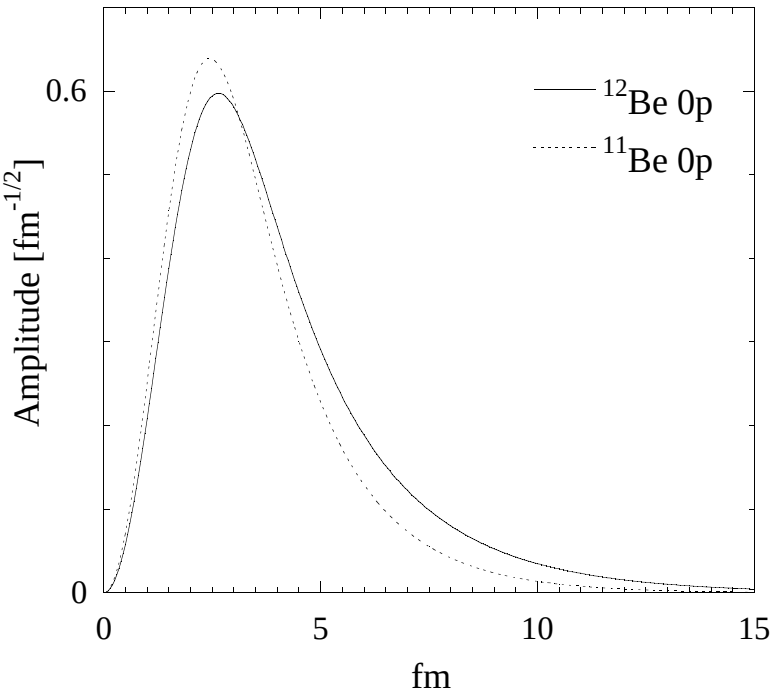

Figure 4.6: Radial wave function $\chi_0(r)$ of the p-state in ^{11,12}Be.

In the case of the ^{7}He energy distribution, the p-neutrons from the ^{12}Be are less tightly bound than those from ^{11}Be (binding energy of 3.489 MeV versus 6.6 MeV). A smaller binding energy results in a slightly more diffuse neutron wave function, which enhances the contributiion to lower energy with a initial ^{12}Be nucleus (Figure 4.7). In the case of the ^{10}Li energy distribution, such an effect is much more pronounced (Figures 4.8 and 4.9), because the diffuse wave function of the ^{11}Be neutron (Figure 4.5), has a significant contribution to the region of low decay energy. The energy distribution for a ^{9}He calculated from an incident ^{11}Be is shown in Figure 4.10.

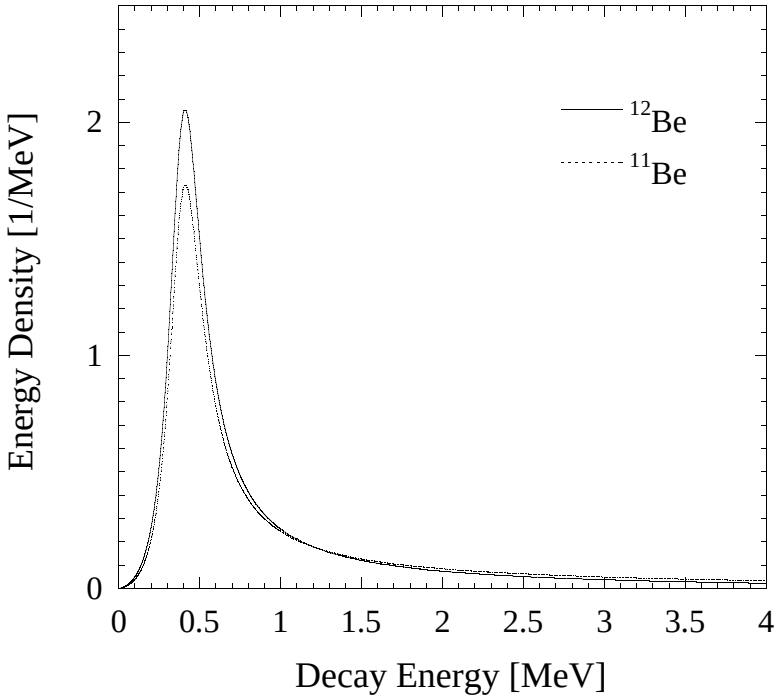

Figure 4.7: Energy Distribution of ^{6}He+n system at E_d= 450 keV calculated using the potential scattering model using initial ^{11,12}Be nucleus.

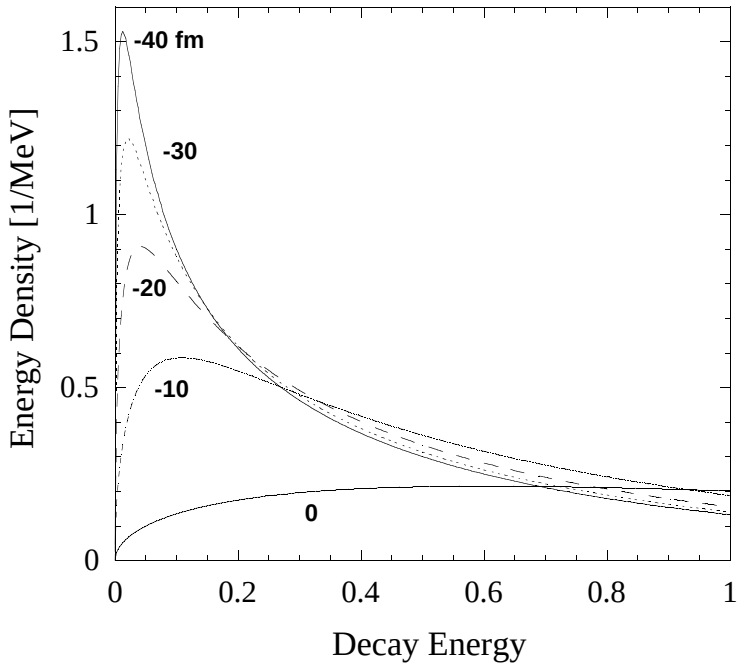

Figure 4.8: Energy Distribution of ^{9}Li+n expanded using a ^{12}Be s-state and the unbound states of ^{9}Li. Shown are the energy distributions corresponding to various scattering lengths.

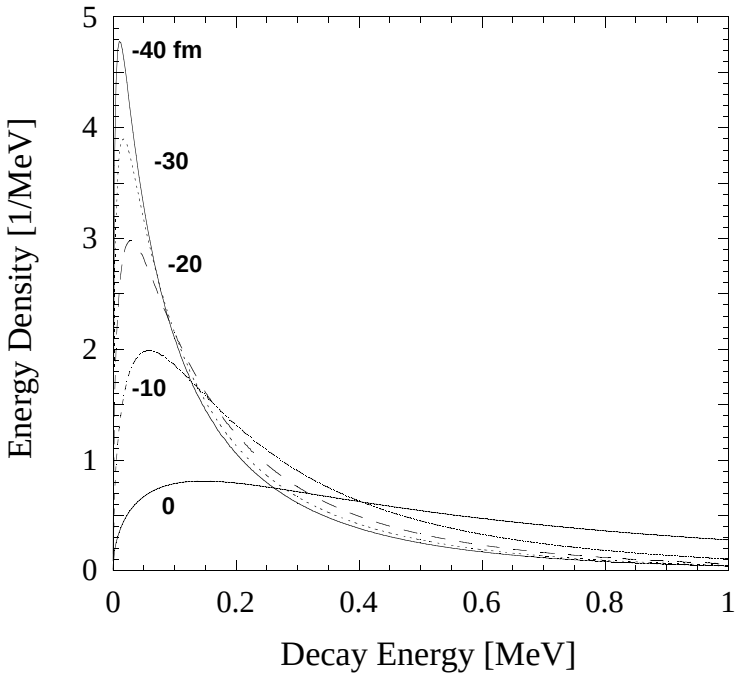

Figure 4.9: Energy Distribution of ^{9}Li+n expanded using a ^{11}Be s-state and the unbound states of ^{9}Li. Shown are the energy distributions corresponding to various scattering lengths.

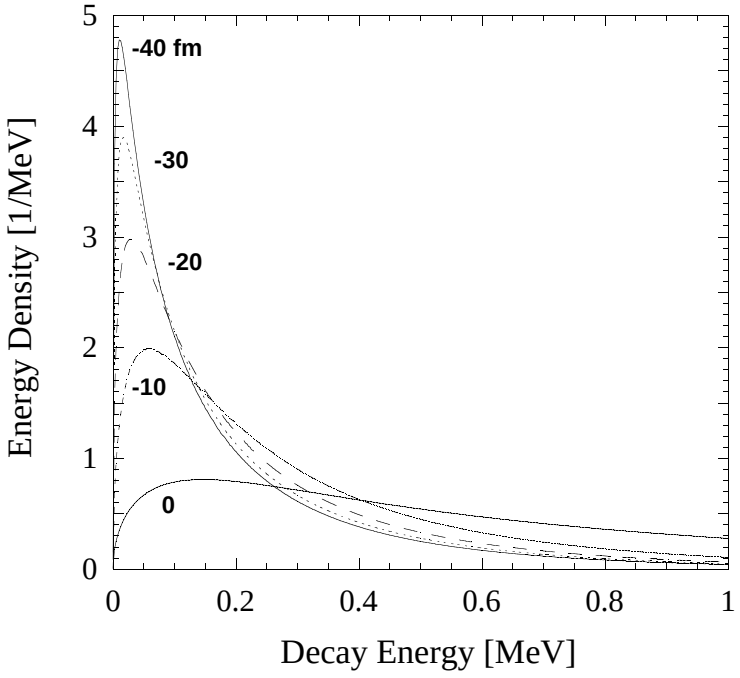

Figure 4.10: Energy Distribution of ^{8}He+n expanded using a ^{11}Be s-state and the unbound states of ^{8}He. Shown are the energy distributions corresponding to various scattering lengths.

Chapter 5

^{6}He+n

5.1 Introduction

The p-resonance in the unbound ^{7}He was first observed by Stokes and Young in 1967 by a means of a ^{7}Li(t,^{3}He)^{7}He direct reaction using a 22-MeV triton beam [46] on a 0.4 mg/cm^2 ^{7}Li target, and the resonance energy (peak position) was measured to be $E_r = 420 \pm 60$ keV with $\Gamma = 170 \pm 40$ keV. The current literature value for the p-resonance for ^{7}He of $E_r = 440 \pm 30$ keV and $\Gamma = 160 \pm 30$ keV was reported in 1969 [10] by the same authors through a repeat of their original experiment with the same beam energy, but with a thinner target (100 μg/cm^2 of ^{7}Li). The present work will perform three separate measurements on the ^{7}He using final-state interactions.

5.2 Results

Figure 5.1 shows the velocity difference spectra scaled to number of incoming ^{10,11,12}Be beams particles. The asymmetry of the two peaks is caused by acceptance effects: neutrons moving faster than the ^{6}He fragments are more likely to be found within 5 degrees of the fragment than the slower neutrons. The two important features of

the spectra are (1) the ^{11}Be spectrum has a greater intensity near the zero velocity difference region than the ^{12}Be spectrum and (2) the low intensity of the ^{6}He + n spectrum with an incident ^{10}Be nucleus. The first feature can be attributed to the low binding energy of the s-state of the ^{11}Be neutron, and these slow (halo) neutrons correspond to zero velocity difference. The second feature illustrates that the ^{6}He is formed mainly by α-particle knockout, which is not accompanied by fast neutrons.

The experimental data is fitted with simulated velocity distributions generated using energy distributions computed from the potential scattering model (Chapter 4). The data is fitted using techniques already described in Section 3.6. Figures 5.2, 5.3, and 5.4 are ^{6}He+n velocity difference spectra with no correction for neutron detection efficiency. Each of the fits shown represents the lowest χ^2 fit. The energy for the p-state was found to be 448 ± 23, 452 ± 19, and 422 ± 20 MeV for ^{12,11,10}Be initial nucleus, respectively. The uncertainty is taken as the range in the resonance where $\triangle\chi^2 < 4$, corresponding to 95% confidence level. Using the average of these three values and the standard deviation as an error, a resonance of 440 ± 16 keV is obtained. The results presented in this analysis are consistent with the current literature value of $E_r = 440 \pm 30$ keV measured by [10].

The potential scattering model does not have a separate parameter specifying the width of a resonance. The selection of a resonance energy specifies the set of continuum eigenfunctions used to expand the bound initial states. The energy distribution from the expansion of the ^{12,11}Be can be found in Figure 4.7. The width Γ as measured by the FWHM of the energy distributions from the initial ^{11}Be (^{12}Be) nucleus is 273 MeV (252 MeV). They are not in agreement with the previous literature value of $\Gamma = 160 \pm 30$ MeV [10]. However, the data shown here shows a good fit using a broader energy distribution.

As a demonstration for the sensitivity of the method, Figures 5.5, and 5.6 show the

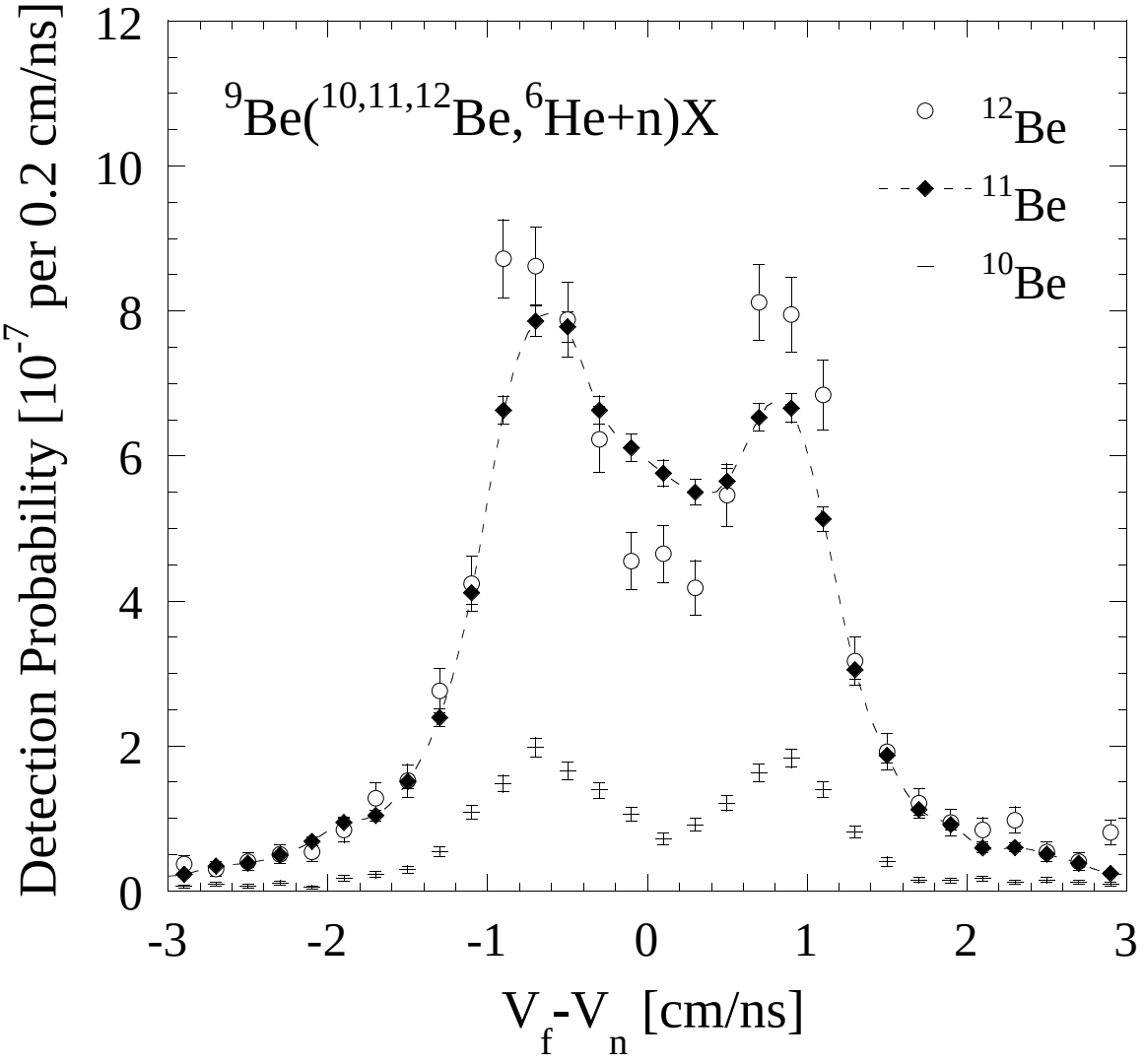

Figure 5.1: Velocity difference spectra of ^{6}He+n scaled to the number of incoming beam particles. The scale has not been corrected for geometrical acceptance and detector efficiency. The uncertainties are purely statistical. Depending on the initial nucleus, the velocity difference spectrum can have a very different appearance even though it is the same resonance being probed. In the case of the incident ^{11}Be, the enhancement near zero relative velocity comes from the loosely-bound neutrons in the *s*-state, which do not interact in a ^{6}He+n system.

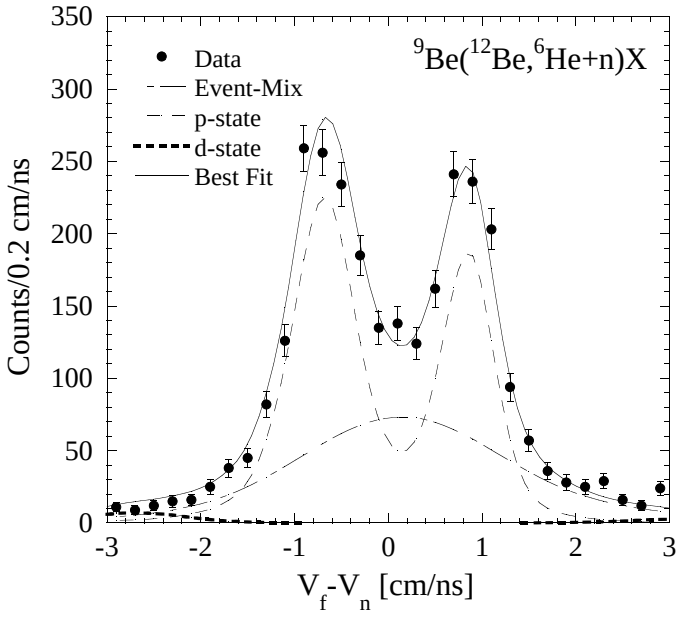

Figure 5.2: Velocity difference spectrum of the ^{9}Be(^{12}Be,^{6}He+n)X system. Shown are the experimental data with statistical error bars, the computer simulation of a p-wave resonance at 450 keV, a d-wave resonance with 5 MeV of effective binding energy, and an event-mixed background. The best fit consists of: event-mixed background: 36%, p-wave: 62%, and d-wave: 2%.

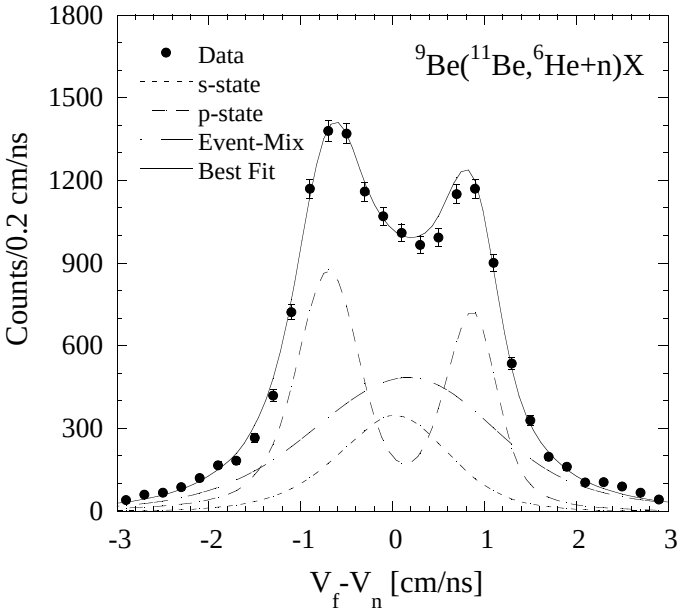

Figure 5.3: Velocity difference spectrum of the ^{9}Be(^{11}Be,^{6}He+n)X system. Shown are the experimental data with statistical error bars, the computer simulation of a p-wave resonance at 450 keV, a s-wave (a_s=0 fm) scattering, and an event-mixed background. The best fit consists of: the background: 39%, p-wave: 44%, and s-wave: 17%. The contribution of the non-interacting scattering of the loosely-bound neutron in the ^{11}Be describes the essential difference between the ^{11}Be and ^{12}Be data.

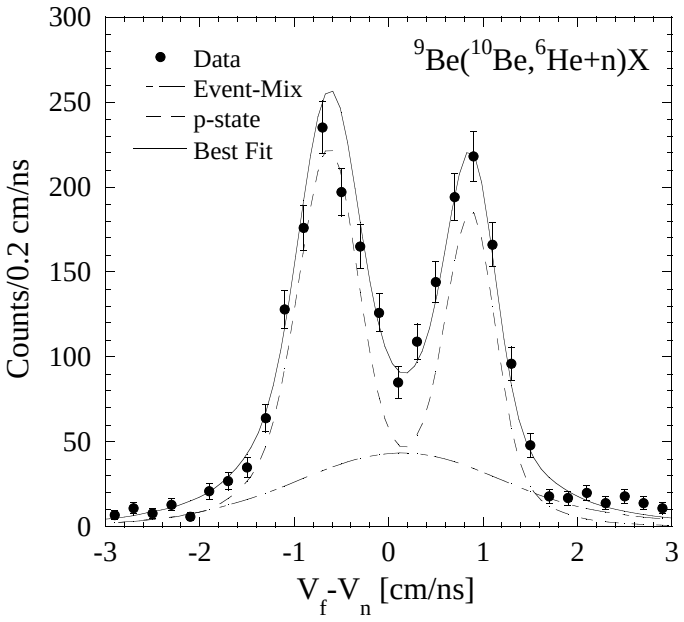

Figure 5.4: Velocity difference spectrum of the ^{9}Be(^{10}Be,^{6}He+n)X system. Shown are the experimental data with statistical error bars, the computer simulation of a p-wave resonance at 420 keV and an event-mixed background. The best fit consists of: the background: 26%, and p-wave: 74%

best fit using a p-state resonance energy in the range between 400 and 500 keV. The region covered by the 100-keV band encompasses the range of the statistical errors limited by the counting in the experiment. However the use of a χ^2 minimization suggests (Figure 5.7) a much better precision in determination of the energy, on the order of 20 keV.

The background generated using an event-mixing technique accounts for approximately 40% of the total intensity of the velocity-difference distributions for ^{11,12}Be projectiles, and 26% for the ^{10}Be. Even though the ^{12}Be can be fitted with only a p-resonance on top of the event-mixed background, the fit is slightly improved by introducing a d-wave resonance with effective binding energy of 5 MeV (See Table 4.6). For the incident ^{11}Be nucleus, the fit also includes an s-wave component in addition to the event-mixed background. The inclusion of an s-wave scattering at $a_s = 0$ fm for the ^{11}Be initial state was required to describe the data, and can be interpreted as

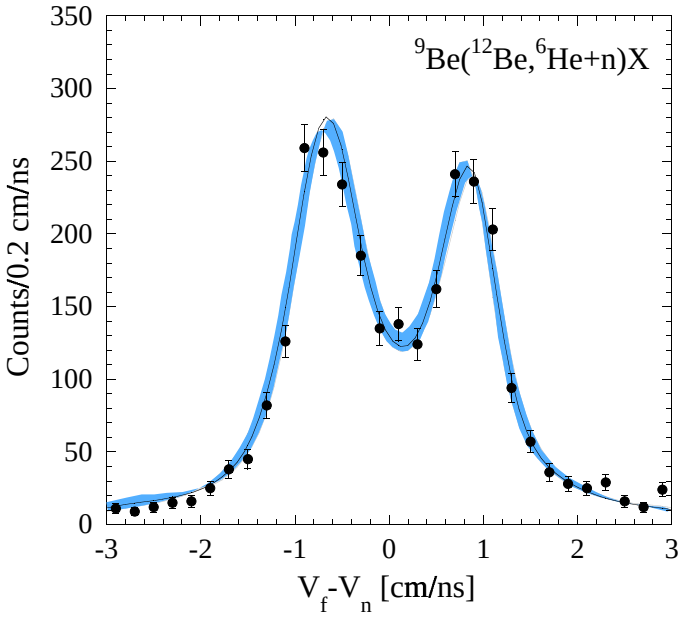

Figure 5.5: Error estimate of p-resonance in the ^{9}Be(^{12}Be,^{6}He+n)X. The shaded region represents the theoretical fits for the region $400 < E_r < 500$ keV, and the solid line represents the $E_r = 450$ keV fit, which is the minimum χ^2 fit.

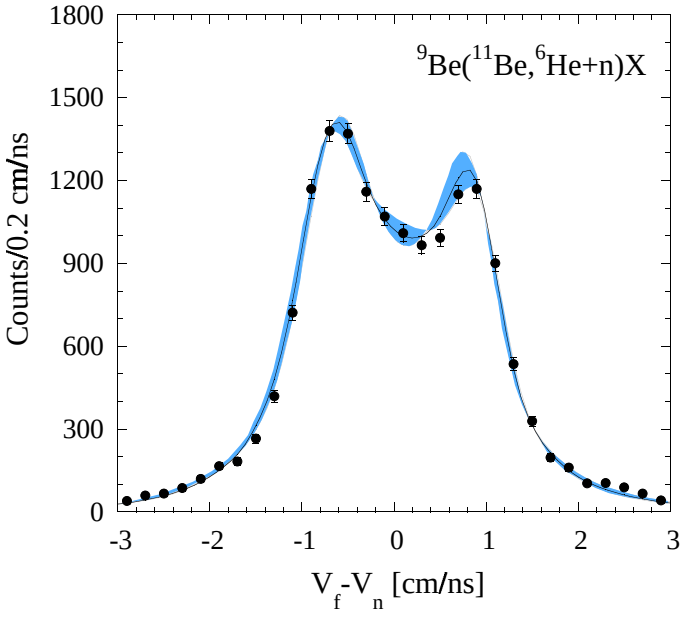

Figure 5.6: Error estimate of p-resonance in the ^{9}Be(^{11}Be,^{6}He+n)X. The shaded region represents the theoretical fits for the regions between $400 < E_r < 500$ keV, and the solid line represents the $E_r = 450$ keV fit, which is the minimum χ^2 fit.

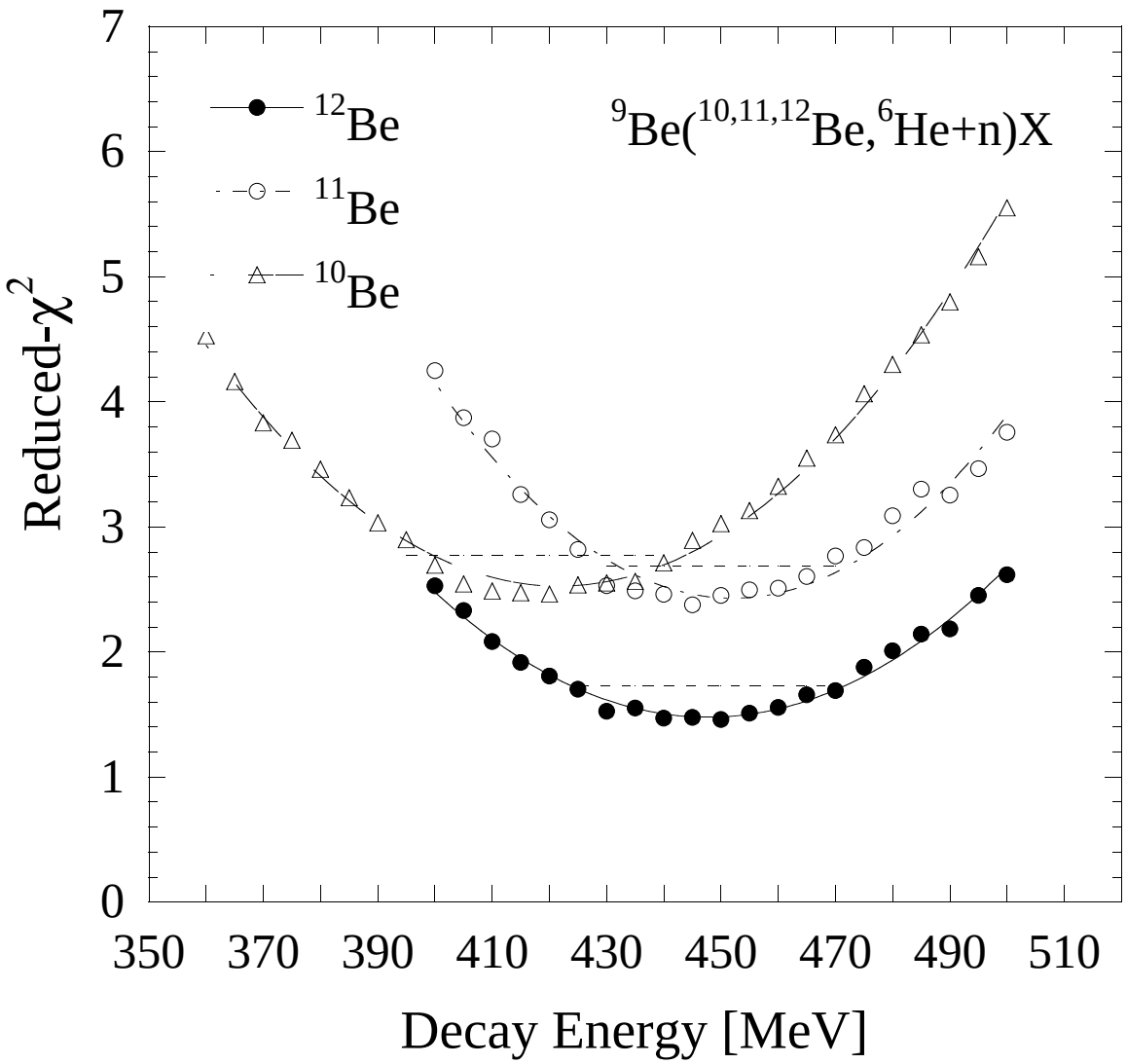

Figure 5.7: Reduced-χ^2 of fits to ^{9}Be(^{12,11,10}Be,^{6}He+n)X data as a function of the decay energy of the p-state. For the ^{12,11}Be reaction, the minimum χ^2 uses three separate components in the fit. The minimization procedure uses the 22 data points between -2.1 cm/ns and 2.1 cm/ns. The four free parameters used in the fitting are the 1) total intensity (taken to be the same as the total number of events), 2) systematic shift in the computer-simulated relative velocity spectra (Section 3.6), and 3) the relative intensities amongst three different components requires two free parameters for fitting. This yields 18 degrees of freedom. In the case of ^{10}Be, there is a total of 19 degrees of freedom because there is only a two-component fit in the spectrum. The curves shown correspond to a second-order fit for the reduced-χ^2, and the dashed lines represent the reduced-χ^2 value that corresponds to a 95% confidence level. Using this as a guide, the typical uncertainty is on the order of 20 keV.

Table 5.1: Approximate occupation of the available neutron orbitals in the reaction ^{9}Be(^{A}Z,^{7}He)X.

Projectile	$0d_{5/2}$	$1s_{1/2}$	$0p_{1/2}$	$0p_{3/2}$
^{12}Be	1.0	0.4	0.4	2.0
^{11}Be	0.2	0.8	0	2.0

the non-interacting s-state neutrons from the ^{11}Be detected together with the ^{6}He.

The need for a non-interacting s-wave component to describe the ^{7}He data with the ^{11}Be projectile seems very apparent; since the ^{7}He exists as a $p_{3/2}$-resonance, an interaction in the $l = 0$ channel is not expected. Using the observed spectroscopic factors of ^{11}Be [9, 54] as a guide, we can estimate the occupation of the available neutron orbitals for ^{9}Be(^{A}Z,^{7}He)X (Table 5.1). Approximately 28% of the available neutron orbitals are in the non-interacting s-state. This appears to explain why there is so much intensity in the region of zero relative velocity. However, there is one problem with this reasoning: ^{12}Be also contains a significant s-component in the initial state.

A simple shell-model predicts that ^{12}Be is a closed shell, and therefore there would be no occupancy in the s-state. However, recent data by Navin *et al.* [55] observed direct evidence for the breakdown in the shell closure in ^{12}Be. For a single neutron-removal from ^{12}Be, a spectroscopic factor of 0.53 ± 0.08 was obtained for the $1s_{1/2}$ state and 0.45 ± 0.07 for the $0p_{1/2}$ [55]. An estimate of the occupation of the available neutron orbitals based on these spectroscopic factors is also shown in Table 5.1. Approximately 10% of the neutrons are in the s-state, which is about one-third as many as the reaction in ^{11}Be. One might ask why there was no need for a separate s-state fit in the fitting of the ^{12}Be data. The reason is that the velocity difference corresponding to a scattering at $a_s = 0$ fm from a ^{12}Be projectile has the same shape as the event-mixed background. This is not true in the case for ^{11}Be, where the

relative velocity distribution for the s-wave is narrower than the event-mixed spectra (Figure 5.3), which caused by the fact that the s-state neutron of the ^{11}Be is much more loosely bound than the ^{12}Be. Part of this contribution is presumably included in the event-mixed background. Thus, the enhancement at zero relative velocity for initial ^{11}Be is a result of low binding of the neutron in the s-state, not merely because of the existence of the s-state.

Chapter 6

^{9}Li+n

6.1 Introduction

In 1985, Tanihata *et al.* [4] first reported that ^{11}Li possesses an unexpectedly large interaction cross section. This large cross section is due to the fact that ^{11}Li is a three-body system consisting of a ^{9}Li core and two loosely-bound neutrons. Even more intriguing is the fact that ^{10}Li is an unbound system, so the stability of the ^{11}Li is partly due to the neutron-neutron pairing force between the two halo neutrons. Thus, understanding the ^{10}Li nucleus is critical towards the understanding of the ^{11}Li three-body problem, as it is essential to understand the interaction between any binary subsystems. The neutron-neutron interaction is well known, so considerable effort has been put forth in studying the ^{10}Li.

An issue of considerable debate is whether the ground state of ^{10}Li is a p-state, as predicted by the simple shell model, or a low-lying s-state. As mentioned earlier, in Section 1.4, there is evidence suggesting that an intruder s-state is the ^{10}Li ground state. Since the first time ^{10}Li was observed, by Wilcox *et al.* [49] in 1975, there has been a number of interesting experimental results with regard to this nucleus. A good summary of the experimental results on ^{10}Li can be found in [12, 28]. There are a

number of observations of peaks which were interpreted as p-state resonances, most recently by Caggiano *et al.* [12].

The difficulty with a virtual state having l=0 and essentially single-particle strength is that it does not exhibit a resonance-like structure. In the energy spectra of the final state, it will manifest itself by a rapid rise in cross section just above the threshold followed by a slow decay towards higher energies. The resulting line shape is asymmetric with "energy" and "width" roughly comparable (See Figures 4.8, 4.9). There two previous experimental results [27, 28] (Section 1.4) both observed evidence for an interaction in the l=0 channel with scattering length $a_s < -20$ fm via a central peak in the region of zero relative velocity. In addition, Zinser *et al.* [44] from GSI reported an experimental observation of the $l = 0$ interaction using a breakup of ^{11}Be at 280 MeV/u. The observed neutron angular distribution suggested an s-ground state with scattering length $a_s < -20$ fm from an analysis that averaged over an estimated recoil contribution. The same effect was seen in ^{11}Li; the group argued that since the ^{11}Li is very loosely bound, the stripping of one of these neutrons would not likely excite the ^{9}Li core, and hence, the discovered s-state therefore must be a ground state [44] (Figure 6.1). A subsequent experiment confirms this assertion, demonstrating that only $7.5 \pm 2.5\%$ of ^{9}Li formed from proton-stripping of ^{11}Be are in the 2.7 MeV excited state [53]. The objective of the present work is to confirm the low-lying s-state in ^{10}Li by using ^{12,11}Be as the initial projectiles and to pin down the angular momentum assignment making use of our knowledge of the structure of ^{12,11}Be.

6.2 Results

The velocity difference distribution between the detected neutrons and the ^{9}Li fragment are analyzed in the same manner as the ^{7}He. Figure 6.2, shows the velocity difference spectra scaled to the incident ^{10,11,12}Be projectiles. The ^{10}Be projectile can-

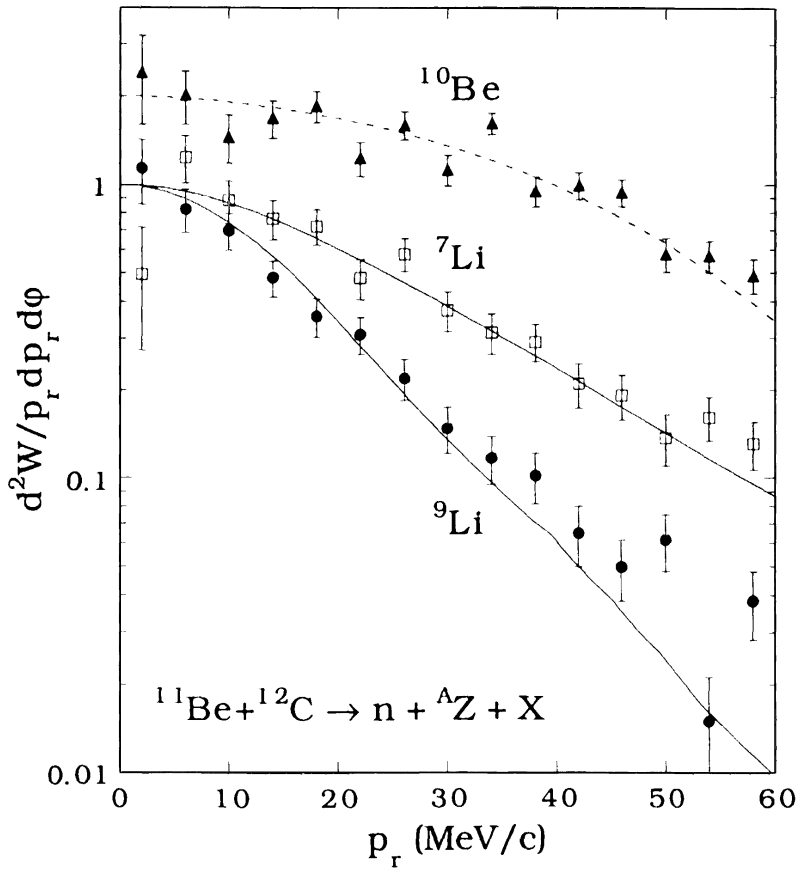

Figure 6.1: Data from Zinser *et al.* [44]. Shown are the radial momentum distributions of the select fragments detected with neutron coincidence from an incident ^{11}Be. The most important feature of this data is the narrow momentum distribution of the observed ^{9}Li, compare to that of ^{7}Li. The solid curves through the lithium data are momentum distributions calculated using a potential scattering model similar to the one used in this work. The curve through the ^{7}Li data is a distribution corresponding to an s-wave scattering with $a_s = 0$ fm, while the curve through the ^{9}Li data is calculated using $a_s = -20$ fm. In both cases, there is a component of a p-wave resonance at 0.42 MeV.

not break up into ^{9}Li and a fast neutron, so the absence of counts in this channel shows that discrimination against neutrons from the target is satisfactory. The data from the ^{11}Be beam are clearly narrower than those from the ^{12}Be, which can be explained from the fact that ^{11}Be neutron is very loosely bound. As discussed in Section 4.4, the diffuse tail in the neutron wave function enhances the low energy region of the energy distribution, making the energy distribution for an s-state narrower for an initial ^{11}Be versus that of a ^{12}Be projectile. That difference in the energy distributions also can be observed in the narrowing of the velocity difference distributions (Figures 3.4 and 3.5). Thus, like the ^{6}He+n data present in Chapter 5, we see that the initial states can effect the observed final-state interaction in ^{9}Li+n data.

The results from the ^{9}Be(^{12}Be,^{9}Li+n)X reaction are shown in Figure 6.3. The data is fitted using four different components: s, p, and d-waves, and event-mixed background. Both the introduction of the p and d components improves the fit of the data. A p-wave resonance at approximately 0.5 MeV has been observed by [12, 48], and is included in this analysis. Because of the low relative intensity with the p-state (approximately 7%), the fit is rather insensitive to the energy of this resonance. The most pronounced feature in the data is a central peak near zero relative velocity. This is also the essential argument why this peak represents an interaction in the s-state. Energy distributions corresponding to interactions in the s-state with a ^{12}Be projectile can be found in Figure 4.8. A strong s-state interaction corresponds to a narrower energy distribution and thus would result in a narrow, central peak in the relative velocity distribution. Figure 6.4 shows the data compared to fits using different scattering lengths a_s, and Figure 6.5 shows the reduced-χ^2 as a function of scattering length. Using an analysis where $\triangle\chi^2 < 4$, corresponding to 95% confidence level, an s-wave interaction of at least $a_s < -10$ fm is deduced.

The data from the ^{9}Be(^{11}Be,^{9}Li+n)X reaction shown in Figure 6.6. The analysis

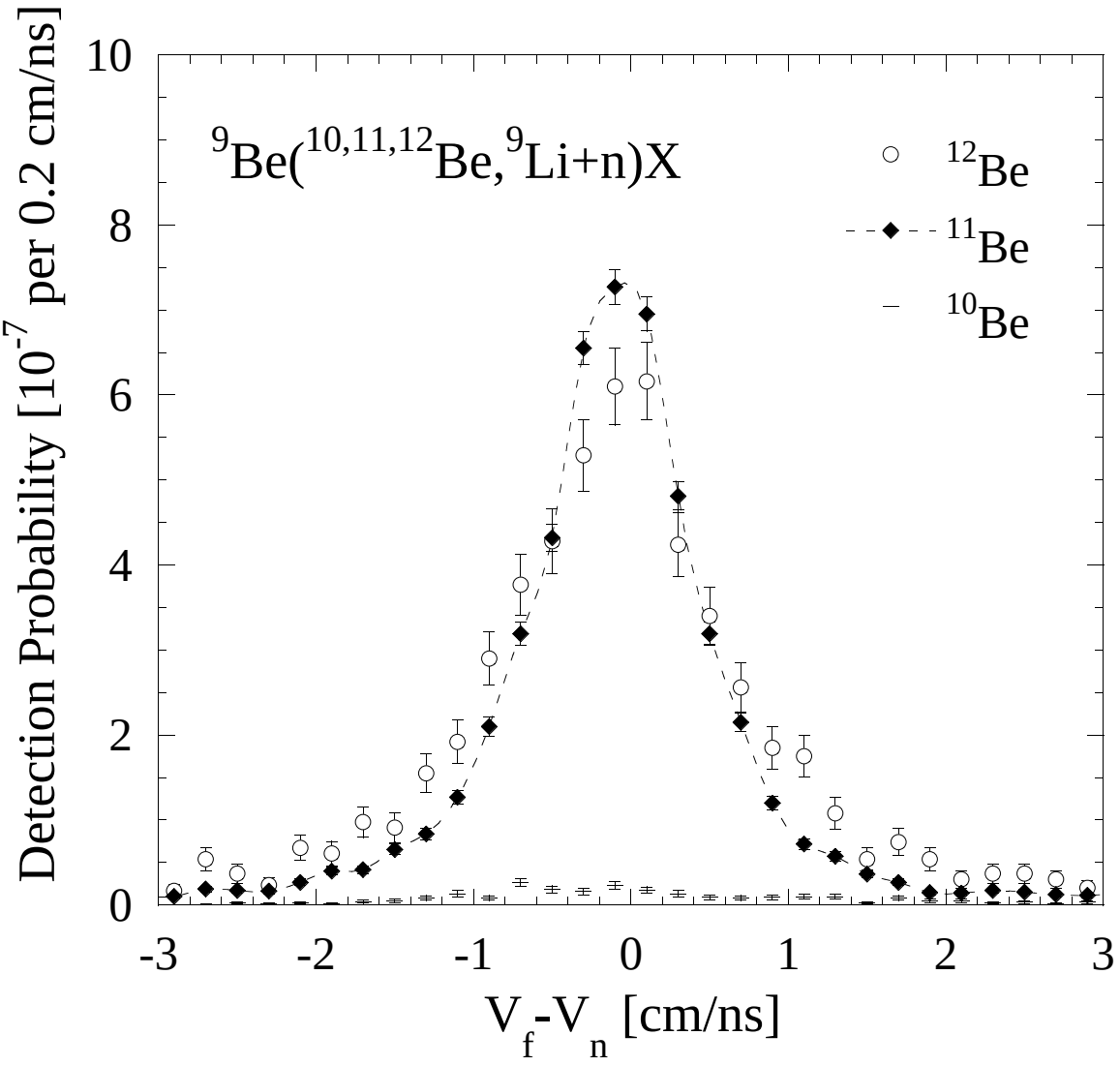

Figure 6.2: Velocity difference spectra of ^{9}Li+n with three different initial nuclei scaled to the number incident beam particles. Because of the loosely-bound *s*-state of the ^{11}Be, the peak near zero velocity is narrower than that from ^{12}Be. Note that the ^{10}Be projectile cannot break up into ^{9}Li and a fast neutron, so the absence of counts in this channel shows that the discrimination against neutrons from the target is satisfactory.

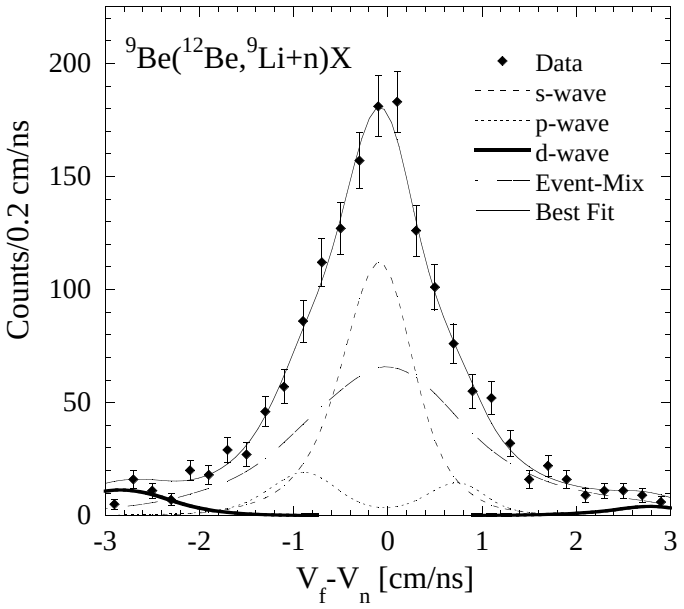

Figure 6.3: Velocity difference spectrum of the ^{9}Be(^{12}Be,^{9}Li+n)X system. Shown are the experimental data with statistical error bars, the computer simulation of a p-wave resonance at 538 keV, a a_s=-25 fm s-wave scattering, a d-wave scattering with an effective binding energy of 5 MeV, and an event-mixed background. The best fit consists of: the background: 48.%, p-wave: 7%, d-wave: 6%, and s-wave (a_s=-25 fm): 39%.

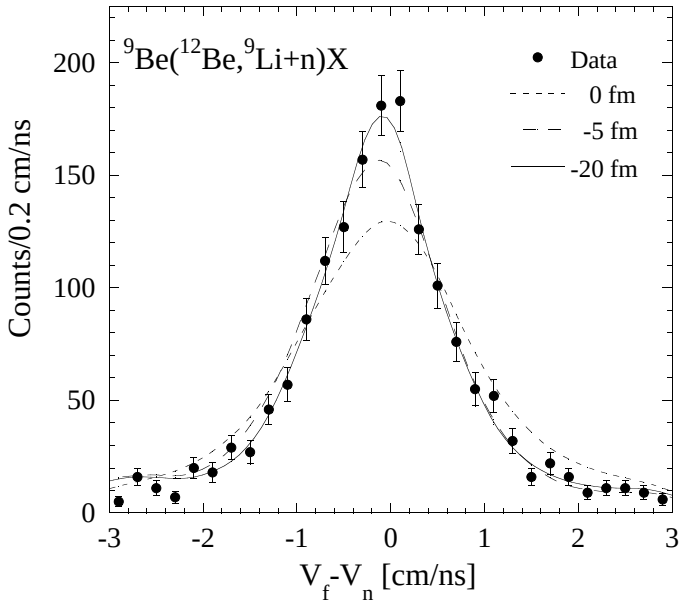

Figure 6.4: Velocity difference spectrum for the reaction ^{9}Be(^{12}Be,^{9}Li+n)X data with best-fits using scattering lengths a_s=0, -5, and -20 fm.

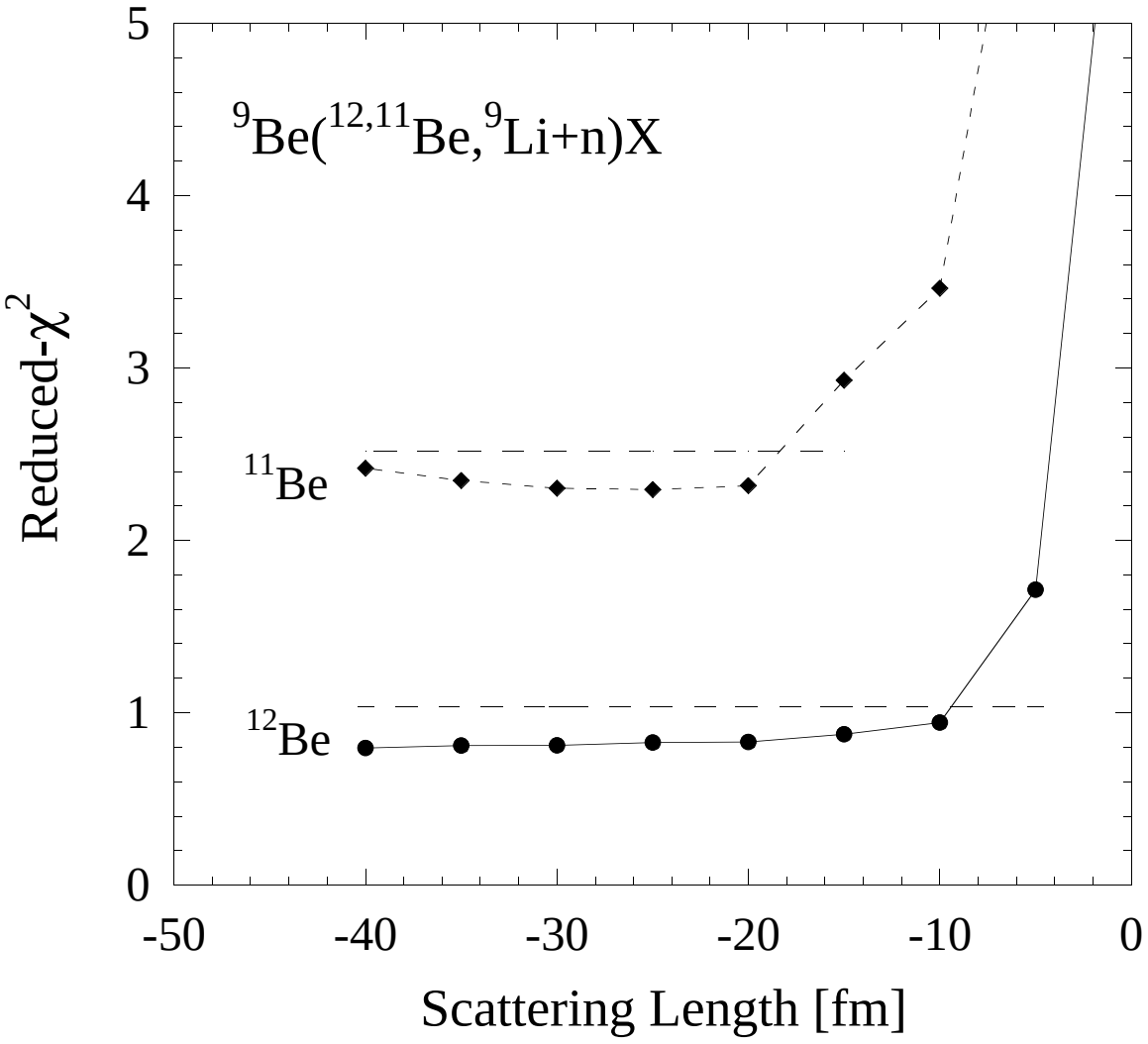

Figure 6.5: Reduced-χ^2 of fits to ^{9}Be(^{12,11}Be,^{9}Li+n)X data as a function of the scattering length a_s of the s-state. For an incident ^{12}Be nucleus, the minimum χ^2 analysis uses four separate components in the fit. The minimization procedure uses the 22 data points between -2.1 cm/ns and 2.1 cm/ns. The five free parameters used in the fitting are the 1) total intensity (taken to be the same as the total number of events), 2) systematic shift in the computer-simulated relative velocity spectra (Section 3.6), and 3) relative intensities amongst four different components requires three free parameters for fitting. This yields 17 degrees of freedom. In the case of ^{11}Be, there is a total of 18 degrees of freedom because there is only a three-component fit in the spectrum. The dashed lines represent the reduced-χ^2 value that corresponds to a 95% confidence level.

Table 6.1: Approximate occupation of the available neutron orbitals in the reaction ^{9}Be(^{A}Z,^{10}Li)X. The available neutron orbitals are the same for ^{9}Be(^{A}Z,^{9}He)X since the two unbound systems have the same number of neutrons.

Projectile	$0d_{5/2}$	$1s_{1/2}$	$0p_{1/2}$
^{18}O	1.4	0.4	2.0
^{12}Be	1.0	0.4	0.4
^{11}Be	0.2	0.8	0

uses only three separate components: s and p-waves, and event-mixed background, and the procedure is completely analogous to the analysis of ^{12}Be projectile. Just as before, a p-wave improves the fit, and the low contribution from the p-state (approximately 5%) makes it rather insensitive to the energy of the p resonance. Using χ^2 as a guide, we see an s-state interaction corresponding to a scattering length of $a_s < -20$ fm. Figure 6.7 shows a comparison of using different scattering lengths.

Table 6.1 shows the approximate occupation of the available neutron orbitals in the reaction ^{9}Be(^{A}Z,^{10}Li)X. We do not expect as much p-state in fitting the ^{11}Be data since the valence neutron is predominantly in the sd-shell. A greater contribution in the p-state is expected from the ^{12}Be projectile. Both of these effects are observed in this experiment. The ^{18}O projectile contains the highest occupancy in the p-state. As expected, data from [28] (Figure 1.6) show the largest p-state contribution.

The data from both the ^{12,11}Be projectiles show evidence of a low-lying s-state for the unbound ^{10}Li. This result is consistent with findings by [27, 28, 44]. A comparison of the results from ^{10}Li and ^{7}He data allows some important conclusions about the final-state interaction technique. If one suspects that the unbound state of core+n system is mostly a p-state, such as the ^{7}He case, one might wish to start from an initial state that also contains mostly p neutrons, such as the case of ^{10,12}Be. The ^{7}He data would suggest that using an initial state which has a loosely bound s-state such as ^{11}Be may not be the best approach, since the s-state obscures the observed

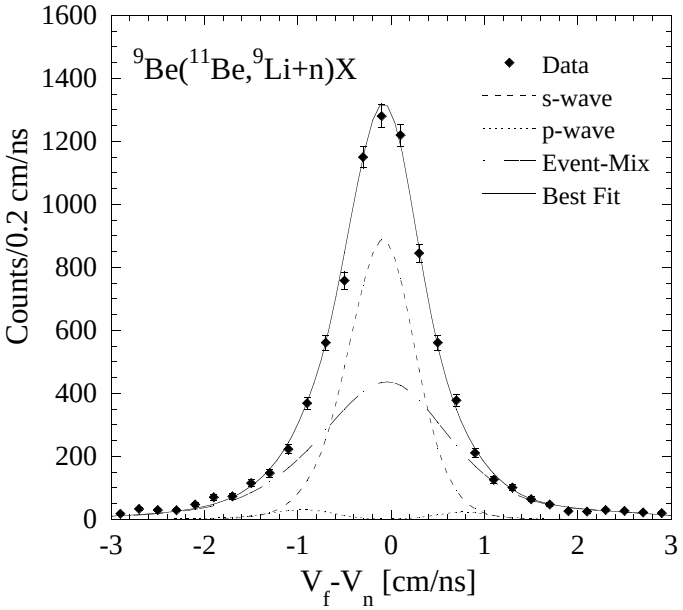

Figure 6.6: Velocity difference spectrum of the ^{9}Be(^{11}Be,^{9}Li+n)X system. Shown are the experimental data with statistical error bars, the computer simulation of a p-wave resonance at 538 keV, a a_s=-25 fm s-wave scattering, and an event-mixed background. The best fit consists of: the background: 47%, p-wave: 5%, and s-wave (a_s=-25 fm): 48%.

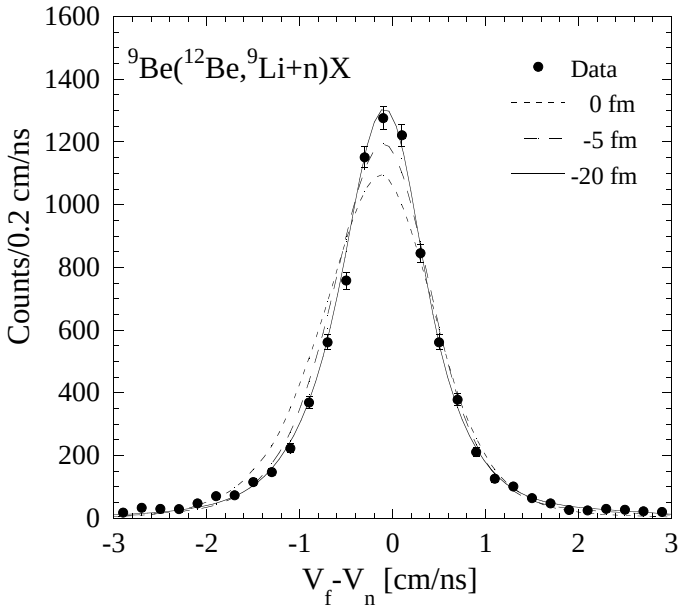

Figure 6.7: Velocity difference spectrum for the reaction ^{9}Be(^{11}Be,^{9}Li+n)X data with fits using scattering lengths a_s=0, -5, and -20 fm.

interaction of the p-states.

Whereas the loosely-bound s-state of the ^{11}Be makes the peaks in the relative velocity distribution difficult to resolve in the ^{7}He case, it makes the velocity distribution narrower in the case of ^{10}Li versus the use of a ^{12}Be projectile. A narrower relative velocity distribution does not necessarily translate into a stronger final-state interaction, since the shape of the distribution is strongly dependent on the initial states. Since there can be strong dependence on the initial states in the relative velocity distribution of the final states, the fact that the results here corroborate the findings of Thoennessen *et al.* [28] is important. The ^{11,12}Be have a very different structure from ^{18}O, which is the projectile used in [27, 28], and the fact that interactions in the $l = 0$ channel can be seen using all three projectiles makes a strong case for the existence of a low-lying s-state in the ^{10}Li. The observation of a strong final-state interaction by using ^{11}Be (which has essentially no $p^2_{1/2}$ in the initial state) proves the $l = 0$ assignment of this state.

Chapter 7

^{8}He+n

7.1 Introduction

The first experimental result on ^{9}He was reported in 1987 by Seth *et al.* [13] using a ^{9}Be(π^{-},π^{+})^{9}He reaction with a 194 MeV π^{-} beam. They found that states in ^{9}He are at the energies of 1.13 ± 0.10 MeV, 2.3 MeV ($\Gamma = 420 \pm 100$ keV) and 4.9 MeV ($\Gamma = 500 \pm 100$ keV) against neutron decay. [13]. Shortly thereafter, Bohlen *et al.* [14] reported a set of ^{9}He results from a double charge-exchange study using the ^{9}Be(^{13}C,^{13}O)^{9}He, at a beam energy of 380 MeV. They reported states at 1.8 MeV and 5.6 MeV against neutron decay. Figure 1.3 shows the data for both Seth *et al.* and Bohlen *et al.*.

The most recent measurement on ^{9}He was reported in 1995 by von Oertzen *et al.* [32]. Using a ^{9}Be(^{14}C,^{14}O)^{9}He double charge-exchange reaction with incident beam of ^{14}C at 24 MeV/u , they reported states at 1.27 MeV ($\Gamma = 0.30$ MeV), 2.42 MeV ($\Gamma = 0.85$ MeV), and 5.25 MeV against neutron decay. Figure 7.1 shows the data from von Oertzen *et al.*.

A common thread in all of these experimental results is that the lowest observed state is relatively sharp (See Figures 1.3, 7.1). The authors in all three cases inter-

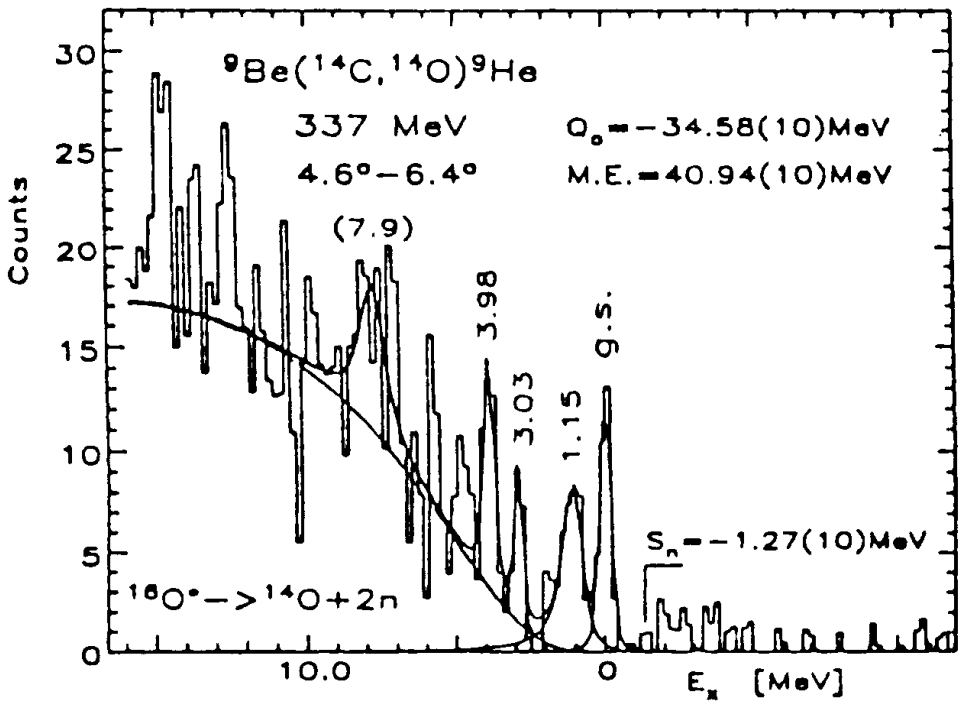

Figure 7.1: Data from von Oertzen *et al.* [32]. Shown are the observed excited states using a ^{9}Be(^{14}C,^{14}O)^{9}He reaction. The energies are shown with reference to the lowest observed state.

preted the lowest observed state as a *p*-state [13, 14, 32]. As mentioned previously, ^{9}He is a member of the N=7 isotones, which parity inversion has been predicted for the lighter members of this group. Parity inversion is well-documented for the bound ^{11}Be, and observed in ^{10}Li by [27, 28] as well as this present work. ^{9}He is the lightest isotone in this family, and the most extreme test for this prediction.

7.2 Results

Data for the ^{9}He system was limited by statistics. Most of the beamtime for this experiment was spent on the ^{11}Be nucleus, so the data with incident ^{12}Be has very low statistics. Since the data with incident ^{12}Be projectiles was too sparse to analyze, it will not be discussed here. Because of the limited statistics for ^{8}He+n data, the size of the angular cut (Section 3.1) was expanded from 5 degrees to 10 degrees to

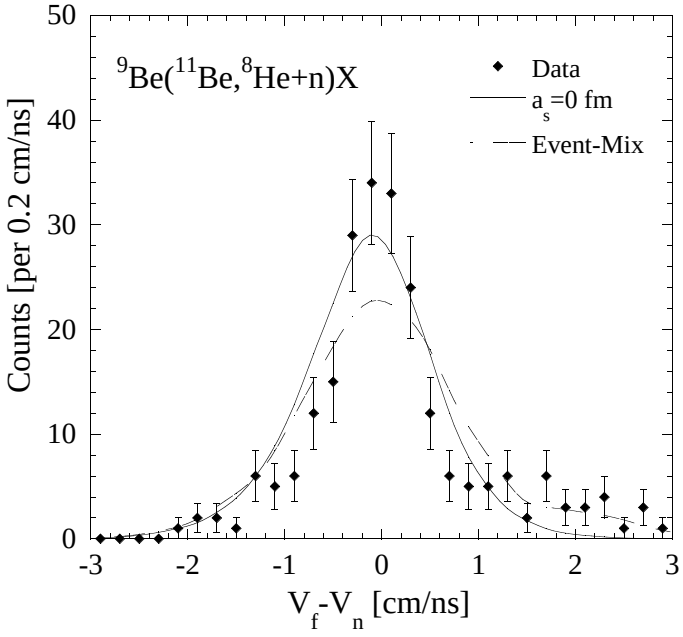

Figure 7.2: ^{9}Be(^{11}Be,^{8}He+n)X data compared with event-mixed background at the same total intensity (dashes) and best fit using a_s = 0 fm (solid). The important feature here is to observe that simple event-mixing cannot explain the data. In the best fit using a combination of an a_s = 0 fm distribution and an event-mixed background, the fit failed to describe the narrow, central peak of the data. In that case, the best fit here obtained uses 100% s-wave component and 0% event-mixed background.

increase the available data for analysis. In spite of the decreased resolution that comes from a larger acceptance angle, sufficient sensitivity remains to detect a final state interaction (Figure 3.9).

The data here is analyzed in a very similar manner as the ^{10}Li data. Figure 7.2 shows two different fits: (1) Pure event-mixed background scaled to the same number of events and (2) Best-fit using a combination s-wave (a_s = 0 fm) and event-mixed background. A distribution that consists entirely of event-mixed spectrum fails to describe the peak near zero relative velocity. A best fit using a non-interacting s-wave does a better job than the event-mixed spectrum, but it is still unsatisfactory at describing the narrowness of the relative velocity distribution.

Figure 7.3 shows ^{8}He+n relative velocity data with fits using a_s = -10 fm. Figure

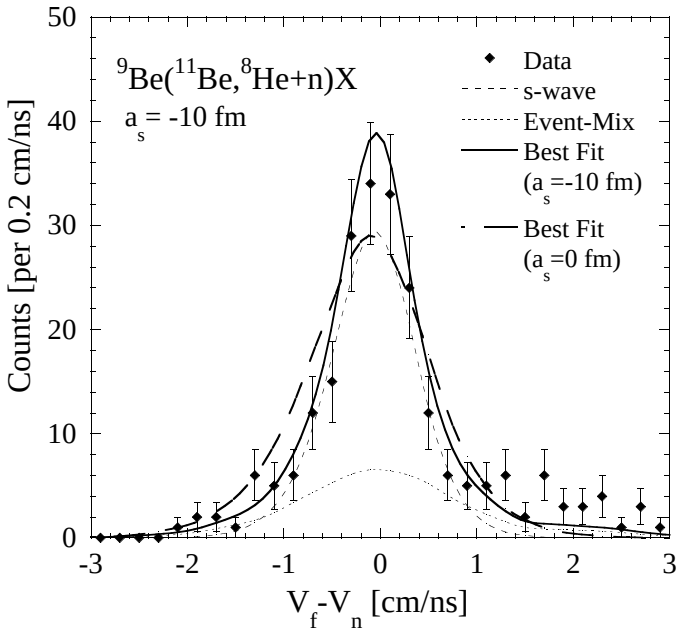

Figure 7.3: ^{9}Be(^{11}Be,^{8}He)X data with a fit using two components (solid): a_s=-10 fm (short dashes) and an event-mixed background (dots). The best fit here obtained uses 71% s-wave component and 29% event-mixed background. Also shown for the purpose of comparison is the best fit using only a combination of $a_s = 0$ fm and an event-mixed background (long dashes).

7.4 shows the reduced-χ^2 as a function of scattering length between 0 and -40 fm. The fit uses only an event-mixed background and a simulated relative velocity distribution with a given scattering length. Simulated relative velocity distributions corresponding to a final-state interaction of $a_s < -10$ fm seem to offer the best fit to the data, which is equivalent to a decay energy of less than 200 keV.

We propose that the present data represents the first observation of the low-lying ground state of ^{9}He. In addition, we further assert that this is the intruder s-state that had been predicted to exist [29]. Figure 7.5 shows two shell-model calculations from [47] using a Warburton-Brown model and compares them with results from Seth *et al.* and von Oertzen *et al.* [13, 32]. The calculations both predict a low-lying s-state as a ground state, as well as states of comparable energy to those observed by [13, 32].

The essential argument why the observed final-state interaction of the ^{9}He corresponds to an s-state follows the same line of reasoning as the ^{10}Li case. The ^{11}Be

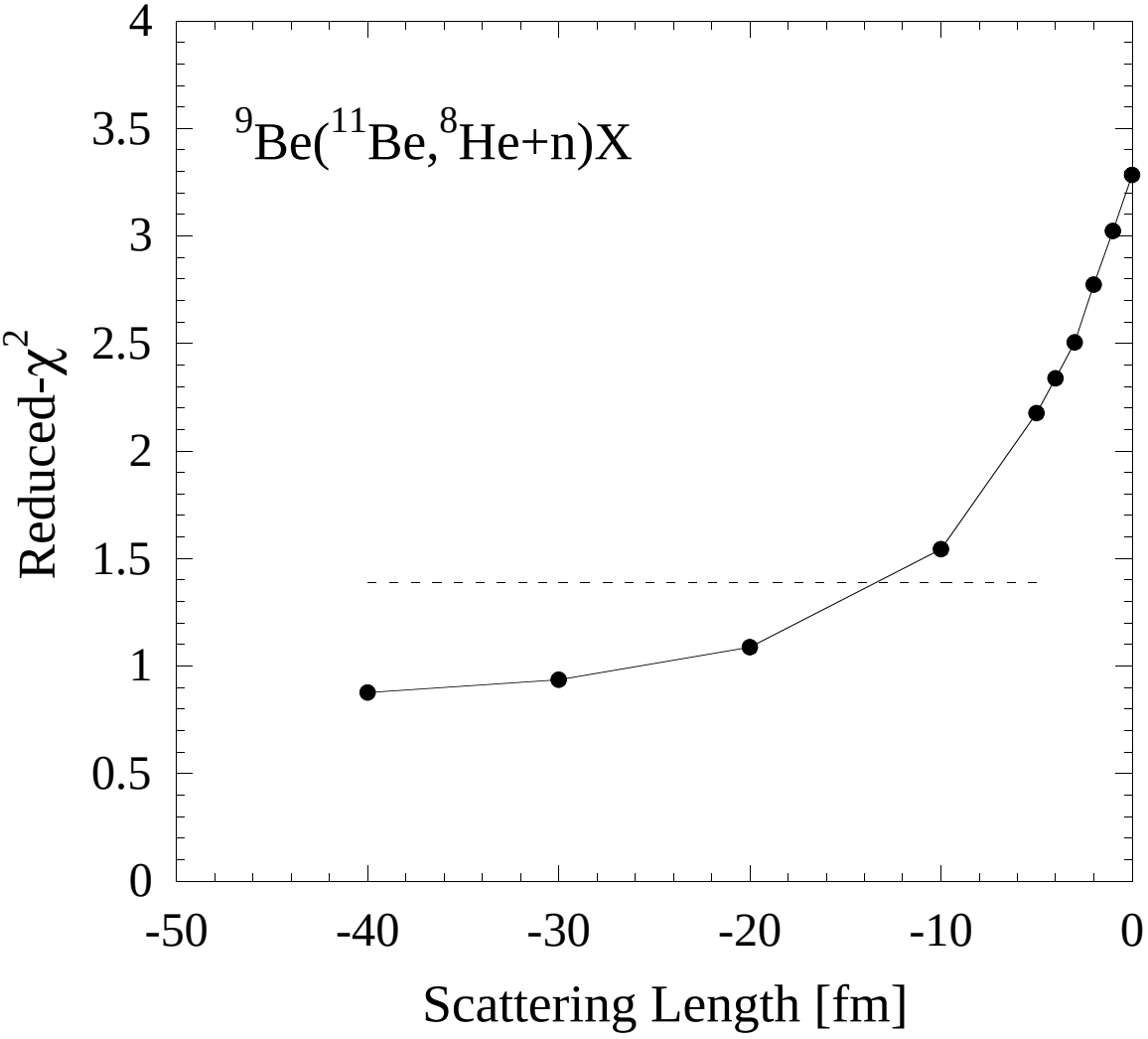

Figure 7.4: Reduced-χ^2 of fits to ^{9}Be(^{11}Be,^{8}He+n)X data as a function of the scattering length a_s of the s-state. The minimum χ^2 analysis uses three separate components in the fit. The minimization procedure uses the 12 data points between -1.1 cm/ns and 1.1 cm/ns. The 3 free parameters used in the fitting are the 1) total intensity (taken to be the same as the total number of events), 2) systematic shift in the computer-simulated relative velocity spectrum (Section 3.6), and 3) the relative intensities amongst two different components requires just one free parameters for fitting. This yields 9 degrees of freedom. The dashed line represent the reduced-χ^2 value that corresponds to a 95% confidence level, showing that a scattering length numerically larger than -10 fm best fits the data.

projectile contains essentially no $p_{1/2}$ in the initial state and is predominantly in the s-state. The formation of a ^{8}He+n system from ^{11}Be comes from double proton removal, with a neutron in the s-state. Since a final-state interaction is observed between the neutron and ^{8}He, this interaction cannot come from the p channel. This argument precludes the possibility of having observed a low-lying p-state with an energy too low to be resolved as two separate peaks (Figure 3.3).

This argument illustrates a very important point about the choice of the initial projectile. The ability to select different initial states allows the experimenter to discriminate which state gets probed, making it possible to make angular momentum assignments.

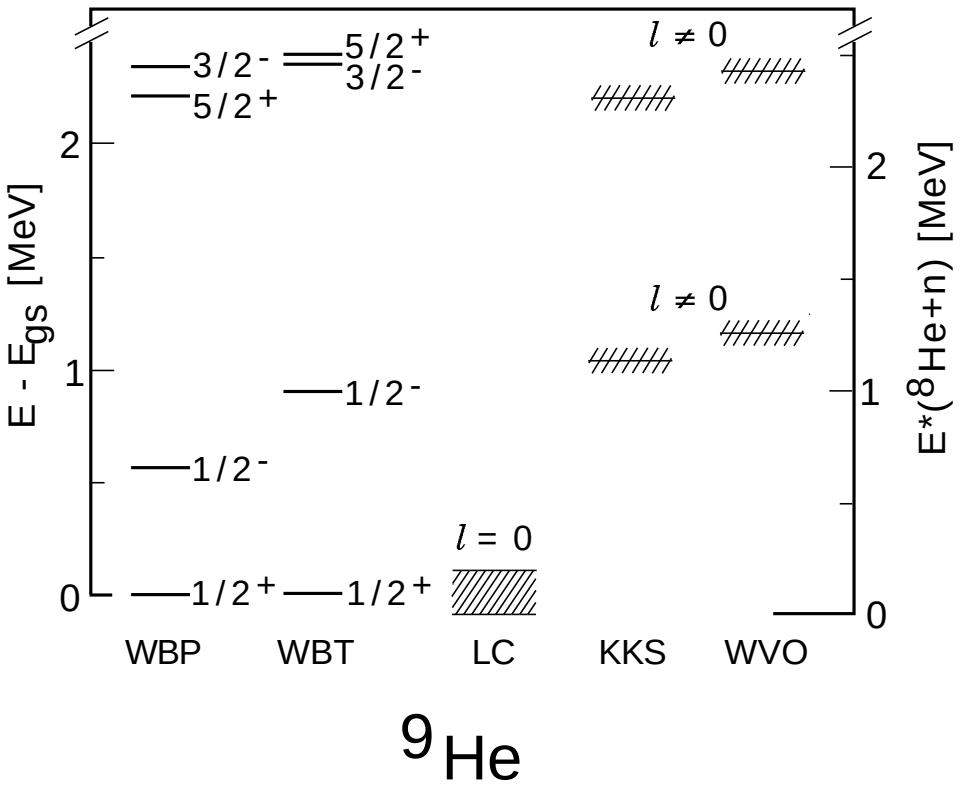

Figure 7.5: Proposed level scheme for ^{9}He. Shown here are two shell-model calculations using the Warburton-Brown model (WBP and WBT) and the data from the two experiments (Seth *et al.* (KKS) [13] and von Oertzen *et al.* (WVO)[32]) that are used for the current tabulated value for the ^{9}He mass in Audi and Wapstra [31]. Also shown is the low lying s-state observed in this work (LC). Two separate energy scales are shown. On the left is the energy scale measured with respect to the ground-state energy, and the energy scale on the right uses neutron separation energy as a reference.

Chapter 8

Summary

In this work, we have explored the FSI technique to study unbound nuclei, and made measurements on ^{7,9}He and ^{10}Li. Important experimental results can be summarized as the follows:

1) The unbound nucleus ^{7}He was studied with three different projectiles. ^{7}He was the easiest system to study, because the energy of the p resonance is much higher than those we were trying to study in the other two cases. The energy of the resonance was measured to be 440 ± 16 keV, an improvement over the current literature value of 440 ± 30 keV.

2) It has been predicted that the unbound system ^{10}Li has a low-lying s-state as a ground state. The previous two experiments by [27, 28] used an ^{18}O projectile and found a strong interaction at low energy. This is the first relative velocity measurement made with a projectile other than ^{18}O, and these observations also indicate a strong interaction in the $l = 0$ channel, with scattering length a_s <-10 fm. The fact that a low-lying s-state has been observed using three different projectile places the existence of this state on a stronger footing.

3) The first experimental observation for a low-lying s-state in the unbound ^{9}He, the lightest of the N=7 isotones, is reported. The s-state interaction is reported here

as a scattering length of $a_s \leq$-10 fm. The existence of this state has been predicted by [29] but has never been observed until this work. However, the results are restricted because of the low yields of a breakup reaction. A future study with a different inital nucleus with improved statistics could be very insightful.

The study of nuclei near and beyond the neutron dripline continues to be the ultimate test for nuclear models. The experimental limitations are the ability of accelerator facilities to produce these exotic nuclei. With more powerful facilities coming on line, it will be possible to use the final-state-interactions technique to probe the unbound states of heavier nuclei. This work has demonstrated that a final-state interaction is a promising technique to study these unbound systems. It also shows that the choice of initial projectile can be very important to these types of experiments, and good judgement must be exercised.

Appendix A

Data

The data from this experiment are contained in this appendix. The relative velocity distributions are listed in Tables A.1, A.2, and A.3. In addition, the neutron and fragment velocity distributions are listed in Tables A.4 to A.9. The fragment and neutron velocity distributins are used to calculate the event-mixed background (Section 3.6).

Table A.1: ^{6}He+n relative velocity distribution. Shown are the total number of events that satisfy the 5-degree angular cut binned in 0.2 cm/ns increments. The velocity difference distribution $V_f - V_n$ for each of the ^{12,11,10}Be projectiles is shown.

$V_f - V_n$	Incident Beam			$V_f - V_n$	Incident Beam		
(cm/ns)	^{12}Be	^{11}Be	^{10}Be	(cm/ns)	^{12}Be	^{11}Be	^{10}Be
-3.9	4	12	2	0.1	138	1011	85
-3.7	9	18	4	0.3	124	966	109
-3.5	6	21	1	0.5	162	993	144
-3.3	16	30	2	0.7	241	1147	194
-3.1	11	35	4	0.9	236	1170	218
-2.9	11	40	7	1.1	203	901	166
-2.7	9	60	11	1.3	94	536	96
-2.5	12	67	8	1.5	57	329	48
-2.3	15	87	13	1.7	36	197	18
-2.1	16	120	6	1.9	28	161	17
-1.9	25	166	21	2.1	25	104	20
-1.7	38	183	27	2.3	29	105	14
-1.5	45	266	35	2.5	16	89	18
-1.3	82	419	64	2.7	12	67	14
-1.1	126	722	128	2.9	24	42	11
-0.9	259	1165	176	3.1	12	46	14
-0.7	256	1381	235	3.3	13	55	5
-0.5	234	1367	197	3.5	12	44	16
-0.3	185	1164	165	3.7	8	46	11
-0.1	135	1073	126	3.9	14	36	10

Table A.2: ^{9}Li+n velocity difference distribution. Shown are the total number of events that satisfy the 5-degree angular cut binned in 0.2 cm/ns increments. The velocity difference distribution $V_f - V_n$ for each of the ^{12,11,10}Be projectiles is shown.

$V_f - V_n$	Incident Beam			$V_f - V_n$	Incident Beam		
(cm/ns)	^{12}Be	^{11}Be	^{10}Be	(cm/ns)	^{12}Be	^{11}Be	^{10}Be
-3.9	2	3	0	0.1	183	1221	21
-3.7	1	2	1	0.3	126	845	16
-3.5	3	9	1	0.5	101	561	11
-3.3	7	7	2	0.7	76	378	10
-3.1	6	16	3	0.9	55	211	11
-2.9	5	18	0	1.1	52	126	12
-2.7	16	33	1	1.3	32	101	12
-2.5	11	30	3	1.5	16	64	3
-2.3	7	29	2	1.7	22	47	10
-2.1	20	47	3	1.9	16	26	6
-1.9	18	70	2	2.1	9	25	6
-1.7	29	73	5	2.3	11	30	3
-1.5	27	115	6	2.5	11	27	4
-1.3	46	147	10	2.7	9	22	2
-1.1	57	223	16	2.9	6	20	4
-0.9	86	369	10	3.1	7	22	5
-0.7	112	561	32	3.3	11	14	2
-0.5	127	758	22	3.5	13	16	3
-0.3	157	1151	19	3.7	7	19	2
-0.1	181	1276	27	3.9	1	19	2

Table A.3: ^{8}He+n velocity difference distribution. Shown are the total number of events that satisfy the 10-degree angular cut binned in 0.2 cm/ns increments. The velocity difference distribution $V_f - V_n$ for each of the ^{12,11,10}Be projectiles is shown.

$V_f - V_n$	Incident Beam			$V_f - V_n$	Incident Beam		
(cm/ns)	^{12}Be	^{11}Be	^{10}Be	(cm/ns)	^{12}Be	^{11}Be	^{10}Be
-3.9	0	0	0	0.1	9	33	0
-3.7	1	0	0	0.3	5	24	2
-3.5	0	0	0	0.5	6	12	0
-3.3	2	0	0	0.7	8	6	0
-3.1	1	0	0	0.9	3	5	0
-2.9	1	0	0	1.1	7	5	0
-2.7	0	0	0	1.3	4	6	0
-2.5	2	0	0	1.5	7	2	1
-2.3	0	0	0	1.7	4	6	0
-2.1	0	1	0	1.9	4	3	0
-1.9	0	2	0	2.1	5	3	0
-1.7	2	2	0	2.3	3	4	0
-1.5	3	1	1	2.5	1	1	0
-1.3	3	6	0	2.7	5	3	0
-1.1	4	5	0	2.9	2	1	0
-0.9	5	6	0	3.1	2	0	0
-0.7	11	12	0	3.3	2	0	0
-0.5	7	15	0	3.5	1	6	0
-0.3	7	29	0	3.7	4	0	0
-0.1	6	34	0	3.9	3	1	0

Table A.4: Neutron and fragment velocity distributions from the ^{9}Be(^{12}Be,^{6}He+n)X reaction. Shown here are the velocity distributions of the ^{6}He fragments and the neutrons from coincidence events. Only events with single neutron wall and single fragment bar hits are shown here.

Velocity (cm/ns)	n	^{6}He	Velocity (cm/ns)	n	^{6}He	Velocity (cm/ns)	n	^{6}He
0.0	0	0	4.0	46	1	8.0	425	434
0.2	0	0	4.2	65	0	8.2	353	207
0.4	0	0	4.4	73	4	8.4	244	76
0.6	0	0	4.6	74	7	8.6	189	30
0.8	0	0	4.8	91	10	8.8	113	6
1.0	0	0	5.0	104	32	9.0	77	0
1.2	0	0	5.2	119	46	9.2	48	0
1.4	0	0	5.4	136	53	9.4	45	0
1.6	1	0	5.6	198	103	9.6	28	0
1.8	5	0	5.8	256	155	9.8	26	0
2.0	5	0	6.0	329	217	10.0	25	0
2.2	9	0	6.2	403	327	10.2	26	0
2.4	20	0	6.4	470	415	10.4	21	0
2.6	22	0	6.6	597	596	10.6	14	0
2.8	39	0	6.8	685	858	10.8	15	0
3.0	49	0	7.0	602	1171	11.0	4	0
3.2	55	0	7.2	697	1191	11.2	4	0
3.4	49	0	7.4	660	1172	11.4	3	0
3.6	46	0	7.6	588	983	11.6	6	0
3.8	49	0	7.8	542	675	11.8	5	0

Table A.5: Neutron and fragment velocity distributions from the ^{9}Be(^{11}Be,^{6}He+n)X reaction. Shown here are the velocity distributions of the ^{6}He fragments and the neutrons from coincidence events. Only events with single neutron wall and single fragment bar hits are shown here.

Velocity (cm/ns)	n	^{6}He	Velocity (cm/ns)	n	^{6}He	Velocity (cm/ns)	n	^{6}He
0.0	0	0	4.0	205	9	8.0	2195	1764
0.2	0	0	4.2	211	6	8.2	1699	812
0.4	0	0	4.4	236	43	8.4	1146	254
0.6	0	0	4.6	286	64	8.6	728	77
0.8	0	0	4.8	341	130	8.8	449	11
1.0	0	0	5.0	397	188	9.0	300	2
1.2	0	0	5.2	489	276	9.2	255	1
1.4	0	0	5.4	654	431	9.4	149	0
1.6	32	0	5.6	861	587	9.6	106	0
1.8	35	0	5.8	1167	858	9.8	94	0
2.0	44	0	6.0	1553	1270	10.0	81	0
2.2	58	0	6.2	2072	1794	10.2	51	0
2.4	62	0	6.4	2746	2360	10.4	39	0
2.6	120	0	6.6	3429	3136	10.6	42	0
2.8	137	0	6.8	4013	4299	10.8	37	0
3.0	158	0	7.0	4179	5840	11.0	26	0
3.2	165	0	7.2	4226	6880	11.2	16	0
3.4	172	0	7.4	3844	6471	11.4	20	0
3.6	165	4	7.6	3323	5071	11.6	12	0
3.8	204	5	7.8	2847	3344	11.8	18	0

Table A.6: Neutron and fragment velocity distributions from the ^{9}Be(^{10}Be,^{6}He+n)X reaction. Shown here are the velocity distributions of the ^{6}He fragments and the neutrons from coincidence events. Only events with single neutron wall and single fragment bar hits are shown here.

Velocity (cm/ns)	n	^{6}He	Velocity (cm/ns)	n	^{6}He	Velocity (cm/ns)	n	^{6}He
0.0	0	0	4.0	43	2	8.0	335	337
0.2	0	0	4.2	59	5	8.2	303	129
0.4	0	0	4.4	65	9	8.4	190	42
0.6	0	0	4.6	75	15	8.6	111	8
0.8	0	0	4.8	72	26	8.8	63	1
1.0	0	0	5.0	94	47	9.0	49	0
1.2	0	0	5.2	109	68	9.2	33	0
1.4	0	0	5.4	126	82	9.4	22	0
1.6	0	0	5.6	165	146	9.6	17	0
1.8	3	0	5.8	219	187	9.8	10	0
2.0	0	0	6.0	260	268	10.0	14	0
2.2	5	0	6.2	365	371	10.2	8	0
2.4	16	0	6.4	418	459	10.4	10	0
2.6	23	0	6.6	519	547	10.6	4	0
2.8	41	0	6.8	547	594	10.8	6	0
3.0	38	0	7.0	624	687	11.0	7	0
3.2	45	0	7.2	572	882	11.2	4	0
3.4	58	0	7.4	568	1014	11.4	2	0
3.6	40	0	7.6	509	841	11.6	4	0
3.8	45	2	7.8	437	600	11.8	4	0

Table A.7: Neutron and fragment velocity distributions from the ^{9}Be(^{12}Be,^{9}Li+n)X reaction. Shown here are the velocity distributions of the ^{9}Li fragments and the neutrons from coincidence events. Only events with single neutron wall and single fragment bar hits are shown here.

Velocity (cm/ns)	n	^{9}Li	Velocity (cm/ns)	n	^{9}Li	Velocity (cm/ns)	n	^{9}Li
0.0	0	0	4.0	27	0	8.0	185	8
0.2	0	0	4.2	43	0	8.2	133	0
0.4	0	0	4.4	34	0	8.4	70	0
0.6	0	0	4.6	46	0	8.6	68	0
0.8	0	0	4.8	42	1	8.8	60	0
1.0	0	0	5.0	57	0	9.0	45	0
1.2	0	0	5.2	56	1	9.2	40	0
1.4	0	0	5.4	77	3	9.4	24	0
1.6	2	0	5.6	83	13	9.6	22	0
1.8	2	0	5.8	127	51	9.8	15	0
2.0	3	0	6.0	139	136	10.0	16	0
2.2	7	0	6.2	184	218	10.2	9	0
2.4	9	0	6.4	238	333	10.4	8	0
2.6	12	0	6.6	318	590	10.6	7	0
2.8	20	0	6.8	366	806	10.8	5	0
3.0	16	0	7.0	370	963	11.0	3	0
3.2	31	0	7.2	374	747	11.2	3	0
3.4	28	0	7.4	330	345	11.4	2	0
3.6	31	0	7.6	231	194	11.6	1	0
3.8	24	0	7.8	214	65	11.8	3	0

Table A.8: Neutron and fragment velocity distributions from the ^{9}Be(^{12}Be,^{9}Li+n)X reaction. Shown here are the velocity distributions of the ^{9}Li fragments and the neutrons from coincidence events. Only events with single neutron wall and single fragment bar hits are shown here.

Velocity (cm/ns)	n	^{9}Li	Velocity (cm/ns)	n	^{9}Li	Velocity (cm/ns)	n	^{9}Li
0.0	0	0	4.0	76	2	8.0	543	10
0.2	0	0	4.2	78	0	8.2	368	0
0.4	0	0	4.4	93	0	8.4	244	0
0.6	0	0	4.6	107	0	8.6	200	0
0.8	0	0	4.8	121	3	8.8	124	0
1.0	0	0	5.0	139	5	9.0	98	0
1.2	0	0	5.2	147	8	9.2	91	0
1.4	0	0	5.4	192	37	9.4	72	0
1.6	11	0	5.6	251	128	9.6	48	0
1.8	29	0	5.8	319	330	9.8	40	0
2.0	18	0	6.0	501	676	10.0	32	0
2.2	29	0	6.2	736	937	10.2	22	0
2.4	26	0	6.4	1044	1348	10.4	14	0
2.6	50	0	6.6	1490	2507	10.6	14	0
2.8	58	0	6.8	1880	3356	10.8	9	0
3.0	58	0	7.0	2206	4621	11.0	7	0
3.2	59	0	7.2	2149	3420	11.2	6	0
3.4	75	0	7.4	1763	1458	11.4	4	0
3.6	70	0	7.6	1275	424	11.6	4	0
3.8	56	0	7.8	894	58	11.8	0	0

Table A.9: Neutron and fragment velocity distributions from the ^{9}Be(^{11}Be,^{8}He+n)X reaction. Shown here are the velocity distributions of the ^{8}He fragments and the neutrons from coincidence events. Only events with single neutron wall and single fragment bar hits are shown here.

Velocity (cm/ns)	n	^{8}He	Velocity (cm/ns)	n	^{8}He	Velocity (cm/ns)	n	^{8}He
0.0	0	0	4.0	2	0	8.0	11	0
0.2	0	0	4.2	4	0	8.2	11	0
0.4	0	0	4.4	3	0	8.4	1	0
0.6	0	0	4.6	5	0	8.6	4	0
0.8	0	0	4.8	6	0	8.8	2	0
1.0	0	0	5.0	3	0	9.0	1	0
1.2	0	0	5.2	7	0	9.2	1	0
1.4	0	0	5.4	5	0	9.4	0	0
1.6	0	0	5.6	6	0	9.6	0	0
1.8	1	0	5.8	11	2	9.8	0	0
2.0	0	0	6.0	32	15	10.0	0	0
2.2	3	0	6.2	28	53	10.2	0	0
2.4	1	0	6.4	35	83	10.4	0	0
2.6	3	0	6.6	42	77	10.6	1	0
2.8	4	0	6.8	46	79	10.8	0	0
3.0	1	0	7.0	43	78	11.0	0	0
3.2	2	0	7.2	40	43	11.2	0	0
3.4	4	0	7.4	30	4	11.4	0	0
3.6	2	0	7.6	14	0	11.6	0	0
3.8	4	0	7.8	15	0	11.8	0	0

LIST OF REFERENCES

[1] T. Motobayshi, Y. Ikeda, Y. Ando, K. Ieki, M. Inoue, N. Iwasa, T. Kikuchi, M. Kurokawa, S. Moriya, S. Ogawa, H. Murakami, S. Shimoura, Y. Yanagisawa, T. Nakamura, Y. Watanabe, M. Ishihara, T. Teranishi, H. Okuno, R.F. Casten, *Phys. Lett.* B **346**, 9 (1995).

[2] R.W. Ibbotson, T. Glasmacher, B.A. Brown, L. Chen, M.J. Chromik, P.D. Cottle, M. Fauerbach, K.W. Kemper, D.J. Morrissey, H. Scheit, and M. Thoennessen, *Phys. Rev. Lett.* **80**, 2081 (1998).

[3] B.V. Pritychenko, T. Glasmacher, P.D. Cottle, M. Fauerbach, R.W. Ibbotson, K.W. Kemper, V. Maddalena, A. Navin, R. Ronnigen, A. Sakharuk, H. Scheit, V.G. Zelevinsky, *Phys. Lett.* **B461**, 322 (1999).

[4] I. Tanihata, H. Hamagaki, O. Hashimoto, Y. Shida, Y. Yoshikawa, K. Sugimoto, O. Yamakawa, and T. Kobayashi, *Phys. Rev. Lett.* **55**, 2676 (1985).

[5] T. Kobayashi, O. Yamakawa, K. Omata, K. Segimoto, T. Shimoda, N. Takahashi, and I. Tanihata, *Phys. Rev. Lett.* **60**, 2599 (1988).

[6] N.A. Orr, N. Anantaraman, S. M. Austin, C.A. Bertulani *et al.*, *Phys. Rev. Lett.* **69**, 2050 (1992).

[7] J.H. Kelley, S.M. Austin, R.A. Kryger, D.J. Morrissey, N.A. Orr, B.M. Sherrill, M. Thoennessen, J.S. Winfield, J.A. Winger, and B.M. Young, *Phys. Rev. Lett.* **74**, 30 (1995).

[8] A. Navin, D. Bazin, B.A. Brown, B. Davids, G. Gervais, T. Glasmacher, P.G. Hansen, M. Hellstroöm, R.W. Ibbotson, V. Maddalena, B. Pritychenko, H. Scheit, B.M. Sherrill, M. Steiner, J.A. Tostevin, J. Yurkon, *Phys. Rev. Lett.* **81**, 5089 (1998).

[9] T. Aumann, A. Navin, D.P. Balamuth, D. Bazin, B. Blank, B.A. Brown, J.E. Buth, J.A. Caggiano, B. Davids, T. Glasmacher, V. Guimarães, PG. Hansen, R.W. Ibbotson, D. Karnes, J.J. Kolata, V. Maddalena, B. Pritychenko, H. Scheit, B.M. Sherrill, and J.A. Tostevin *Phys. Rev. Lett.* **84**, 35 (2000).

[10] R.H. Stokes and P.G. Young, *Phys. Rev.* **178**, 2024 (1969).

[11] H.G. Bohlen, B. Gebauer, M. von Lucke-Petsch, A.N. Ostrowski, M. Wilpert, Th. Wilpert, H. Lenske, D.V. Alexandrov, A.S. Demyanova, E. Nikolskii, A.A. Korsheninnikov, A.A. Ogloblin, R. Kalpakchieva, Y.E. Penionzhkevich, S. Piskor, *Z. Phys.* A **344**, 381 (1993).

[12] J.A Caggiano, D. Bazin, W. Benenson, B. Davids, B.M. Sherrill, M. Steiner, J. Yurkon, A.F. Zeller, B. Blank, *Phys. Rev.* C **60**, 064322 (1999).

[13] K.K. Seth, M. Artuso, D. Barlow, M. Kaleta, H. Nann, B. Parker, and R. Soundranayagam, *Phys. Rev. Lett.* **58**, 1930 (1987).

[14] H.G. Bohlen, B. Gebauer, D. Kolbert, W. von Oertzen, E. Stiliaris, M. Wilpert, and T. Wilpert, *Z. Phys.* **330**, 227 (1988).

[15] R.P. Haddock, R.M. Salter, Jr., M. Zeller, J.B. Czirr, and D.R. Nygren, *Phys. Rev. Lett.* **14**, 318 (1965).

[16] R. Honecker and H. Grässler, *Nucl. Phys.* **A107**, 81 (1968).

[17] B. Zeitnitz, R. Maschuw, and P. Suhr, *Nucl. Phys.* **A149**, 449 (1970).

[18] I. Šlaus, Y. Akaishi, and H. Tanaka *Phys. Reports* **173**, 257 (1990).

[19] G.A. Miller, B.M.K. Nefkens, and I. Slaus, *Phys. Reports* **194**, 1 (1990).

[20] C.R. Howell, Q. Chen, T.S. Carman, A. Hussein, W.R. Gibbs, B.F. Gibson, G. Mertens, C.F. Moore, C. Morris, A. Obst, E. Pasyuk, C.D. Roper, F. Salinas, I. Slaus, S. Sterbenz, W. Tornow, R.L. Walter, C.R. Whiteley, M. Whitton, *Phys. Lett.* **B444**, 252 (1998).

[21] H.S.W. Massey, *Progr. Nucl. Phys.* **3**, 237 (1953).

[22] A.B. Migdal *Soviet Physics-JETP* **1**, 2 (1955).

[23] K. Ilakovac, L. G. Kuo, M. Petravić, I. Šlaus, and P. Thomaš, *Phys. Rev. Lett.* **6**, 356 (1961).

[24] K. Ilakovac, L.G. Kuo, M. Petravić, I. Šlaus, and P. Thomaš, *Nucl. Phys.* **B53**, 254 (1963).

[25] M. Cerineo, K. Ilakovac, I. Šlaus, P. Thomaš, and V. Velković, *Phys. Rev.* **133**, B948 (1963).

[26] R.M. Salter, Jr., R.P. Haddock, M. Zeller, D.R. Nygren, and J.B. Czirr,*Nucl. Phys.* **A254**, 241 (1975).

[27] R.A. Kryger, A. Azhari, A. Galonsky, J.H. Kelley, R. Pfaff, E. Ramakrishnan, D. Sackett, B.M. Sherrill, M. Thoennessen, J.A. Winger, and S. Yokoyama, *Phys. Rev.* C **47**, R2439 (1993).

[28] M. Thoennessen, S. Yokoyama, A. Azhari, T. Baumann, J.A. Brown, A. Galonsky, P.G. Hansen, J.H. Kelley, R.A. Kryger, E. Ramakrishnan, and P. Thrilof, *Phys. Rev.* C **59**, 111 (1999).

[29] H. Sagawa, B.A. Brown, and H. Esbensen, *Phys. Lett.* **B309**, 1 (1993).

[30] I.J. Thompson and M.V. Zhukov, *Phys. Rev.* C **49**, 1904 (1994).

[31] G. Audi and A.H. Wapstra, *Nucl. Phys.* **A595**, 409 (1995).

[32] W. von Oertzen, H.G. Bohlen, G. Gebauer, M. von Lucke-Petsch, A.N. Ostrowski, Ch. Seyfert, Th. Stolla, M. Wilpert, Th. Wilpert, D.V. Alexandrov, A.A. Korsheninnikov, I. Mukha, A.A. Ogloblin, S.M. Grimes, and T.N. Massey, *Nucl. Phys.* **A588**, 129c (1995).

[33] P.D. Zecher, *Nucl. Instrum. Methods* **401**, 329 (1997).

[34] J.J. Kruse, Ph.D. Thesis. (1999)

[35] P.D. Zecher, Ph.D. Thesis. (1996)

[36] S.K. Yokoyama, Ph.D. Thesis. (1996)

[37] A.S. Goldhaber, *Phys. Lett.* **B53**, 306 (1974).

[38] H. Feshbach and K. Huang, *Phys. Lett.* **47B**, 300 (1973).

[39] M.J. Murphy and R.G. Stokstad, *Phys. Rev.* C **28**, 428 (1983).

[40] F. Hubert, R. Bimbot and H. Gauvin, *At. Data Nucl. Data Tables* **46**, 9 (1990).

[41] P.G. Hansen, *Phys. Rev. Lett.* **77**, 1016 (1996).

[42] J.A. Tostevin, *J. Phys. G: Nucl.* **25**, 735 (1999).

[43] B.A. Brown, Private Communications, 1999.

[44] M. Zinser, F. Humbert, T. Nilsson, W. Schwab, Th. Blaich, M.J.G. Borg, L.V. Chulkov, H. Eickhoff, Th.W. Elze, H. Emling, B. Franzke, H. Freiesleben, H. Geissel, K. Grim, D. Guillemaude-Muller, P.G. Hansen, R. Holzmann, H. Irnich, B. Jonson, J.G. Keller, O. Klepper, H. Klinger, J.V. Kratz, R. Kulessa, D. Lambrecht, Y. Leifels, A. Magel, M. Mohar, A.C. Mueller, G. Münzenberg, F. Nickel, G. Nyman, A. Richter, K. Riisager, C. Scheidenberger, G. Schrieder, B.M. Sherrill, H. Simon, K. Stelzer, J. Stroth, O. Tengblad, W. Trautmann, E. Wajda, and E. Zude, *Phys. Rev. Lett.* **75**, 1719 (1995).

[45] R.G. Stokstad, *Comments Nucl. Part. Phys.* **13**, 231 (1984).

[46] R.H. Stokes and P.G. Young, *Phys. Rev. Lett.* **18**, 611 (1967).

[47] B.A. Brown, Private Communications, 1994.

[48] B.M. Young, W. Benenson, J.H. Kelley, N.A. Orr, R. Pfaff, B.M. Sherrill, M. Steiner, M. Thoennessen, J.S. Winfield, J.A. Winger, S.J. Yennello, and A. Zeller, *Phys. Rev.* C **49**, 279 (1994).

[49] K.H. Wilcox, R.B. Weisenmiller, G.J. Wozniak, N.A. Jelley, D. Ashery, and J. Cerny, *Phys. Lett.* **59B**, 142 (1975).

[50] J. Wang, Ph.D. Thesis. (1999)

[51] R.B. Firestone, V.S. Shirley, C.M. Baglin, S.Y.F. Chu, and J. Zipkin, *Table of Isotopes, Eigth Edition, Volume I* (John Wiley & Sons, Inc., 1996).

[52] R. Anne, R. Bimbot, S. Dogny, H. Emling, D. Guillemaud-Mueller *et al.*, *Nucl. Phys.* **A575**, 125 (1994).

[53] M. Chartier, J.R. Beene, B. Blank, L. Chen, A. Galonsky, N. Gan, P.G. Hansen, J. Kruse, V. Maddalena, M. Thoennessen, R.L. Varner, *To be pulished.*

[54] B. Zwieglinski, W. Benenson and R.G.H. Robertson, *Nucl. Phys.* **A315**, 124 (1979).

[55] A. Navin, D.W. Anthony, T. Aumann, T. Baumann, D. Bazin, Y. Blumenfeld, B.A. Brown, T. Glasmacher, P.G. Hansen, R.W. Ibbotson, P.A. Lofy, V. Maddalena, K. Miller, T. Nakamura, B. Pritychenko, B.M. Sherrill, E. Spears, M. Steiner, J.A. Tostevin, J. Yurkon, A. Wagner, *To be pulished.*